

University of Louisville

ThinkIR: The University of Louisville's Institutional Repository


Electronic Theses and Dissertations

5-2023

Structural, magnetic, electrical, pseudocapacitive, and electrocatalytic properties of bilayered ruddlesden-popper oxides.

Chandana C W Kananke-Gamage
University of Louisville

Follow this and additional works at: <https://ir.library.louisville.edu/etd>

 Part of the [Analytical Chemistry Commons](#), [Inorganic Chemistry Commons](#), and the [Materials Chemistry Commons](#)

Recommended Citation

Kananke-Gamage, Chandana C W, "Structural, magnetic, electrical, pseudocapacitive, and electrocatalytic properties of bilayered ruddlesden-popper oxides." (2023). *Electronic Theses and Dissertations*. Paper 4098.

Retrieved from <https://ir.library.louisville.edu/etd/4098>

This Doctoral Dissertation is brought to you for free and open access by ThinkIR: The University of Louisville's Institutional Repository. It has been accepted for inclusion in Electronic Theses and Dissertations by an authorized administrator of ThinkIR: The University of Louisville's Institutional Repository. This title appears here courtesy of the author, who has retained all other copyrights. For more information, please contact thinkir@louisville.edu.

STRUCTURAL, MAGNETIC, ELECTRICAL, PSEUDOCAPACITIVE, AND
ELECTROCATALYTIC PROPERTIES OF BILAYERED RUDDLESDEN-POPPER
OXIDES

By

Chandana C W Kananke-Gamage
B.Sc., University of Colombo, 2017

A Dissertation
Submitted to the Faculty of the
College of Arts and Sciences of the University of Louisville
in Partial Fulfilment of the Requirements
for the Degree of

Doctor of Philosophy in Chemistry

Department of Chemistry
University of Louisville
Louisville, Kentucky

May 2023

© Copyright 2023 by Chandana C W Kananke-Gamage

All rights reserved

STRUCTURAL, MAGNETIC, ELECTRICAL, PSEUDOCAPACITIVE, AND
ELECTROCATALYTIC PROPERTIES OF BILAYERED RUDDLESDEN-POPPER
OXIDES

By

Chandana C W Kananke-Gamage

A Dissertation Approved on

April 20, 2023

by the following Dissertation Committee:

Dissertation Director- Dr. Farshid Ramezanipour

Dr. Robert M. Buchanan

Dr. Jinjun Liu

Dr. Gamini Sumanasekera

DEDICATION

This work is dedicated to my mother, Wimala Violet Weerasooriya, my late father Kananke Gamage Wijayasiri, my three sisters, my brother, my three brothers-in law and my beloved husband, Dhanushka Hetti Arachchilage for all the support, love, inspiration, and motivation. Lastly, I dedicate this work to my high school teachers, the Science faculty professors at the University of Colombo, for enriching me with their expertise and providing me with academic support to advance my career toward the Doctor of Philosophy degree.

ACKNOWLEDGEMENTS

First and foremost, I want to express my heartfelt gratitude to Dr. Farshid Ramezanipour, my research supervisor, who has been an invaluable mentor to me. It is an honor for me to be part of the Ramezanipour research group. Throughout my graduate studies, Dr. Ramezanipour has always been encouraging, compassionate, and supportive. His accessibility, advice, unwavering support, patience, and direction will be a lifetime favor for me. I am grateful to him for providing me with opportunities to study, develop, and improve as a scientist and a good person. I am extremely grateful to my mother, Wimala Violet Weerasooriya for being such a lovely mother, who is always by my side. Although he is not with us, I am thankful to my father for being my motivation. I am so thankful to my beloved husband for the support he gave me and the path he showed me to achieve my dream of becoming a PhD scholar. I want to express my gratitude to my family and friends for their guidance and support, which have been crucial in getting me through the several trying circumstances I encountered during this graduate program. Being surrounded by such wonderful, amazing, kind, and caring people makes me feel lucky and honored. I want to express my gratitude to Dr. Robert Buchanan, Dr. Jinjun Liu, and Dr. Gamini Sumanasekera for serving as members of my research and dissertation committees. I appreciate their comments, constructive criticism, advice, and guidance to complete my graduate degree. I would like to extend my deepest regards to the entire staff at the Department of Chemistry for their assistance with my academic and professional goals. Particularly, I would like to acknowledge Mrs. Sherry Nalley and Mr. Steve Riley for their

selfless academic, administrative, and technical support throughout my graduate studies in the Chemistry Department. Also, I would like to express my gratitude to all my present coworkers including the prior members of the Ramezanipour research group. Dr. Ram Krishna Hona, Dr. Selorm Joy Fanah and Dr. Surendra Karki for their inspiration, encouragement, and support throughout my PhD studies.

ABSTRACT

STRUCTURAL, MAGNETIC, ELECTRICAL, PSEUDOCAPACITIVE, AND ELECTROCATALYTIC PROPERTIES OF BILAYERED RUDDLESDEN-POPPER OXIDES

Chandana C W Kananke-Gamage

April 20, 2023

Ruddlesden Popper (RP) oxides are perovskite-derived functional materials with the general formula $A_{n-1}A'_2B_nO_{3n+1}$, where A/A' is often a lanthanide or alkaline earth metal, and B is usually a transition metal. These materials contain perovskite-like connectivity, where BO_6 units share apexes to form layers that are stacked above each other. The number of layers in each stack is represented by n in the above formula. The spaces between stacks are often occupied by lanthanide or alkaline-earth metals (A' -site metals), which also reside in intra-stack spaces (A -site) between the octahedra. Oxide materials derived from perovskites have been studied for a wide range of applications, such as solar cells, batteries, catalysts, and capacitors.

We have studied the electrocatalytic properties of RP materials for water splitting. This is an important application given the need for efficient and economical electrocatalysts for the two half-reactions of water-splitting, namely hydrogen-evolution reaction (HER) and oxygen-evolution reaction (OER). The benchmark catalysts to overcome the sluggish kinetics of OER and HER are Ru, Ir, and Pt-based catalysts. Such catalysts are expensive

since they use precious metals, and some of them have stability issues. Owing to their compositional diversity and the thermodynamic stability, multi-element transition metal oxides are promising candidates for electrocatalytic water splitting. The variation of A and B-site metals in RP oxides can lead to changes in physical and chemical properties, such as crystal structure, magnetism, conductivity, and electrochemical catalysis. In this study, several bilayered ($n = 2$) RP oxides are synthesized followed by systematic study of magnetic, charge transport, pseudocapacitive, and electrocatalytic properties.

The effect of structural symmetry on electrocatalytic properties in two isoelectronic materials, $\text{Sr}_2\text{LaMn}_2\text{O}_7$ and $\text{Ca}_2\text{LaMn}_2\text{O}_7$, which were synthesized by varying the A-site cation, was investigated. The structural changes identified are associated with systematic variation in the magnetic, electrical charge transport and electrocatalytic properties toward both components of water splitting, namely OER and HER.

The effect of the B-site cation on electrocatalytic performance of two RP materials, $\text{Sr}_2\text{LaFeMnO}_7$ and $\text{Sr}_2\text{LaCoMnO}_7$ was also studied. Here, the variation in the B-site cation can result in significant changes in magnetic properties, charge-transport properties, and the activity toward the HER and OER processes.

Together with the A/A' and B-site changes of RP oxides, oxygen vacancies in these oxide materials strongly affect the properties including conductivity and electrocatalytic activity. Systematic trends in the series of materials, $\text{Sr}_3\text{Ti}_{2-x}\text{M}_x\text{O}_{7-\delta}$ ($\text{M} = \text{Mn, Fe, Co}$; $x = 0, 1$) were observed with the creation of oxygen vacancies which correlate with electrocatalytic and charge-transport properties.

The bilayered RP materials have been also explored to understand the oxide intercalation based pseudocapacitance. The change in pseudocapacitive properties as a function of structural symmetry in two materials $\text{Ca}_2\text{LaMn}_2\text{O}_7$ and $\text{Sr}_2\text{LaMn}_2\text{O}_7$ was studied in the alkaline medium.

Overall, in the bilayered RP oxides, the electrical, electrochemical and electrocatalytic characteristics can be modified by changing the elemental composition, symmetry, and oxygen vacancies.

TABLE OF CONTENTS

DEDICATION	iii
ACKNOWLEDGEMENTS	iv
ABSTRACT	vi
CHAPTER 1 : INTRODUCTION	1
1.1 Background	1
1.2 Perovskite Oxides.....	2
1.3 Perovskite Derived Ruddlesden-Popper (RP) Oxides.....	3
1.4 Properties Of Perovskites And Perovskite-Derived RP Oxides.....	5
1.4.1 Electrical Charge Transport.....	5
1.4.2 Magnetic Properties	8
1.4.3 Electrocatalytic Properties	9
1.4.4 Pseudocapacitive Energy Storage Properties	14
1.5 Material Synthesis Methods	16
1.5.1 Solid State Synthesis	16
1.5.2 Sol-Gel Synthesis	18
1.6 Characterization Techniques	19
1.6.1 Powder X-Ray Diffraction.....	19
1.6.2 Electrical Conductivity Measurements.....	22

1.6.3 Magnetic Measurements	24
1.6.4 Iodometric Titration.....	25
1.6.5 Scanning Electron Microscopy.....	26
1.6.6 X-Ray Photoelectron Spectroscopy	27
1.6.7 Raman Spectroscopy	28
1.7 Application Of The Above Topics In This Work	28
CHAPTER 2 : EFFECT OF STRUCTURAL SYMMETRY ON MAGNETIC, ELECTRICAL, AND ELECTROCATALYTIC PROPERTIES OF ISOELECTRONIC OXIDES $A_2LaMn_2O_7$ (A= Sr^{2+} , Ca^{2+})	
2.1 Experimental	30
2.1.1 Synthesis.....	30
2.1.2 Characterization.....	30
2.1.3 Electrochemical OER/HER Studies	31
2.2 Results And Discussion.....	33
2.2.1 Crystal Structure.....	33
2.2.2 Electrical Conductivity	38
2.2.3 Magnetic Properties	40
2.2.4 Electrocatalytic Properties For OER And HER	42
2.3 Conclusions	49
CHAPTER 3 : Variation Of Electrocatalytic Activity Of Isostructural Oxides $Sr_2LaFeMnO_7$ And $Sr_2LaCoMnO_7$ For Hydrogen And Oxygen-Evolution	
	51

3.1 Experimental	51
3.1.1 Synthesis	51
3.1.2 Characterization	51
3.1.3 Electrocatalytic Measurements For OER And HER	52
3.2 Results And Discussion	54
3.2.1 Crystal Structure	54
3.2.2 Electrical Conductivity	58
3.2.3 Magnetic Properties	59
3.2.4 Electrocatalytic Activity For HER	62
3.2.5 Electrocatalytic Activity For OER	64
3.3 Conclusions	70
CHAPTER 4 : SYSTEMATIC VARIATION OF ELECTROCATALYTIC ACTIVITY	
FOR WATER SPLITTING IN ISOSTRUCTURAL OXIDES $\text{Sr}_3\text{Ti}_{2-x}\text{M}_x\text{O}_{7-\Delta}$ (M = Mn,	
Fe, Co; X = 0, 1)	
72	
4.1 Experimental	72
4.1.1 Synthesis	72
4.1.2 Characterization	73
4.1.3 Electrochemical OER/HER Measurements	74
4.2 Results And Discussion	75
4.2.1 Crystal Structure And Oxygen Content	75
4.2.2 Electrical Conductivity	80

4.2.3 Electrocatalytic Properties For HER And OER	83
4.3 Conclusions	90
CHAPTER 5 : STRUCTURE EFFECT ON PSEUDOCAPACITIVE PROPERTIES OF A ₂ LaMn ₂ O ₇ (A = Ca, Sr)	91
5.1 Experimental	91
5.1.1 Synthesis	91
5.1.2 Characterization	91
5.1.3 Pseudocapacitance Measurements	92
5.2 Results And Discussion	93
CHAPTER 6 : CONCLUSION	102
REFERENCES	106
CURRICULUM VITAE	115

LIST OF FIGURES

Figure 1.1: The unit cell of a simple perovskite and the coordination of the cations with oxygen.....	3
Figure 1.2: The unit cell of a RP structure and the coordination of the cations with oxygen.....	5
Figure 1.3: A set of lattice planes (100) in a unit cell.....	20
Figure 1.4: A graphical representation of Bragg's Law.	21
Figure 1.5: The four - probe conductivity setup.	23
Figure 1.6: The two - probe conductivity setup.....	23
Figure 2.1: Rietveld refinement profiles for powder X-ray diffraction data for (a) $\text{Ca}_2\text{LaMn}_2\text{O}_7$ and (b) $\text{Sr}_2\text{LaMn}_2\text{O}_7$. The experimental data are represented by black crosses. The red line shows the fit. The vertical green tick marks and the lower blue line correspond to the Bragg peak positions and difference plot, respectively.	33
Figure 2.2: Crystal structure of $\text{A}_2\text{LaMn}_2\text{O}_7$ ($\text{A}=\text{Ca}/\text{Sr}$). Green spheres represent $\text{Ca}/\text{Sr}/\text{La}$ and red spheres are oxygen. The Mn atoms are shown as light blue spheres at the centers of MnO_6 octahedra.	35
Figure 2.3: Scanning electron microscopy images of (a) $\text{Ca}_2\text{LaMn}_2\text{O}_7$ and (b) $\text{Sr}_2\text{LaMn}_2\text{O}_7$	37
Figure 2.4: (a) Electrical conductivity variation as a function of temperature. (b) Arrhenius plots for determination of the activation energies (E_a) for the temperature-activated increase in conductivity, giving $E_a = 0.0877$ (25-500 °C) for $\text{Sr}_2\text{LaMn}_2\text{O}_7$ and $E_a = 0.0898$ (25-400 °C) for $\text{Ca}_2\text{LaMn}_2\text{O}_7$	39

Figure 2.5: (a) and (b) show zero-field-cooled (ZFC) and field-cooled (FC) magnetic susceptibility data. (c) and (d) show the isothermal magnetization data as a function of magnetic field. The lines are guide to the eye.	41
Figure 2.6: OER activity in 0.1 M KOH for Sr ₂ LaMn ₂ O ₇ (red) and Ca ₂ LaMn ₂ O ₇ (green): (a) Polarization curves, (b) Tafel plots and (c) Chronopotentiometry response of Sr ₂ LaMn ₂ O ₇	43
Figure 2.7: (a) HER polarization curves in 0.5 M H ₂ SO ₄ for Ca ₂ LaMn ₂ O ₇ (green) and Sr ₂ LaMn ₂ O ₇ (red). (b) Tafel plots and Tafel slopes. (c) Chronopotentiometry data for Sr ₂ LaMn ₂ O ₇	44
Figure 2.8: (a) HER polarization curves in 1 M KOH for Ca ₂ LaMn ₂ O ₇ (green) and Sr ₂ LaMn ₂ O ₇ (red). (b) Tafel plots and Tafel slopes. (c) Chronopotentiometry data for Sr ₂ LaMn ₂ O ₇	45
Figure 2.9: HER polarization curves in 0.1 M KOH for Ca ₂ LaMn ₂ O ₇ (green) and Sr ₂ LaMn ₂ O ₇ (red).	45
Figure 2.10: X-ray diffraction data of Sr ₂ LaMn ₂ O ₇ before and after 500 cycles of HER in the 0.5 M H ₂ SO ₄	46
Figure 2.11: X-ray diffraction data of Sr ₂ LaMn ₂ O ₇ , before and after 500 cycles of HER in 1 M KOH.	47
Figure 2.12: (a) and (b) show cyclic voltammetry (CV) data in non-Faradaic region in 0.1 M KOH. (c) shows the plot of j_{average} obtained from the middle potential of the above CVs as a function of scan rate. The slopes give the double layer capacitance values.	48
Figure 3.1: Rietveld refinement profiles for powder X-ray diffraction data for (a) Sr ₂ LaCoMnO ₇ and (b) Sr ₂ LaFeMnO ₇ . The experimental data are represented by black crosses. The red line shows the fit. The vertical magenta tick marks, and the lower blue line correspond to the Bragg peak positions and difference plot, respectively.	54
Figure 3.2: Crystal structure of Sr ₂ LaBMnO ₇ (B = Fe, Co). Green spheres represent Sr/La, and red spheres show oxygens. The BO ₆ octahedra are shown in dark blue.	55
Figure 3.3: Scanning electron microscopy images for Sr ₂ LaCoMnO ₇ compared to Sr ₂ LaFeMnO ₇	57

Figure 3.4: (a) Electrical conductivity variation as a function of temperature for $\text{Sr}_2\text{LaFeMnO}_7$ (green) and $\text{Sr}_2\text{LaCoMnO}_7$ (blue). (b) Arrhenius plots for determination of the activation energies (E_a) for the temperature-activated increase in conductivity, giving $E_a = 0.2499$ (25-800 °C) for $\text{Sr}_2\text{LaMnCoO}_7$ and $E_a = 0.194$ (25-500 °C) for $\text{Sr}_2\text{LaMnCoO}_7$	59
Figure 3.5: (a) and (b) show zero-field-cooled (ZFC) and field-cooled (FC) magnetic susceptibility data. (c) and (d) show the isothermal magnetization data as a function of magnetic field.....	61
Figure 3.6: HER activity in 0.5 M H_2SO_4 for $\text{Sr}_2\text{LaFeMnO}_7$ (green), $\text{Sr}_2\text{LaCoMnO}_7$ (blue), and Pt/C (black): (a) Polarization curves. (b) Tafel plots. (c) Chronopotentiometry for $\text{Sr}_2\text{LaCoMnO}_7$	63
Figure 3.7: OER activity in 0.1 M KOH for $\text{Sr}_2\text{LaFeMnO}_7$ (green), $\text{Sr}_2\text{LaCoMnO}_7$ (blue), and IrO_2 (black): (a) Polarization curves. (b) Tafel plots. (c) Chronopotentiometry response of $\text{Sr}_2\text{LaCoMnO}_7$	65
Figure 3.8: (a) and (b) cyclic voltammetry in non-Faradaic region in 0.1 M KOH. (c) javerage obtained from these CV plotted as a function of scan rate. The slope gives double layer capacitance.	67
Figure 3.9: X-ray diffraction data for $\text{Sr}_2\text{LaCoMnO}_7$ before and after 1000 cycles of OER.	67
Figure 3.10: X-ray photoelectron spectroscopy data, showing cobalt binding energies, for $\text{Sr}_2\text{LaCoMnO}_7$ before (top) and after (bottom) 1000 cycles of OER.....	68
Figure 3.11: X-ray photoelectron spectroscopy data, showing manganese binding energies, for $\text{Sr}_2\text{LaCoMnO}_7$ before and after 1000 cycles of OER.	68
Figure 3.12: Raman spectroscopy data for $\text{Sr}_2\text{LaCoMnO}_7$ before and after 1000 cycles of OER.....	69
Figure 4.1: Crystal structure of Sr_3TiMO_7 (M = Ti, Mn, Fe, Co). Green spheres represent La, and red spheres show oxygens. The BO_6 octahedra are shown purple in color.	73

Figure 4.2: Rietveld refinement profiles with powder X-ray diffraction data for (a) $\text{Sr}_3\text{Ti}_2\text{O}_7$, (b) $\text{Sr}_3\text{TiMnO}_7$, (c) $\text{Sr}_3\text{TiFeO}_{7-\delta}$, and (d) $\text{Sr}_3\text{TiCoO}_{7-\delta}$. The experimental data are represented by black crosses. The red line shows the fit. The vertical blue tick marks and the lower pink line correspond to the Bragg peak positions and difference plot, respectively. 76

Figure 4.3: (a) Electrical conductivity variation as a function of temperature. The dotted box has been magnified in the inset to show the conductivity variations for $\text{Sr}_3\text{Ti}_2\text{O}_7$ and $\text{Sr}_3\text{TiMnO}_7$. (b) Arrhenius plots for determination of the activation energies (E_a) for the temperature-activated increase in conductivity. 81

Figure 4.4: HER activity in 0.1 M KOH (a) Polarization curves. (b) Tafel plots. (c) X-ray diffraction data of $\text{Sr}_3\text{TiCoO}_{7-\delta}$, before and after 100 cycles of OER (d) Chronopotentiometry response of $\text{Sr}_3\text{TiCoO}_{7-\delta}$ 85

Figure 4.5: OER activity in 0.1 M KOH (a) Polarization curves. (b) Tafel plots. (c) X-ray diffraction data of $\text{Sr}_3\text{TiCoO}_{7-\delta}$, before and after 100 cycles of OER (d) Chronopotentiometry response of $\text{Sr}_3\text{TiCoO}_{7-\delta}$ 86

Figure 4.6: (a), (b), (c), and (d) cyclic voltammetry in non-Faradaic region in 0.1 M KOH. (e) j_{average} obtained from these CV plotted as a function of scan rate. 88

Figure 5.1: Typical crystal structure of a bilayered Ruddlesden-Popper oxide. In the case of $\text{Ca}_2\text{LaMn}_2\text{O}_7$ and $\text{Sr}_2\text{LaMn}_2\text{O}_7$, the yellow octahedra are MnO_6 units, green spheres represent the sites where La/Ca/Sr reside, and red spheres indicate oxygen. 93

Figure 5.2: Powder X-ray diffraction data for (a) $\text{Ca}_2\text{LaMn}_2\text{O}_7$ and (b) $\text{Sr}_2\text{LaMn}_2\text{O}_7$. Black crosses, orange vertical tick marks, solid red line, and lower pink line correspond to experimental data, Bragg peak positions, the model, and difference plot, respectively... 94

Figure 5.3: Cyclic voltammetry curves from three-electrode measurements for (a) $\text{Ca}_2\text{LaMn}_2\text{O}_7$ and (b) $\text{Sr}_2\text{LaMn}_2\text{O}_7$ 96

Figure 5.4: Cyclic voltammetry curves from three-electrode measurements in 1M KNO_3 and 1M KOH electrolytes at 100 mV/s for $\text{Sr}_2\text{LaMn}_2\text{O}_7$, which has greater pseudocapacitive properties. 97

Figure 5.5: Galvanostatic charge-discharge (GCD) profiles using a two-electrode cell for (a) $\text{Ca}_2\text{LaMn}_2\text{O}_7$ and (b) $\text{Sr}_2\text{LaMn}_2\text{O}_7$ 98

Figure 5.6: (a) Specific capacitance at different current densities. (b) Stability test at current density of 1 A/g for $\text{Sr}_2\text{LaMn}_2\text{O}_7$ 100

LIST OF TABLES

Table 2.1: Refined structural parameters of $\text{Ca}_2\text{LaMn}_2\text{O}_7$ from powder X-ray diffraction data. Space group: $Cmcm$, $a = 19.2814(4) \text{ \AA}$, $b = 5.4609(1) \text{ \AA}$, $c = 5.4113(1) \text{ \AA}$, $R_p = 0.0261$, $wR_p = 0.0341$	33
Table 2.2: Refined structural parameters of $\text{Sr}_2\text{LaMn}_2\text{O}_7$ from powder X-ray diffraction data. Space group: $I4/mmm$, $a = b = 3.8670(1) \text{ \AA}$, $c = 19.9814(10) \text{ \AA}$, $R_p = 0.0415$, $wR_p = 0.0549$	34
Table 2.3: Mn-O bond distances and Mn-O-Mn angles of $\text{Sr}_2\text{LaMn}_2\text{O}_7$ and $\text{Ca}_2\text{LaMn}_2\text{O}_7$	35
Table 3.1: Refined structural parameters of $\text{Sr}_2\text{LaCoMnO}_7$ from powder X-ray diffraction data.....	56
Table 3.2: Refined structural parameters of $\text{Sr}_2\text{LaFeMnO}_7$ from powder X-ray diffraction data.....	56
Table 4.1: Refined structural parameters of $\text{Sr}_3\text{Ti}_2\text{O}_7$ from powder X-ray diffraction data. Space group: $I4/mmm$, $a = b = 3.9009(1) \text{ \AA}$, $c = 20.3386(5) \text{ \AA}$, $R_p = 0.0702$, $wR_p = 0.0949$	76
Table 4.2: Refined structural parameters of $\text{Sr}_3\text{TiMnO}_7$ from powder X-ray diffraction data. Space group: $I4/mmm$, $a = b = 3.8481(1) \text{ \AA}$, $c = 20.2024(6) \text{ \AA}$, $R_p = 0.0446$, $wR_p = 0.0585$	77
Table 4.3: Refined structural parameters of $\text{Sr}_3\text{TiFeO}_{7-\delta}$ from powder X-ray diffraction data. Space group: $I4/mmm$, $a = b = 3.8904(1) \text{ \AA}$, $c = 20.2788(7) \text{ \AA}$, $R_p = 0.0326$, $wR_p = 0.0459$	77
Table 4.4: Refined structural parameters of $\text{Sr}_3\text{TiCoO}_{7-\delta}$ from powder X-ray diffraction data. Space group: $I4/mmm$, $a = b = 3.8682(1) \text{ \AA}$, $c = 20.2349(8) \text{ \AA}$, $R_p = 0.0361$, $wR_p = 0.0545$	78

Table 4.5: B-O bond distances and B-O-B angles for the synthesized structures. 79

Table 4.6: Room temperature electrical conductivities and activation energies..... 83

Table 5.1: Refined structural parameters $\text{Ca}_2\text{LaMn}_2\text{O}_7$ from powder X-ray diffraction data. Space group: $Cmcm$, $a = 19.2820(5) \text{ \AA}$, $b = 5.4614(1) \text{ \AA}$, $c = 5.4116(2) \text{ \AA}$, $R_p = 0.0259$, $wR_p = 0.0335$ 94

Table 5.2: Refined structural parameters of $\text{Sr}_2\text{LaMn}_2\text{O}_7$ from powder X-ray diffraction data. Space group: $I4/mmm$, $a = b = 3.8668(1) \text{ \AA}$, $c = 19.9801(10) \text{ \AA}$, $R_p = 0.0419$, $wR_p = 0.0556$ 95

CHAPTER 1

INTRODUCTION

1.1 BACKGROUND

Perovskite-related oxides are an important class of a family of solid-state materials due to their interesting structural, physical, and chemical characteristics. These oxide materials have been investigated in terms of their structural, ¹⁻³ magnetic, ⁴⁻⁶ charge transport, ⁷⁻⁹ electrocatalytic, ^{10, 11} photocatalytic, sensor, piezoelectric, etc. properties. ¹² Ruddlesden-Popper (RP) oxide is a perovskite derived quasi-two-dimensional oxide structure. RP oxide materials have also been recognized as candidates for a number of applications, including solid oxide fuel cells, batteries, and electrocatalysts, owing to their distinct structural, chemical, and physical characteristics, including thermodynamic stability and mixed ionic electronic conductivity properties. ¹³⁻¹⁶

There are several gaps that must be addressed due to factors including the depletion of fossil fuel sources and the detrimental consequences that fossil fuel use is having on the environment, such as acid rain, land, air, and water pollution. ¹⁷ Consequently, a demand exists for clean, renewable energy sources and technologies. ¹⁷ Moreover, more cost-effective solutions to the energy crisis and negative environmental effects are required. The interesting properties of these perovskites and perovskite-derived oxide materials mentioned above can be beneficial in addressing energy-related challenges and would make ideal alternatives for cost-effective solutions. A few efficient energy technologies in

use include batteries, pseudocapacitors, water electrolyzers, and fuel cells.^{9, 16, 18} RP oxide, which contains a network of atoms constructed in layers, is one example of a material that has been investigated for use in such devices.

1.2 PEROVSKITE OXIDES

The perovskite mineral, calcium titanate oxide, CaTiO_3 was first discovered in 1893 by Gustav Rose, a Russian scientist in the Ural Mountains of Russia.¹⁹ However, the name "perovskite" was eventually given using the name of the Russian mineralogist Lev Perovski, who conducted additional research on the mineral.¹⁹ The general formula of the perovskite is ABO_3 , where A and B are cations. A-site cations have a twelve-coordination to oxygen, whereas B-site cations have an octahedral six-coordination to oxygen. The B-site cations are generally smaller in ionic radius than A-site cations. **Figure 1.1** depicts the unit cell of a simple perovskite, octahedral coordination of the B site and the cuboctahedron coordination of the A site with oxygen. The A site is often composed of s or f block elements, or a combination of those, while transition metals or p block elements comprise the B site. The typical formula for ilmenite is ABO_3 as well. Despite having a similar general chemical formula, the A and B site cations are nearly identical in size, and both have octahedral coordination with oxygen, differentiating from perovskites.

Perovskites are network compounds, which can be explained by the symmetry of the structure. The cubic symmetry is the simplest and most ideal structural symmetry for a perovskite.

The relationship between r_A , r_B , and r_O , which represent the ionic radii of A, B, and O^{2-} , respectively, is true for the ideal perovskite structure.

$$r_A + r_O = \sqrt{2} (r_B + r_O)$$

The relationship shown below, known as the Goldschmidt tolerance factor (t), is dimensionless and can be applied to describe the deviations from ideal cubic structures:

$$t = (r_A + r_O) / \sqrt{2} (r_B + r_O)$$

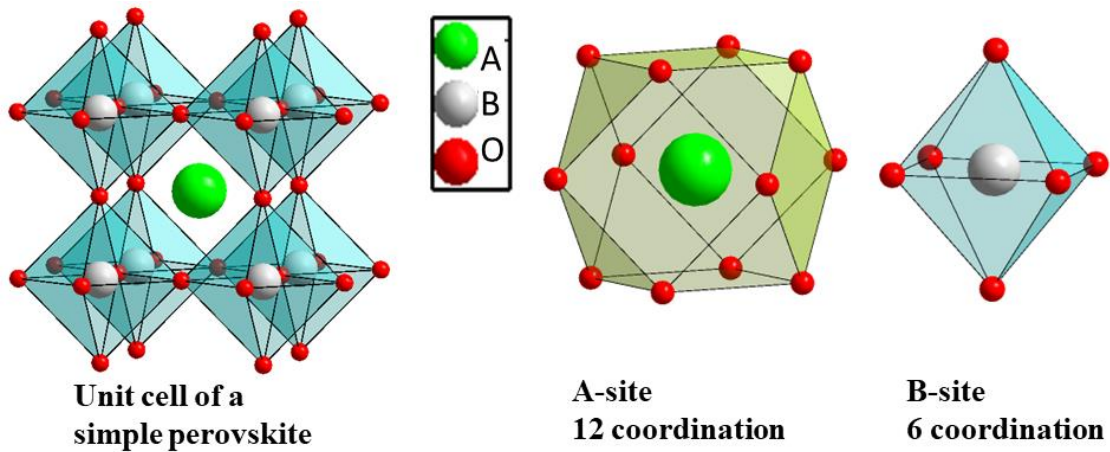


Figure 1.1: The unit cell of a simple perovskite and the coordination of the cations with oxygen

For perovskites, the t value approximately ranges from 0.8 to 1.10, and for an ideal cubic structure, it is closer to 1. The identity of the A and B site ions, influences the structure as well as the size of the ionic radii of the ions.

1.3 PEROVSKITE DERIVED RUDDLESDEN-POPPE (RP) OXIDES

There are different oxide structures derived from the simple perovskite structure, such as oxygen deficient perovskites, brownmillerites, double perovskites and RP oxides.²⁰

The general formula for the quasi-two-dimensional RP structure is $A_{n-1}A'_2B_nO_{3n+1}$, where A/A' is typically a lanthanide or alkaline earth metal, and B is often a transition metal, p-block element, or combination of them. For $n=1$ structures, the term "KNiF₄ type structure" is frequently used, whereas "Ruddlesden popper structures" is used for all phases, including $n=1, 2, 3$, etc. This indicates that A_2BO_4 is the general formula for the first member of the RP oxide family, while $A_3B_2O_7$ is the general formula for the second member. These phases reflect the names of S.N. Ruddlesden and P. Popper, who synthesized and described the Ruddlesden-Popper structure for the first time in 1957.²¹

The two-dimensional RP structure is made up of alternating perovskite stacks and cations along the c -axis. RP compounds are also network compounds where B site has an octahedral coordination with oxygen. A unit cell of an RP oxide and the coordination of the A, A' and B site cations with oxygen are shown in **Figure 1.2**. Contrary to the basic perovskite structure, the A site has two distinct crystallographic positions, within (A) and between (A') the perovskite stacks. While the A-site cations between the stacks of perovskites have a coordination of nine with oxygen, those within the perovskites have a coordination of twelve with oxygen as illustrated in **Figure 1.2**.

The flexibility of RP oxides to have oxygen vacancies in their structures, is similar to that of perovskites.^{22, 23} Furthermore, they can store oxygen interstitials in the spaces between the perovskite stacks.¹¹ A range of A- and B-site aliovalent cation replacements, synthesis conditions, and other parameters can result in RP oxides that are either oxygen-deficient or oxygen-excessive with varying functional properties, as explained in the following sections.

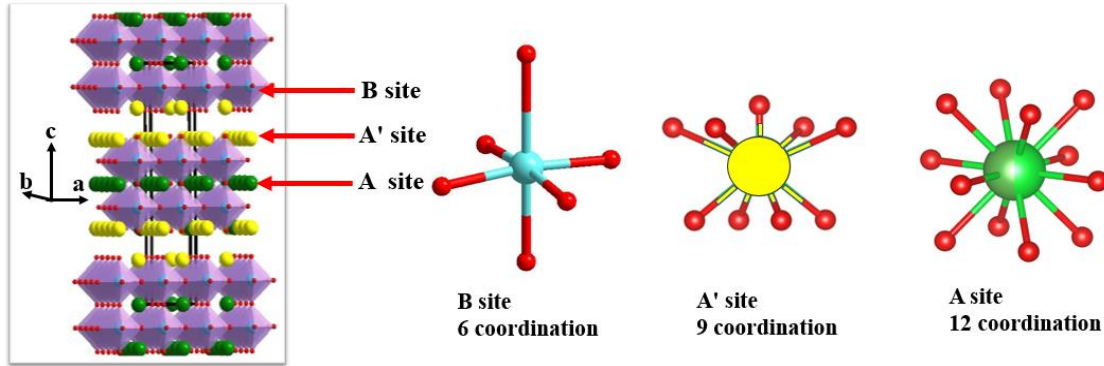


Figure 1.2: The unit cell of a RP structure and the coordination of the cations with oxygen.

1.4 PROPERTIES OF PEROVSKITES AND PEROVSKITE-DERIVED RP OXIDES

Perovskite and derived oxides are recognized for demonstrating a diverse range of structures and properties.²⁴ The symmetry of the structure, which describes how the atoms of a structure are organized with respect to one another, has a significant impact on the physical and chemical properties of these oxides.²⁴⁻²⁷ Nevertheless, it is always possible to modify these properties by using different synthesis methods, using different metal element substitutions at the A- and B-site, and incorporating oxygen vacancies and excess into the perovskites and derived oxides.²⁸

1.4.1 ELECTRICAL CHARGE TRANSPORT

The electrical conductivity is affected by the band structures and the density of states (DOS).²⁹ The highest occupied band and the lowest unoccupied band, respectively, are two distinct bands known as the valence band and the conduction band. Conductivity occurs by the promotion of electrons from the valence band to the conduction band. The Fermi level

is a hypothetical energy level which, at thermodynamic equilibrium, has a 50% probability of always being occupied by electrons. The Fermi level must cut through the conduction band to create a partially filled band for it to be a high-electronic conducting material (metal). A band gap between the valence and conduction bands is a characteristic of insulating or semiconducting materials, causing the compound to be a poor conductor. The material becomes a poorer conductor as the band gap expands. In semi-metallic materials, the energy gap between the valence and conductive bands is zero, demonstrating intermediate characteristics between metals and insulators.

There are microscopic factors, which affect the electrical conductivity, σ in addition to these band structures.³⁰

$$\sigma = ne(e\Gamma/m^*)$$

The terms n , e , Γ , and m^* in the above equation, stand for the carrier concentration (cm^{-3}), the electron charge (1.602×10^{-19} C), relaxation time (The amount of time needed for a material to relax into an equilibrium state with zero current after the electrical field that generated the current has been switched off), and effective mass of the electron (kg), respectively. In metals, carrier concentration slowly rises with temperature and there are more atom-electron vibrations and collisions, which drives the relaxation time to be inversely proportional to temperature thus causing conductivity to decrease as a function of temperature. Carrier concentration in semiconductors increases as temperature rises due to excitations across band gaps.³¹ Despite having an inverse relationship of Γ with temperature, the conductivity of semi-conductor will increase due to the exponential relationship between carrier concentration and temperature.³¹

In perovskites and perovskite-derived oxides such as RP oxides, the B-O-B bond oversees electronic conduction via electrons or holes through the network of structures.³² The exchange of electrons and holes is determined by the interaction of the O-2p orbital with the d orbitals of the B-site.³² The conductivity will enhance when the overlap between the O-2p and metal 3d increases. In general, for better charge transfer and higher conductivity, a shorter bond length for B-O and a larger bond angle for B-O-B are required.³²⁻³⁵ A key element in the electron conductivity is the presence of multivalent cations at the B-site.³⁶ Polaron hopping mechanism is a well-known electrical conduction mechanism.³⁶ The polaron hopping conductance mechanism is often involves electron hopping between transition-metal ions in different valence states (e.g., V^{4+} -O- V^{5+}), where the charge carriers are actually small polarons.³⁷ However, there are other factors, such as crystallite size and defects in the structure, that affect the conductivity of these types of oxides. For example, the larger particle size perovskite, $La_{0.5}Sr_{0.5}Al_{0.2}Fe_{0.8}O_{3-\delta}$ has been demonstrated to have better conductivity than the smaller grain size perovskite $La_{0.5}Sr_{0.5}Co_{0.2}Fe_{0.8}O_{3-\delta}$.³⁶ In addition, ion migration pathways for oxygen ion conducting materials have been explored for the oxygen ion migration, which is promoted by oxygen vacancies or oxygen excess in the structures.³⁸

RP oxides are mixed ionic electronic conductors.^{39, 40} Oxygen interstitials and oxygen deficiencies can exist in between and within the perovskite stacks respectively, which facilitate the transport of oxygen ions. The structural features of the RP oxides cause anisotropic oxygen migration, which is an intrinsic property of the RP oxide.⁴⁰ Different metal cation doping at the A-site and B-site and can be used to modify the electrical conductivities of the RP oxides.³⁹ For example, correlations have been observed between

the band gap of some RP oxides and the ionic radii of B-site metals.²⁹ Moreover, the changes in charge transport and thermoelectric properties as a function of A and B site metals have been demonstrated in some of the studies.^{41, 42}

In this study, the conductivity variations with varying temperature have been studied for the bilayer RP oxides with different A- and B-site cation substitutions.

1.4.2 MAGNETIC PROPERTIES

Unpaired electrons are commonly associated with magnetic properties in materials. The incomplete orbital filling of d-block elements at B-sites, which are often transition metals is related to the magnetic characteristics of perovskites.⁴³ The geometries around the A- and B-site metal cations are also significant as they influence the orbital energy levels.⁴³ Importantly, the magnetic characters of metal elements and ions are caused by electron spin states, which are affected by crystal field interactions.^{43 44}

The terms paramagnetic, ferromagnetic, antiferromagnetic, and ferrimagnetic refer to four different types of magnetic behaviors. In paramagnetic, the electron spins are in random orientations. The magnetic moments in antiferromagnets are opposite and parallel to each other to cancel out the moments, while the electron spins in ferromagnets are aligned in the same direction. The magnetic moments of ferrimagnets are aligned in opposite directions with a net magnetic moment, where the magnetic moments do not completely cancel each other due to the difference in magnitude of the opposing moments. Moreover, there are other reported magnetic phenomena, including spin-glass magnetism, superparamagnetism, and metamagnetism.^{45, 46}

The Curie-Weiss law is followed by paramagnetic materials with locally and weakly interacting electrons as shown by below equation. The variables χ_m , C, and T in the equation represent molar susceptibility, Curie constant, temperature, and the Weiss constant, respectively.⁴⁷

$$\chi_m = C/(T-\theta)$$

The magnetic ordering variations of the materials can be found using the curves χ_m vs T or $1/\chi_m$ vs T.

Perovskites and perovskite derived RP oxides exhibit various complex magnetic behaviors.^{43 44 46} The magnetic characteristics of the materials have been modified by changing the elements used in the A-site and B-site.^{43 48, 49} For instance, the magnetic characteristics of the compound $\text{Sr}_3\text{Mn}_{2-x}\text{Fe}_x\text{O}_{7-\delta}$ have been investigated while varying the Fe concentration. These structures have been shown very complex magnetic behaviors and when x was greater than 0.5, these phases revealed transitions with spin-glass-like characteristics at low temperatures.⁵⁰ In this study, the magnetic property variations with different A- and B-site cation substitutions have been studied for the bilayer RP oxides.

1.4.3 ELECTROCATALYTIC PROPERTIES

Perovskites are useful in the catalysis of different reactions due to their exceptional catalytic activity and superior chemical stability.^{10, 11} The perovskite structure enables the formation of compounds containing a wide range of elements with multiple valence states, which can then be tuned for enhanced electrocatalytic activity. The transition metal at the B-site acts as the active site of the catalyst in perovskites and derived RP oxides.^{51, 52 27, 53-}

⁵⁵ Moreover, the presence of oxygen vacancies in materials may cause the gap between the metal-3d band center (M_d) and the oxygen 2p band center (ΔE_{d-p}) to be reduced by bringing the M_d center close to the Fermi level.^{35, 56}

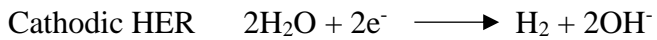
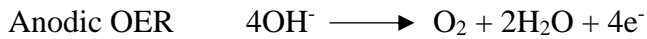
There are two half reactions for water splitting. The reactions are known as the oxygen evolution reaction (OER) and the hydrogen evolution reaction (HER) based on the two primary products of the water splitting. The overall water splitting reaction is shown below.



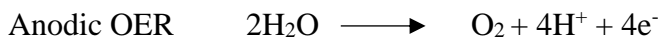
Both acidic and alkaline electrolytes are used in the water splitting reaction. Thus, based on the electrolyte, the OER and HER reactions have been considered separately below.^{35,}

^{57 58, 59}

In alkaline electrolyte,



In acidic electrolyte,



Thermodynamically, hydrogen evolution takes place ideally at the potential of 0 V versus the reversible hydrogen electrode ($E_{\text{H}_2/\text{H}_2\text{O}}$, 0 V vs. RHE). The minimum potential required for generating oxygen by splitting water is 1.23V versus the RHE. ($E_{\text{O}_2/\text{H}_2\text{O}}$, 1.23 V vs. RHE).

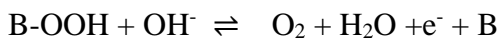
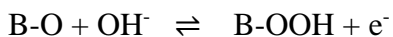
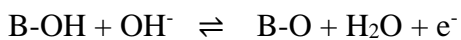
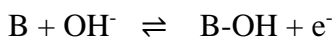
Two main different mechanisms have been established for the OER, namely Adsorbate evolution mechanism (AEM) and the Lattice oxygen mediated mechanism (LOM).^{35, 57}

AEM mechanism involves the adsorption of OH on B-site metal, which then dissociates further to form adsorbed O in the second step. In the third step, the adsorbed O combines with a different water molecule to create adsorbed OOH on a surface metal cation, which results in the evolution of O₂ (g).

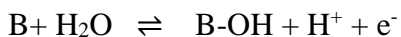
In the LOM, OH is first adsorbed at the metal B-site, then it is deprotonated to form an OO intermediate where one oxygen is received from the lattice. This procedure results in the formation of an unstable lattice oxygen vacancy. The vacant site is thus filled by another OH. The OH linked to the vacancy site undergoes deprotonation to regenerate the catalyst, and the reaction continues.

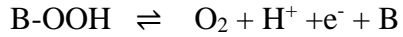
Below are the reaction steps of the AEM mechanism suggested for the OER at alkaline and acidic conditions where B is the active site of the catalyst.^{35, 57 58, 59}

OER mechanism in alkaline medium,



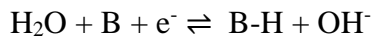
OER mechanism in acidic medium,



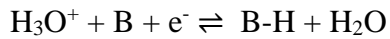


The widely recognized mechanism for the HER consists of two phases, starting with the Volmer reaction and continuing with either the electrochemical Heyrovsky reaction or the chemical recombination step, the Tafel reaction, as shown below, where B stands for the catalyst.²³

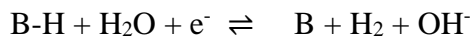
Volmer reaction in alkaline conditions,



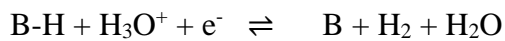
Volmer reaction in acidic conditions,



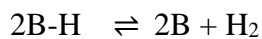
Heyrovsky reaction in alkaline conditions,



Heyrovsky reaction in acidic conditions,



Tafel reaction in both alkaline and acidic conditions,



OER is known to be the bottleneck of the water splitting reaction as it requires 4 electrons to be transferred during the mechanism, whereas the HER mechanism only transfers 2

electrons.⁵⁹ For cost-effective large-scale applications, the search for a better catalyst for water splitting is ongoing due to the scarcity and high cost of Pt and precious metal-based oxides, such as RuO₂ and IrO₂, which are the known effective catalysts for OER-HER. The electrocatalytic performance of earth abundant multi-metal oxides has been extensively studied to enhance the catalytic activities of the materials by using different strategies, such as surface and structural alterations, composite fabrication, defect engineering, and strain engineering.^{55, 60, 61} In previous studies, the relationship between crystal structure symmetry and electrocatalytic activity has been demonstrated in perovskite oxide materials. For example, the electrocatalytic activity of cubic SrMnO₃ has been shown to be significantly better than that of hexagonal SrMnO₃, highlighting the impact of crystal structure symmetry.²⁵ Moreover, in another study, it was shown that in the transition from Sr₂FeCoO_{6-δ} (disordered) to CaSrFeCoO_{6-δ} (ordered) and Ca₂FeCoO_{6-δ} (highly ordered), there is a systematic enhancement of the electrocatalytic activity.²⁶

It has been shown in various previous studies that the electrocatalytic properties are related to compositional modifications of these type of oxides.^{23, 62-65} For example, the electrocatalytic activity of the single-layered RP oxide, La_{0.5}Sr_{1.5}Ni_{1-x}Fe_xO_{4±δ} has been reported by changing the degree of Fe substitution at the B-site, where all materials in the series crystallized in the same space group. The compounds that contain Fe at the B-site showed improved electrocatalytic activity than the parent compounds, La_{0.5}Sr_{1.5}NiO₄ and La_{0.5}Sr_{1.5}FeO₄.⁶⁶ In another previous study, the catalytic activity of La_{1.5}Sr_{0.5}Ni_{0.5}Co_{0.5}O₄, showed better performance than that of the parent compound, La_{1.5}Sr_{0.5}NiO₄ which emphasizes the importance of the B-site for the electrocatalytic performance of the perovskite-derived oxides.¹¹

In another previous study, the structural changes are reported for the $\text{Sr}_2\text{Mn}_2\text{O}_6$ and $\text{CaSrMn}_2\text{O}_6$ by changing the A-site, which are hexagonal $P6_3/mmc$ and cubic $Pm-3m$, respectively. The OER electrocatalytic activity of the latter material is significantly enhanced compared to the former.⁶⁷

This work investigates the electrocatalytic properties of bilayer RP oxides with different A- and B-site cation substitutions, as well as the effect of oxygen vacancies.

1.4.4 PSEUDOCAPACITIVE ENERGY STORAGE PROPERTIES

The demand for energy storage and delivery in our daily lives is rising due to the requirement to power an expanding range of portable electronics and electric vehicles. Additionally, when renewable energy conversion technologies like wind turbines and photovoltaics are used extensively, energy storage solutions are required to balance temporal changes that can span anywhere from a few seconds to many hours.⁶⁸ Therefore, electrochemical energy storage materials that can deliver both high power and high energy density is essential.

Traditionally, batteries provide high energy density but low power density. In contrast to batteries, electrical double-layer capacitors (EDLC),⁶⁹ a subclass of supercapacitor, have a higher power density but lower energy density. However, another class of supercapacitor, i.e., pseudocapacitors, are an intermediate between batteries and EDLCs in terms of energy density and power density. In contrast to EDLCs, which store charge non-faradaically, pseudocapacitive materials store the charge faradaically.^{70, 71} In pseudocapacitors, high

specific capacitance and energy density are achieved by storing energy via reversible surface or near-surface electron transfer processes.

In addition, the faradaic processes, which happen near the surface without experiencing the bulk diffusion, are responsible for the high-power density of pseudocapacitors.⁷²

The pseudocapacitive properties have been observed in various materials, such as metal oxides, nitrides, sulfides, and hydroxides.⁷² They can be categorized based on three different mechanisms namely, underpotential deposition, redox, and intercalation.⁷² The pseudocapacitance generated via adsorbed metal ion monolayer on the surface of another metal, above their redox potential is known as underpotential deposition. The redox pseudocapacitance is the result of electrochemical adsorption of ions on or near surfaces at redox active sites with successive electron transfers. In intercalation mechanism, electroactive species intercalate into a material without a crystallographic phase change.

Among perovskite-based oxides, the oxide ion intercalation has been studied.^{70, 71} Examples of the materials studied for this purpose include $\text{CaMnO}_{3-\delta}$,⁷³ $\text{Ca}_2\text{MnO}_{4-\delta}$,⁷³ $\text{LaNi}_{1-x}\text{Fe}_x\text{O}_{3-\delta}$,⁷³ $\text{Ca}_3\text{GaMn}_2\text{O}_8$,²⁷ and $\text{SrLaFe}_{1-x}\text{Co}_x\text{O}_{4-d}$.²² The charge storage in perovskites and similar oxides is facilitated by oxygen intercalation in the alkaline electrolyte. As shown in the below equations, the B-site transition metal centers of the perovskite are directly oxidized by oxygen anions from the electrolyte.⁷³



Fundamentally, the mechanism of pseudocapacitive anion intercalation in perovskite oxides is quite significant. Many studies on perovskites and derived oxides have been

conducted to investigate their respective pseudocapacitive energy storage performances in alkaline medium.^{22, 27, 70, 71, 73}

The pseudocapacitance properties shown by the perovskite and derived oxides have also shown correlations with different A and B-site cation substitutions.^{12, 74} Perovskite oxides with cubic, tetragonal, orthorhombic and hexagonal structures have been investigated in an attempt to examine the effect of structure on pseudocapacitance.⁷⁴

The anion-intercalated pseudocapacitive properties of bilayer RP oxides with various A substitutions and symmetry variations were researched in this study.

1.5 MATERIAL SYNTHESIS METHODS

1.5.1 SOLID STATE SYNTHESIS

Solid-state synthesis is a method of producing solid materials, typically crystals, by reacting substances in a solid state rather than in a liquid or solution. The method is commonly used in the production of semiconductors, ceramics, and other materials with specific properties. The solid-state synthesis method offers advantages over some other synthesis methods, such as high purity, reduced contamination, and improved reproducibility.

Diffusion is the limiting factor for the solid-state reaction. High temperatures are therefore required for the reaction to take place to diffuse or transport the species through the medium. This process often involves heating and cooling the reactants, sometimes under pressure, to encourage the atoms to bond together into a solid material. Rates of these

reactions usually depend on three factors: the area of contact between reacting solids, the diffusion rate, and the rate of nucleation of the product phase. The conventional solid-state synthesis involves several steps.

For a solid-state reaction, usually starting materials are either oxides or carbonates. During the heating step, CO₂ will escape from the carbonates, which end up as oxides. The oxidation states of the precursor oxides and carbonates should be considered while selecting the precursor materials.

The weighed powders need to be thoroughly mixed. This grinding and mixing are important as poor mixing can prevent compounds from forming, by preventing proper contact between metal ions to form the preferred network.

The ground mixture will then be pelletized using a pellet die. The reason of this step is to bring these particles together using a high-pressure pelletizer and form a pellet, enhancing the intimate contact of the reactants with each other to form the product.

The diffusion limitation can be overcome by using high temperatures. During heating, it is required to place the pellet in a ceramic crucible, which can operate at very high temperatures (~1750 °C) making this ideal for high temperature applications. This step of the reaction process is carried out in a high-temperature furnace. The samples need to be heated at high temperatures for prolonged hours to obtain the desired product. If the sample is not pure after one heating and cooling cycle, it must be reground, repelletized, and refired for several hours again. This process must be repeated until the pure product is obtained.

The two primary types of furnaces used in heating are box and tube furnaces. Based on the conditions required for the reaction to take place, the furnace can be selected. Syntheses

can be conducted in a variety of environments, including argon, oxygen, hydrogen, and air. The advantage of using a tube furnace is that the required type of gas can be passed through the tube at high temperatures during the reaction, assisting the optimum conditions for the reaction. Based on the oxidation states of the B-site (transition metals), the environment can be determined. For instance, if Mn should be present in the compound as Mn^{3+} rather than Mn^{4+} , an argon environment can be used to prevent the oxidation of Mn^{3+} to Mn^{4+} . On the other hand, an oxygen or an air environment can be utilized if the B-site demands a higher valence state. A H_2 environment can be used when reducing conditions are required.

1.5.2 SOL-GEL SYNTHESIS

Sol-gel synthesis is a process that produces solid materials from a solution (sol) through a gelation(gel) process. In the process, chelation agents such as citric acid and EDTA are added to facilitate the formation of homogenous crystalline particles.⁷⁵ The sol-gel process involves the transformation of a sol, which is a colloidal suspension of particles in a liquid, to a gel, which is a three-dimensional network of cross-linked nanoparticles. Finally, the gel is dried and subjected to thermal treatment to remove any remaining solvent and the chelating agent and produce a solid material with a well-defined microstructure.

The sol-gel method is a versatile technique that can be used to produce a wide range of materials, including glasses, ceramics, and composites, with a high degree of control over their composition, structure, and properties. This is achieved by manipulating the chemical composition of the sol, the processing conditions, and the post-processing treatments.

The sol-gel process typically involves the following steps:

1. Hydrolysis: The precursor materials are dissolved in a solvent and undergo hydrolysis, which breaks down the precursor molecules into smaller components that can react with each other.
2. Condensation: The hydrolyzed precursors then undergo condensation, which forms bonds between the smaller components and creates a three-dimensional network of cross-linked particles.
3. Gelation: As the concentration of the network increases, the sol undergoes gelation, transforming from a liquid to a solid material.
4. Drying: The gel is then dried to remove any remaining solvent and form a solid material.

Sol-gel synthesis has some advantages over some other methods, including low-temperature processing, high purity, stabilizing metastable phases, creating products with small crystallites and high surface areas, and uniformity of composition and structure. However, sometimes finding the proper reagents can be a challenge. For example, ions such as Ta^{5+} and Nb^{5+} immediately hydrolyze and precipitate in aqueous solution.

1.6 CHARACTERIZATION TECHNIQUES

1.6.1 POWDER X-RAY DIFFRACTION

Powder X-ray diffraction (PXRD) is a powerful analytical technique to determine the crystal structure of a material. It is based on the principle that when X-rays pass through a crystalline material, they are diffracted by the regularly arranged atoms in the crystal

lattice, producing a unique diffraction pattern. This pattern is a series of peaks that correspond to the atomic arrangement of the crystal and provides information about the crystal structure, phase purity, and crystallinity of the sample. PXRD is a non-destructive technique and requires very little sample preparation, making it a valuable tool in materials science and chemistry research. It is commonly used to identify unknown compounds, determine the purity and crystallinity of a material, and monitor phase changes during chemical reactions and manufacturing processes.

As shown in the Figure below, there are sets (or families) of hypothetical planes that intersect lattice points. All planes in the family are parallel to each other and equally spaced. These distances between the neighboring planes are called “d-spacing” and described using three h , k , and l Miller indices, which are enclosed in parentheses (hkl) .

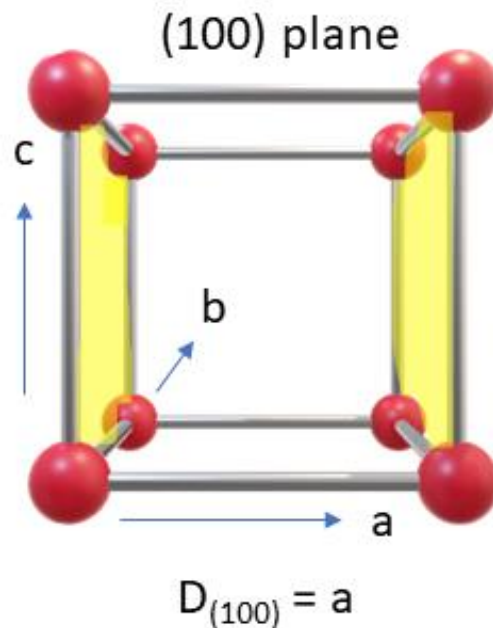


Figure 1.3: A set of lattice planes (100) in a unit cell.

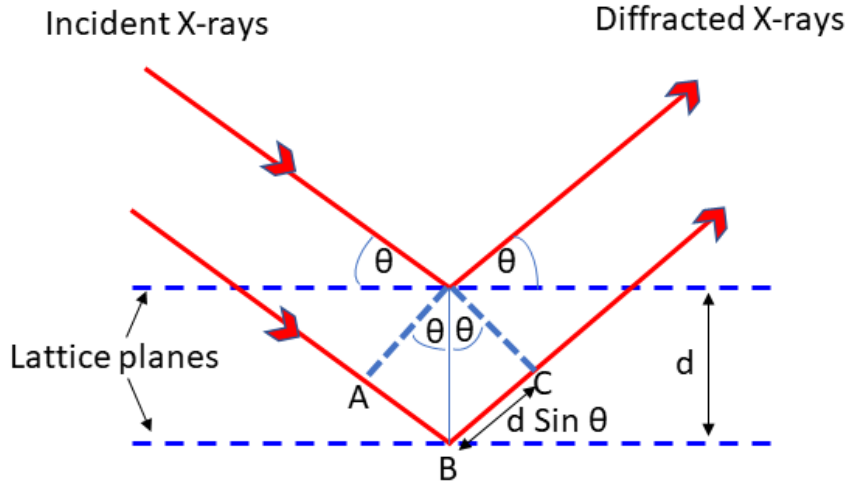


Figure 1.4: A graphical representation of Bragg's Law.

According to the Bragg's law, $2d \sin \theta = n\lambda$, a diffraction peak would only be achieved by constructive interference between the diffracted beams. The difference in the path travelled by beams need to be an integer of the wavelength to give constructive interferences.

A search-match process is used to compare the observed pattern with the entries in reference databases during the processing of powder XRD information to determine the phase purity. The Rietveld refinement is then performed for the powder XRD data obtained, using GSAS software⁷⁶ with EXPIGUI interface⁷⁷. FullProf and Topaz are more examples of fitting software tools that can be used to fit the powder XRD data collected. Ultimately, these investigations provide precise crystallographic information about the interstitial locations, vacancies, and atom site occupancies of the materials.

Overall, PXRD is a valuable tool for understanding the atomic structure of materials, providing insights into their physical and chemical properties, and aiding in the design and development of new materials with desired properties.

1.6.2 ELECTRICAL CONDUCTIVITY MEASUREMENTS

Alternating current (AC) and direct current (DC) conductivity measurements can be used to investigate the electrical charge transport properties of perovskite oxides. Electrical conductivity measurements are used to determine how easily an electrical current can pass through a material. This property is important in many fields, including materials science, chemistry, and electrical engineering. Overall, electrical conductivity measurements are a valuable tool for understanding the properties of materials and designing electrical systems.

There are different techniques for measuring electrical conductivity, including the four-probe method and the two-probe method. Both two and four probe techniques are used in DC and AC measurements, with AC measurements being especially significant for better understanding the ionic conduction process.^{1, 14} The electrochemical impedance spectroscopy method is used in the AC analysis rather than the DC measurement approach explained below.⁷ Impedance is the electrical resistance that opposes the flow of electric current in a system when applying the alternating current, analogous to resistance for direct current.

Each method has its own advantages and disadvantages.⁷⁸ The DC four-probe method uses four closely spaced electrodes to measure the voltage drop across the sample, which allows

for accurate measurements of the resistivity and conductivity as this method prevents contribution from the contacts and the wires connected.⁷⁹. The conductivity can be calculated using the following equation from the four-probe conductivity measurements by measuring the current while applying a voltage, as shown in **Figure 1.5**.

$$\sigma = \left(\frac{I}{V}\right) \left(\frac{L}{wh}\right)$$

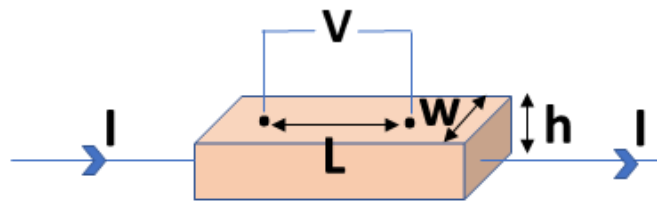


Figure 1.5: The four - probe conductivity setup.

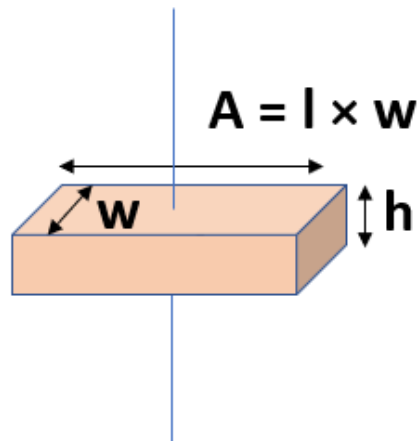


Figure 1.6: The two - probe conductivity setup.

The two-point probe method is simpler than the four-point probe method, however often the conductivity values from the two methods are similar, especially for many materials with low or moderate conductivity.⁸⁰ This method uses two electrodes to measure the voltage drop across the sample, and the resulting resistance is used to calculate the conductivity. By measuring the current at various temperatures while using a constant voltage, as shown in **Figure 1.6**, the conductivity was calculated according to the formula below from the two-probe conductivity measurements.

$$\sigma = \left(\frac{I}{V}\right) \left(\frac{h}{A}\right)$$

In this study, DC studies were carried out using two-probe measurements to analyze the electrical charge transport properties of the materials over a range of temperatures. In addition, the charge transfer resistance during electrocatalytic properties was investigated by applying impedance analysis using AC measurements.

1.6.3 MAGNETIC MEASUREMENTS

The physical property measurement system (PPMS) is a scientific instrument that is used to measure the physical properties of materials such as magnetism, electrical conductivity, thermal conductivity, and specific heat capacity.⁸¹ PPMS typically consists of a cryostat that can sustain extremely low temperatures (often down to a few Kelvin) and a variety of measuring probes that can be inserted into the sample space of the cryostat. The probes are used to measure the various physical properties of the sample as it cools or heats up.

PPMS instruments are extremely useful for researching material behavior in various situations, such as in the presence of a magnetic field or at extremely low temperatures.⁸¹

⁸² In this study, magnetic measurements were carried out using a PPMS. On a vibrating sample magnetometer, magnetic susceptibility measurements were acquired in the temperature range of 2 to 400 K under a known applied magnetic field. Data were acquired for each material by lowering the temperature without the external magnetic field (zero field cooled: ZFC) and with the external field (field cooled: FC). Isothermal field-run experiments were also carried out in a range of magnetic fields.

1.6.4 IODOMETRIC TITRATION

Iodometric titration is performed to determine the oxygen stoichiometry of the compounds. This is a well-established method to study the oxygen vacancies or excess oxygen in the oxides.^{28, 83}

In the first step in this method, a known amount of the oxide sample is dissolved in HCl acid with excess KI. Before mixing the sample and the KI, the acid solution is bubbled with argon gas for some time to remove any dissolved oxygen gas in the acid solution. Upon mixing, the transition metal ions (Aliovalent cations) at the B-site will be reduced to their most stable lowest oxidation state while oxidizing the I^- into I_2 . The reaction mixture should be kept overnight to completely undergo the redox reactions.

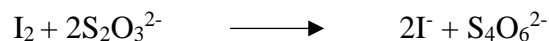
The liberated I_2 in the reaction mixture is then titrated against $Na_2S_2O_3$ solution (concentration should be known), using a known volume of the overnight reacted reaction

mixture. A starch solution is used as an indicator near the endpoint of the titration. The color change from blue to colorless is the indication of the endpoint.

All the steps of the titration need to be performed under inert Argon atmosphere. Calculations are based on the conversion of transition metal ions into their most stable lowest oxidation state, due to the excess KI as shown in the equation below. The below shown equation is just an example, as transition metals can have different oxidation states depending on the oxygen content or the A-site metal type.



The reaction between the formed I_2 and $Na_2S_2O_3$ during the titration is shown below.



The A site mostly has a constant valence state. The consumed moles of titrant ($Na_2S_2O_3$) to titrate a known volume of the titrand were determined based on the concentration and titration volume of $Na_2S_2O_3$. The amount of oxygen that was lost due to the reduction of the metals is equivalent to the amount of I_2 that is titrated by $Na_2S_2O_3$. The amount of oxygen in total is consequently equal to the sum of the oxygen that is still present (to maintain the charge of the reduced B-site cation) and the oxygen that is lost (due to the reduction of B-site cations).

1.6.5 SCANNING ELECTRON MICROSCOPY

Scanning electron microscopy (SEM) is a powerful imaging technique that uses a beam of electrons to scan the surface of a sample to create high-resolution images. The surface of the sample is scanned by a focused beam of electrons in SEM, and any scattered or emitted

electrons are detected by a detector. The intensity of the detected electrons is used to create an image of the surface topography and composition of the sample. SEM images are a useful tool due to their ability to provide a number of details regarding the morphology, dimension of the crystals, and shape of materials.

Energy dispersive X-ray (EDX) detection is an additional feature of SEM. A sample is subjected to an electron beam during an EDX analysis, which causes positively charged holes to be left behind after the electron beam strikes the inner shell of an atom, knocking electrons out of the shell. When one electron is removed, the empty space is filled by pulling another electron from an outer shell. This energy difference can be emitted in the form of an X-ray as the electrons transfer from the outer, higher-energy shell of the atom to the inner, lower-energy shell. Since the energy of these X-rays is distinctive to the elements in the sample, it allows to identify the elements and determine their relative abundance. A detector that monitors the energy and intensity of the X-rays generated from the sample is used to detect the X-rays. EDX has a high spatial resolution and sensitivity for information on the elemental composition of a sample. The distribution of elements inside a sample can therefore be mapped using EDX to study the spatial variation in composition.

1.6.6 X-RAY PHOTOELECTRON SPECTROSCOPY

The elemental composition and chemical state of the elements present in a sample can be determined using the surface-sensitive analytical method known as X-ray photoelectron

spectroscopy (XPS). In XPS, a sample is bombarded with X-rays, and the electrons in the inner shell can be ejected due to the high energy supplied. These ejected electrons are called photoelectrons. The energy of the photoelectrons is measured, and the resulting spectra provide information about the elements present in the sample as well as their chemical states. The XPS measurements were carried out to study the compositions and oxidation states of the A and B-site cations and to see the stability of the structures before and after electrocatalyzing the oxygen and hydrogen evolution reactions.

1.6.7 RAMAN SPECTROSCOPY

The vibrational states of a sample can be found and studied using the powerful, non-destructive, relatively quick, and simple analytical technique known as Raman spectroscopy. In Raman spectroscopy, a laser beam is focused on a sample, and the light that is reflected back is examined for variations in wavelength that are indicative of change in polarizability during the vibrations of the material. Raman shifts are these changes in wavelength that give information about the chemical composition and structure of the sample. It can be used to identify the functional groups present in a compound, as well as to determine the crystallinity of a sample. The Raman spectroscopy measurements were carried out to study the stability of the RP structures before and after electrocatalyzing the oxygen and hydrogen evolution reactions.

1.7 APPLICATION OF THE ABOVE TOPICS IN THIS WORK

The concepts described above have been applied to this work, as follows.

The observations of magnetic property variations and electrical charge transport variations have been explored in this chapter 2 by changing the A-site of the RP materials. It was interesting to note that this A-site substitution resulted in a substantial structural change, which affected the functional properties of the materials. Furthermore, the effect of A-site cation change on electrocatalytic activity toward oxygen and hydrogen evolution reactions has been thoroughly investigated in this chapter.

In chapter 3, two of the interesting bi-layered RP oxides have been synthesized by changing the B-site transition metal. This chapter provides a thorough explanation of how the B-site affects the electrical, magnetic, and electrocatalytic properties of the two materials.

In chapter 4, the electrocatalytic activities of a series of bilayer RP materials, $\text{Sr}_3\text{Ti}_{2-x}\text{M}_x\text{O}_{7-\delta}$ ($\text{M} = \text{Mn, Fe, Co}$; $x = 0, 1$), for water electrolysis have been studied. In addition, the effect of oxygen-vacancies and their correlations with electrocatalytic and charge-transport properties have been thoroughly discussed in this chapter.

In chapter 5, the effect of changing the A-site cation on the pseudocapacitive properties generated via oxygen ion-intercalation in the alkaline electrolyte environment, of bi-layered RP structures has been thoroughly discussed.

CHAPTER 2

EFFECT OF STRUCTURAL SYMMETRY ON MAGNETIC, ELECTRICAL, AND ELECTROCATALYTIC PROPERTIES OF ISOELECTRONIC OXIDES $A_2LaMn_2O_7$

(A= Sr²⁺, Ca²⁺)¹

2.1 EXPERIMENTAL

2.1.1 SYNTHESIS

$Sr_2LaMn_2O_7$ and $Ca_2LaMn_2O_7$ were prepared by solid-state synthesis method using powders of $CaCO_3$, $SrCO_3$, La_2O_3 , MnO_2 , Fe_2O_3 and CoO . The stoichiometric amounts of oxides/carbonates were mixed thoroughly using agate mortar and pestle. The mixtures were pressed into pellets and heated at 1300 °C in air for 24 hours. The samples were then re-ground and re-pelletized to be heated at 1300 °C for a total of 72 hours in air with two intermittent grindings and pelletizing. The heating and cooling rates of the furnace for all samples were 100 °C/hour.

2.1.2 CHARACTERIZATION

The synthesized materials were characterized using a high-resolution X-ray diffractometer with Cu $K\alpha_1$ ($\lambda = 1.54056 \text{ \AA}$). The data were collected in the 2θ range of 10 - 80°. Rietveld refinements for the X-ray diffraction (XRD) data were carried out using GSAS software⁷⁶

¹ The work described in this chapter was published in J Phys Chem Solids 2022, 171, 111013.

and the EXPGUI interface.⁷⁷ The electrical conductivity measurements were conducted by two-probe direct current method using an applied potential of 0.01 V. Magnetic susceptibility data were obtained in the temperature range of 2 to 400 K with an applied magnetic field of 1000 Oe on a vibrating sample magnetometer. For each material, data were obtained by lowering the temperature without the external magnetic field (zero field cooled: ZFC) and with the external field (field cooled: FC). Isothermal field-run measurements were also performed in magnetic fields of 0 – 9 T. Iodometric titrations⁴² were performed to examine the oxygen stoichiometries of the two materials.

2.1.3 ELECTROCHEMICAL OER/HER STUDIES

The catalyst ink of each material was prepared by mixing 35 mg of the powder sample, 7 mg of carbon black powder (Fuel Cell Store), 40 μ L Nafion® D-521 solution (Alfa Aesar, 5% w/w in water and 1-propanol), and 7 ml of tetrahydrofuran (Alfa Aesar, 99%). The mixture was then sonicated for 30 minutes. A glassy carbon electrode (GCE, 5 mm diameter, 0.196 cm² area, HTW Germany) was used as the working electrode. Prior to use, it was cleaned using aluminum oxide polishing solution (Allied Hightech Products Inc.) on a polishing cloth, followed by sonication for 2-3 minutes in ethanol (Decon Labs, Inc.). At the end of the polishing steps, the GCE was washed with deionized water and dried. Then 20 μ l of the prepared catalyst ink was drop-casted on the surface of the GCE by placing two coats of 10 μ l with a 2-minute interval. Total catalyst mass loading on the GCE was 0.1 mg. The GCE was then left overnight to air-dry before running the OER/HER electrochemical measurements.

The electrochemical OER/HER experiments were carried out on a standard three-electrode cell using an electrode rotator at 1600 rpm. Commercial Ag/AgCl electrode in 1 M KCl (CH instruments, Inc., TX, USA) and 4 M KCl (Pine Research instruments) were utilized as reference electrodes for OER and HER experiments, respectively. A platinum electrode (Pine Research Instruments) and a carbon electrode were used as counter electrodes for the OER and HER measurements, respectively. Chronopotentiometry experiments in acidic conditions for HER were done by loading a total of 20 μl catalyst ink on the GCE using two coats of 10 μl with a 2-minute interval, followed by overnight air-drying. Carbon electrode was used as counter electrode in a three-electrode setup. Voltage was collected for 10 hours, while applying a constant current of -1.9 mA ($\sim -10 \text{ mA/cm}^2$). Chronopotentiometry experiments in alkaline conditions were done on two-electrode cells using nickel foam, with applied currents of 2 mA and -10 mA, for OER (0.1 M KOH) and HER (1 M KOH), respectively. For OER, 2 mA was chosen due to the low current observed in the polarization curves. Each electrode consisted of 1 cm^2 nickel foam, on which 100 μl of the catalyst ink had been dropcasted with 20 μl increments, followed by overnight air-drying. The two electrodes, which had been separated by two layers of glass fiber filter paper, were attached to gold wires, which were then connected to the potentiostat. Prior to conducting the chronopotentiometry experiment, the two electrodes were soaked in the electrolyte for at least 12 hours. The potential versus Ag/AgCl electrode ($E_{\text{Ag/AgCl}}$) was converted to be expressed against RHE using the equation $E_{\text{RHE}} = E_{\text{Ag/AgCl}} + 0.059 \text{ pH} + E^{\circ}_{\text{Ag/AgCl}}$, where $E^{\circ}_{\text{Ag/AgCl}} = 0.21 \text{ V}$ for 3M KCl⁸⁴ and 0.197 V for 4 M KCl.^{85, 86}

2.2 RESULTS AND DISCUSSION

2.2.1 CRYSTAL STRUCTURE

Rietveld refined profiles for $\text{Sr}_2\text{LaMn}_2\text{O}_7$ and $\text{Ca}_2\text{LaMn}_2\text{O}_7$ are shown in **Figure 2.1** and their refined structural parameters are reported in **Table 2.1** and **2.2**.

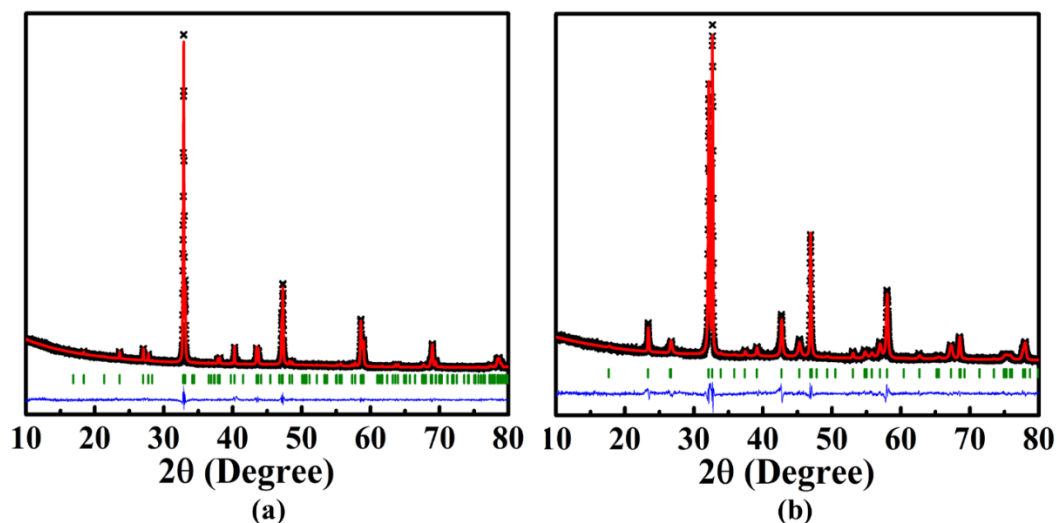


Figure 2.1: Rietveld refinement profiles for powder X-ray diffraction data for (a) $\text{Ca}_2\text{LaMn}_2\text{O}_7$ and (b) $\text{Sr}_2\text{LaMn}_2\text{O}_7$. The experimental data are represented by black crosses. The red line shows the fit. The vertical green tick marks and the lower blue line correspond to the Bragg peak positions and difference plot, respectively.

Table 2.1: Refined structural parameters of $\text{Ca}_2\text{LaMn}_2\text{O}_7$ from powder X-ray diffraction data. Space group: $Cmcm$, $a = 19.2814(4) \text{ \AA}$, $b = 5.4609(1) \text{ \AA}$, $c = 5.4113(1) \text{ \AA}$, $R_p = 0.0261$, $wR_p = 0.0341$

Atom	x	y	z	Occupancy	$U_{\text{iso}} (\text{Å}^2)$	Multiplicity
Ca1	0	0.248(2)	0.25	0.37(1)	0.028(3)	4
La1	0	0.248(2)	0.25	0.63(1)	0.028(3)	4
Ca2	0.1886(2)	0.242(2)	0.25	0.782(7)	0.052(3)	8
La2	0.1886(2)	0.242(2)	0.25	0.218(7)	0.052(3)	8
Mn	0.3995(3)	0.247(3)	0.25	1	0.017(3)	8

O1	0	0.683(8)	0.25	1	0.037(4)	4
O2	0.300(1)	0.290(5)	0.25	1	0.037(4)	8
O3	0.096(1)	0	0	1	0.037(4)	8
O4	0.393(1)	0	0	1	0.037(4)	8

Table 2.2: Refined structural parameters of Sr₂LaMn₂O₇ from powder X-ray diffraction data. Space group: *I4/mmm*, a = b = 3.8670(1) Å, c = 19.9814(10) Å, Rp = 0.0415, wRp = 0.0549

Atom	x	y	z	Occupancy	U _{iso} (Å ²)	Multiplicity
Sr1	0	0	0.5	0.60(3)	0.037(2)	2
La1	0	0	0.5	0.40(3)	0.037(2)	2
Sr2	0	0	0.3153(1)	0.73(3)	0.041(2)	4
La2	0	0	0.3153(1)	0.27(3)	0.041(2)	4
Mn	0	0	0.1007(4)	1	0.021(2)	4
O1	0	0	0	1	0.098(4)	2
O2	0	0	0.199(1)	1	0.098(4)	4
O3	0	0.5	0.095(1)	1	0.098(4)	8

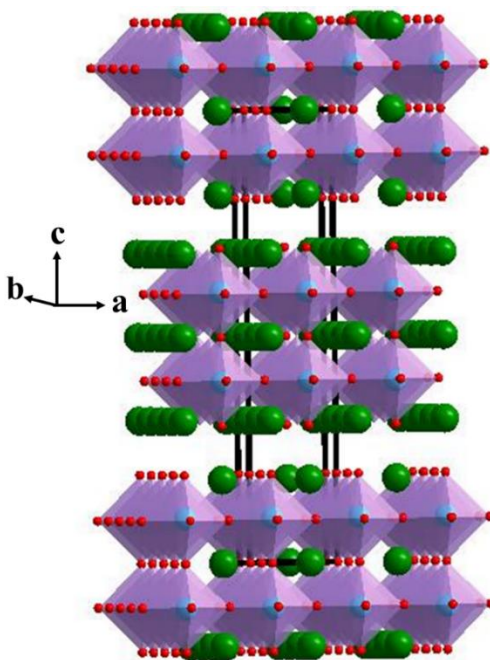


Figure 2.2: Crystal structure of $A_2LaMn_2O_7$ ($A=Ca/Sr$). Green spheres represent $Ca/Sr/La$ and red spheres are oxygen. The Mn atoms are shown as light blue spheres at the centers of MnO_6 octahedra.

As shown in **Figure 2.2**, the crystal structures of these Ruddlesden-Popper type oxides comprise bilayer stacks of MnO_6 octahedra, which are connected via corner-sharing. For each MnO_6 octahedron, one apical oxygen atom and four equatorial oxygens are involved in forming the bilayer stack. Each MnO_6 octahedron has one apical oxygen which is not shared with other octahedra. The $La/Ca/Sr$ atoms are located in spaces between and within the bi-layer stacks. The difference in the ionic radii of Ca^{2+} (1.18 Å) and Sr^{2+} (1.31 Å for $CN = 9$)⁸⁷ results in a change in structural symmetry of these isoelectronic materials. $Ca_2LaMn_2O_7$ ⁸⁸ crystallizes in the orthorhombic $Cmcm$ space group, while $Sr_2LaMn_2O_7$ ⁸⁹ has a tetragonal $I4/mmm$ space group, consistent with previous reports.^{88,89} The tilting and fine rotations of MnO_6 octahedra in $Ca_2LaMn_2O_7$, caused by the smaller ionic radius of Ca^{2+} , result in anisotropic Mn-O bond distances with four types of oxygens as shown in **Table 2.3:** Mn-O bond distances and Mn-O-Mn angles of $Sr_2LaMn_2O_7$ and $Ca_2LaMn_2O_7$

Sr₂LaMn₂O₇	
Mn–O1	2.012(8)
Mn–O2	1.965(23)
Mn–O3 × 4	1.9366(13)
Average Mn–O	1.9539(15)
Mn–O1–Mn	180.0(0)
Mn–O3–Mn	173.5(13)
Average Mn–O–Mn	176.75(9)
Ca₂LaMn₂O₇	
Mn–O1	1.970(11)
Mn–O2	1.924(23)
Mn–O3 × 2	1.936(12)
Mn–O4 × 2	1.915(12)
Average Mn–O	1.9326(14)
Mn–O1–Mn	159.4(25)
Mn–O3–Mn	174.4(16)
Mn–O4–Mn	172.4(15)
Average Mn–O–Mn	168.73(19)

The average Mn-O bond length for $\text{Ca}_2\text{LaMn}_2\text{O}_7$ is shorter than that of $\text{Sr}_2\text{LaMn}_2\text{O}_7$ (**Table 2.3**), consistent with the effect of the ionic radius in expanding the lattice of the latter material. The normalized unit cell volume for $\text{Ca}_2\text{LaMn}_2\text{O}_7$, 284.89 \AA^3 (normalized by dividing the tetragonal unit cell volume, 569.78 \AA^3 , by 2), is smaller than that of $\text{Sr}_2\text{LaMn}_2\text{O}_7$, 298.79 \AA^3 . The microstructures of the two materials were evaluated using scanning electron microscopy, as shown in **Figure 2.3**. As seen here, $\text{Sr}_2\text{LaMn}_2\text{O}_7$ has smaller grains compared to $\text{Ca}_2\text{LaMn}_2\text{O}_7$. The oxygen contents were confirmed using iodometric titrations, indicating 7 oxygens per unit formula unit for both materials.

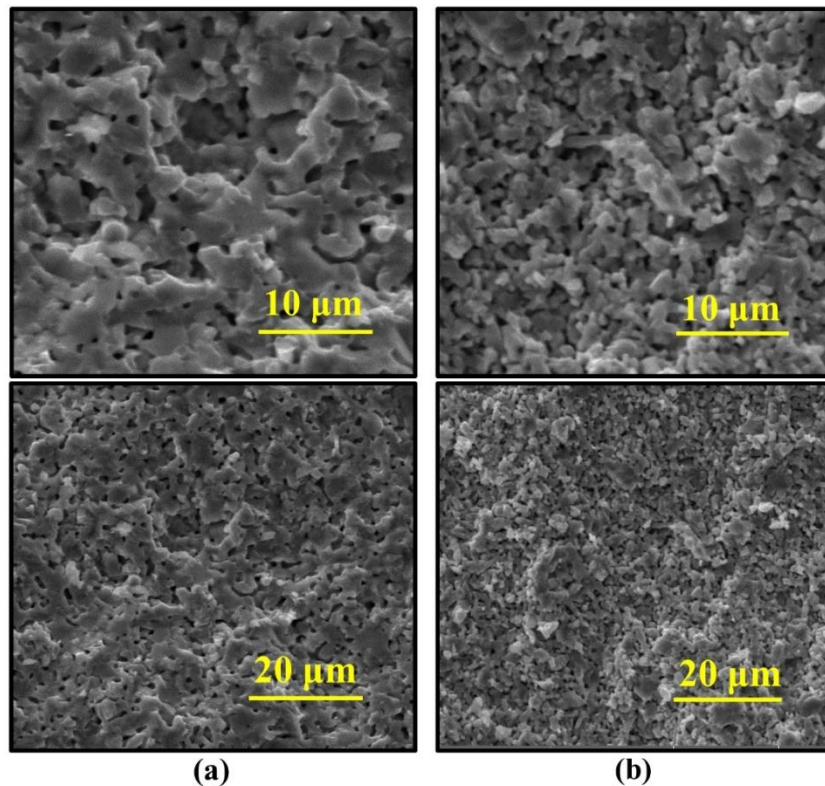


Figure 2.3: Scanning electron microscopy images of (a) $\text{Ca}_2\text{LaMn}_2\text{O}_7$ and (b) $\text{Sr}_2\text{LaMn}_2\text{O}_7$.

2.2.2 ELECTRICAL CONDUCTIVITY

The electrical properties of these materials were investigated in the temperature range 25-800 °C. The following equation was used to calculate conductivities using the measured resistance (R) values at a given constant voltage.⁹⁰

$$\sigma = L/RA \quad (1)$$

In the above equation, σ is the conductivity, L is the thickness of the cylindrical pellet, and A is the cross-sectional area calculated using $A = \pi r^2$, where r is the radius of the pellet. The electrical conductivity variation as a function of temperature is illustrated in **Figure 2.4a**. The conductivity of both materials increases as a function of temperature up to 400 °C for $\text{Sr}_2\text{LaMn}_2\text{O}_7$ and 500 °C for $\text{Ca}_2\text{LaMn}_2\text{O}_7$, which is a typical behavior of semiconductors. However, beyond those temperatures, a transition occurs where the electrical conductivity decreases as a function of temperature, which is a characteristic metallic behavior. $\text{Sr}_2\text{LaMn}_2\text{O}_7$ shows higher conductivity than $\text{Ca}_2\text{LaMn}_2\text{O}_7$ through the entire temperature range, indicating the impact of structural properties on conductivity. Generally, the heterovalency of the B-site cation is important for electrical conduction in oxides. In Ruddlesden-Popper oxides, the B-site cations are usually transition metals. The overlap of the 3d orbitals of transition metals with the 2p orbitals of oxygen facilitates the conduction via B-O-B pathways using electrons or holes. Greater metal overlap between these orbitals can be achieved by shorter B-O bonds and larger B-O-B angles to enhance the electrical conductivity.⁹¹ In the case of materials studied in this work, the type of transition metal is the same in both compounds. Therefore, the effects of structural distortions and bond angles becomes prominent. The average Mn-O-Mn bond angles in $\text{Sr}_2\text{LaMn}_2\text{O}_7$ is closer

to 180° degrees (**Table 2.3**), hence providing an improved orbital overlap and enhanced conduction through the Mn-O-Mn pathway. This is a consequence of the more symmetrical structure of Sr₂LaMn₂O₇ (tetragonal) as opposed to that of Ca₂LaMn₂O₇ (orthorhombic), which contains more distortions due to the smaller ionic radius of calcium.

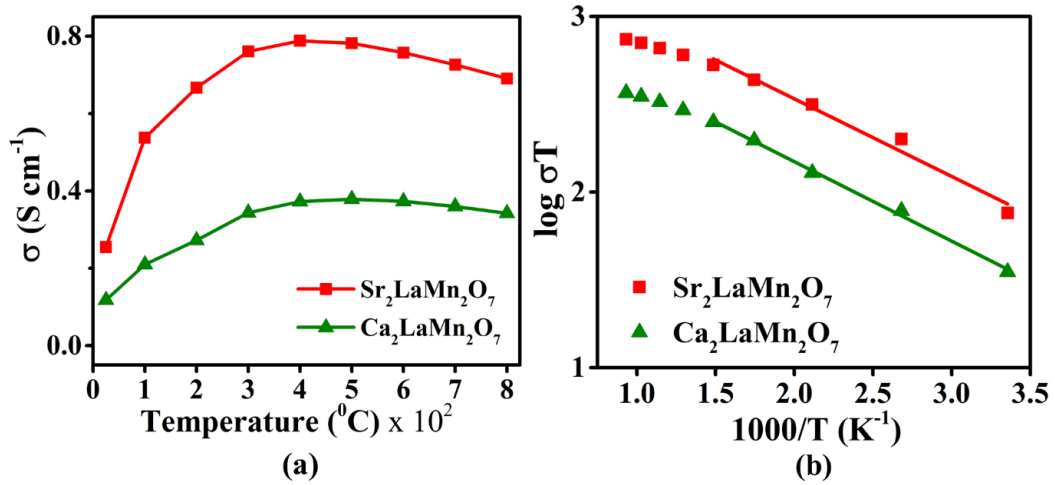


Figure 2.4: (a) Electrical conductivity variation as a function of temperature. (b) Arrhenius plots for determination of the activation energies (E_a) for the temperature-activated increase in conductivity, giving $E_a = 0.0877$ (25-500 °C) for Sr₂LaMn₂O₇ and $E_a = 0.0898$ (25-400 °C) for Ca₂LaMn₂O₇.

The activation energy associated with the thermally activated increase in conductivity³³ can be calculated using the Arrhenius equation shown below, where σ , A , T , E_a , and K_B represent the conductivity, pre-exponential factor, temperature, activation energy, and Boltzmann constant, respectively.

$$\sigma T = A e^{-\frac{E_a}{2.303 K_B T}} \quad (2)$$

The Arrhenius plots for the two materials are shown in **Figure 2.4b**. The activation energies calculated using the Arrhenius plots ($\log \sigma T$ vs $1000/T$) show similar activation energies for both compounds in the range 25 – 400 °C. This indicates that the rate of increase in electrical conductivity as a function of temperature is similar in the two materials.

2.2.3 MAGNETIC PROPERTIES

Structural changes also have a notable impact on magnetic properties. Magnetic susceptibility (χ) measurements were carried out in the temperature range 2 K – 400 K. As shown in **Figure 2.5a**, there is a sharp increase in susceptibility for $\text{Ca}_2\text{LaMn}_2\text{O}_7$, as the temperature is lowered below ~280 K, indicative of ferromagnetic interactions, similar to the behavior observed in a previous study.⁸⁸ The isothermal magnetization versus field data at 300 K shows a linear increase as a function of field, a typical paramagnetic behavior. However, the isothermal magnetization at 5 K shows a sharp increase at low field, but saturation is not reached up to 9 T. A small hysteresis is also present in the isothermal magnetization data at 5 K, consistent with a weak ferromagnetic behavior.

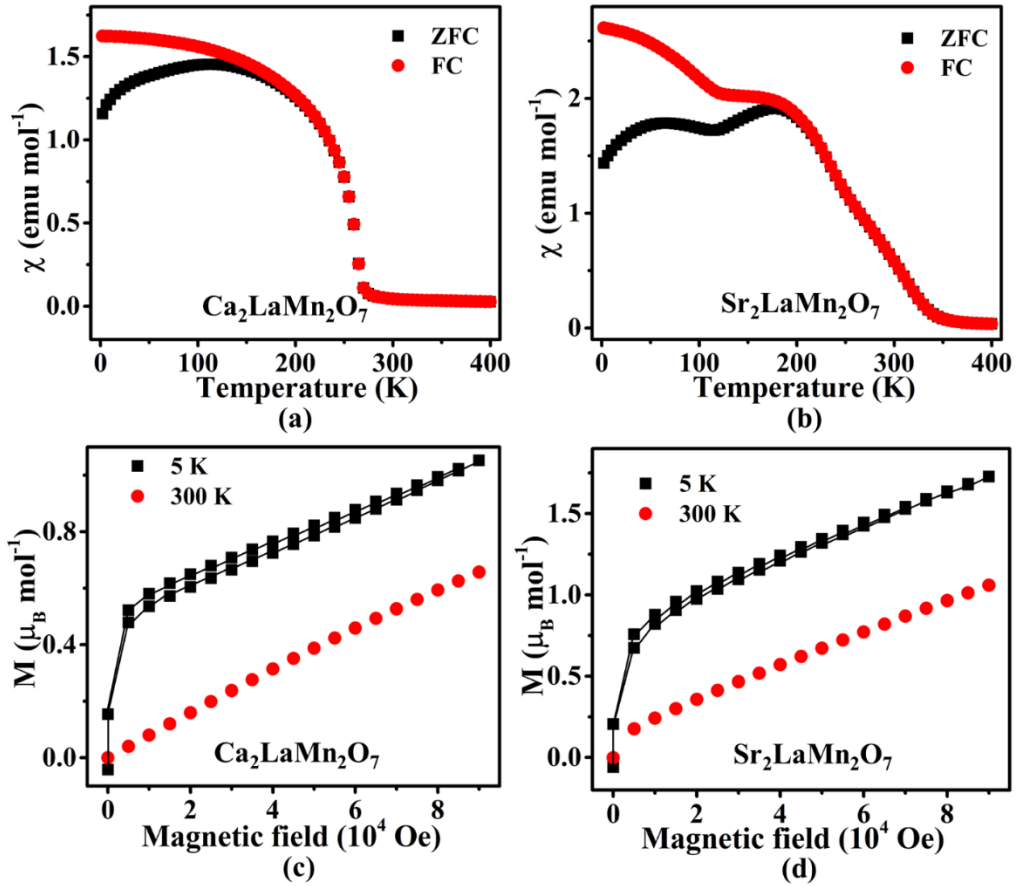


Figure 2.5: (a) and (b) show zero-field-cooled (ZFC) and field-cooled (FC) magnetic susceptibility data. (c) and (d) show the isothermal magnetization data as a function of magnetic field. The lines are guide to the eye.

The magnetic susceptibility and isothermal field sweep data for $\text{Sr}_2\text{LaMn}_2\text{O}_7$ show a different behavior. As demonstrated in **Figure 2.5b**, the data for $\text{Sr}_2\text{LaMn}_2\text{O}_7$ shows a rise in the susceptibility value below 350 K. Further decrease in temperature leads to a transition below ~ 220 K. The isothermal magnetization versus field data at 5 K show an initial sharp increase in magnetization, followed by a more modest rise as a function of the field, without reaching saturation in the range of 0 – 9 T. Taken together, the variable temperature susceptibility and isothermal magnetization data indicate competing ferro- and antiferromagnetic behaviors for $\text{Sr}_2\text{LaMn}_2\text{O}_7$, consistent with a previous report.⁹² The isothermal magnetization at 300 K shows a sharp increase up to ~ 0.5 T, followed by a

linear rise with a smaller slope at higher fields. This confirms that ferromagnetic interactions are present at room temperature as well.

2.2.4 ELECTROCATALYTIC PROPERTIES FOR OER AND HER

An important impact of the change in the structure is observed in the electrocatalytic properties toward both half reactions of water-splitting, i.e., oxygen evolution reaction (OER) and hydrogen evolution reaction (HER). The electrocatalytic activities for OER in 0.1 M KOH are shown in **Figure 2.6**. Measurements in other conditions, such as 1M KOH and 0.1 M HClO₄, led to rapid deterioration of the current response. While both materials show low activity and a low current, the effect of structural change is clear. Sr₂LaMn₂O₇, which has a higher symmetry, shows better performance, evident from lower onset potential, where the electrocatalytic reaction begins and the polarization curve deviates from a horizontal line to show an increase in current response. In addition, the current generated using Sr₂LaMn₂O₇ at the same potential is greater than that of Ca₂LaMn₂O₇. Furthermore, Sr₂LaMn₂O₇ shows better reaction kinetics, evaluated using the Tafel equation $\eta = a + b \log j$, where η is the overpotential and j is the current density.^{33,53} The slope of the plot of η versus $\log j$, i.e., Tafel slope (**Figure 2.6b**), is indicative of the reaction kinetics and is affected by electron and mass transport. In general, lower Tafel slopes show better kinetics of the OER reaction. As shown in **Figure 2.6b**, the Tafel slope for Sr₂LaMn₂O₇ is smaller than that of Ca₂LaMn₂O₇, consistent with better kinetics and higher electrocatalytic activity of the former material.

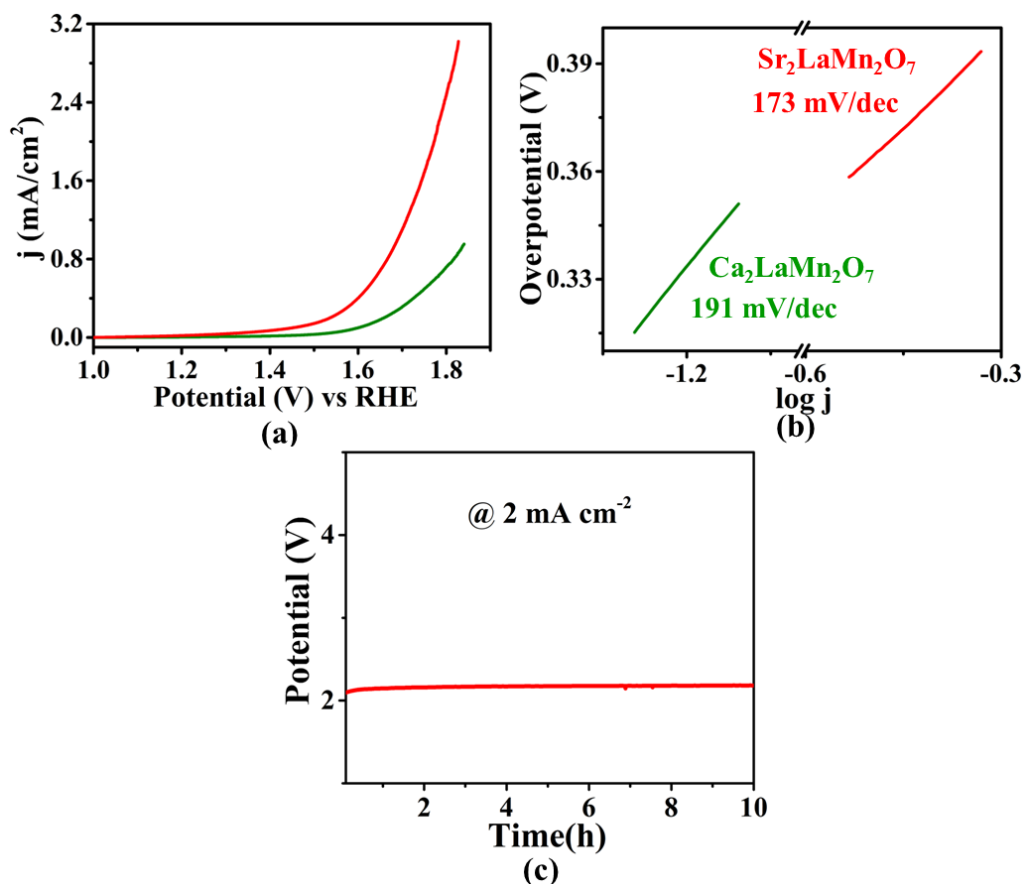


Figure 2.6: OER activity in 0.1 M KOH for Sr₂LaMn₂O₇ (red) and Ca₂LaMn₂O₇ (green): (a) Polarization curves, (b) Tafel plots and (c) Chronopotentiometry response of Sr₂LaMn₂O₇.

The electrocatalytic properties for HER show a greater current response, especially in acidic condition, 0.5 M H₂SO₄. **Figure 2.7a** shows the polarization curves of the two materials, where Sr₂LaMn₂O₇ gives a lower onset potential than Ca₂LaMn₂O₇. In addition, the overpotential at 10 mA/cm² (η_{10}) is commonly used as a reference for comparing different electrocatalysts. Again, Sr₂LaMn₂O₇ ($\eta_{10} = 0.589$ V) shows a lower overpotential than Ca₂LaMn₂O₇ ($\eta_{10} = 0.595$ V). Although the performance of these materials is not as high as Pt/C^{93, 94} (shown in black in **Figure 2.7a**) or some other oxide catalysts such as

CaSrFe_{0.75}Co_{0.75}Mn_{0.5}O_{6-δ},⁹⁵ they show a better performance than some reported HER electrocatalysts such as WO₃ ($\eta_{10} = 0.637$ V)⁹⁶ and TiO_{2-x} ($\eta_{10} = 0.630$ V).⁹⁷

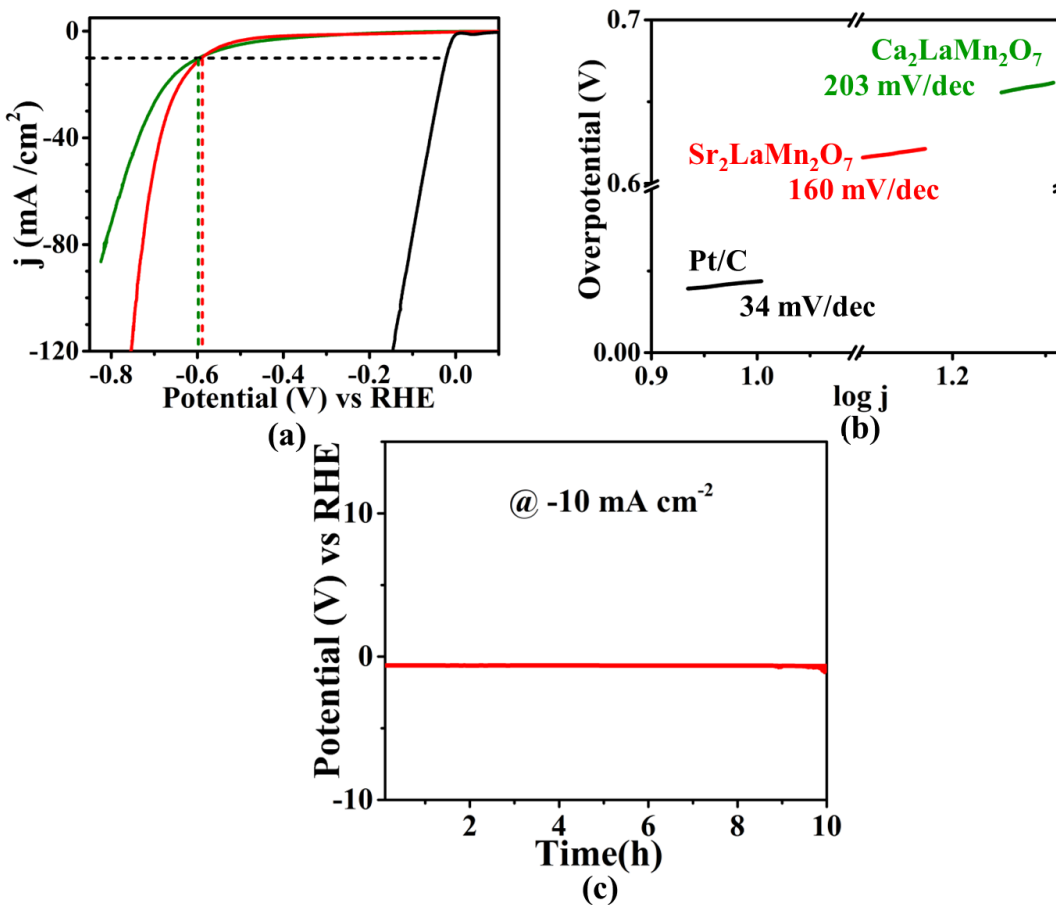


Figure 2.7: (a) HER polarization curves in 0.5 M H₂SO₄ for Ca₂LaMn₂O₇ (green) and Sr₂LaMn₂O₇ (red). (b) Tafel plots and Tafel slopes. (c) Chronopotentiometry data for Sr₂LaMn₂O₇.

Figure 2.7b shows the Tafel plots for HER, where Sr₂LaMn₂O₇ has a smaller Tafel slope than Ca₂LaMn₂O₇, indicating faster reaction kinetics for the former material. This is in line with the higher HER activity of Sr₂LaMn₂O₇, which also shows a sustained response for at least 10 hours, as demonstrated by chronopotentiometry data in **Figure 2.7c**.

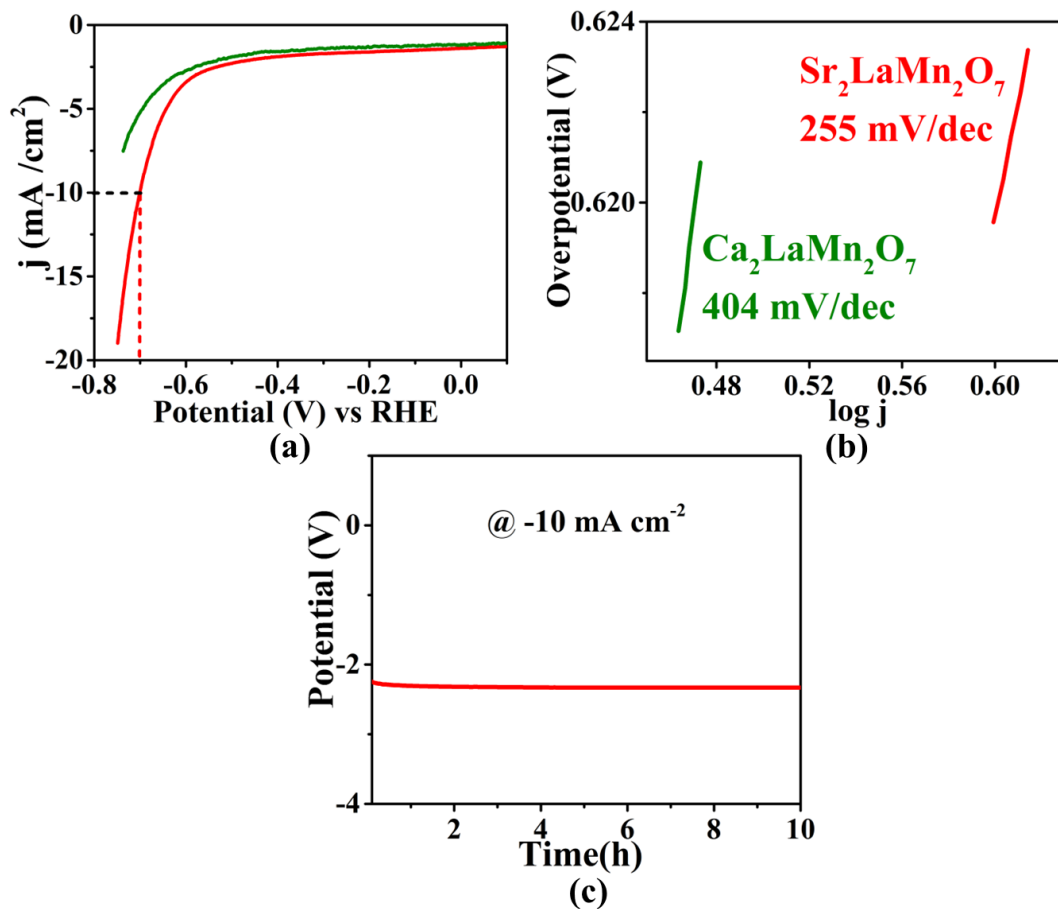


Figure 2.8: (a) HER polarization curves in 1 M KOH for $\text{Ca}_2\text{LaMn}_2\text{O}_7$ (green) and $\text{Sr}_2\text{LaMn}_2\text{O}_7$ (red). (b) Tafel plots and Tafel slopes. (c) Chronopotentiometry data for $\text{Sr}_2\text{LaMn}_2\text{O}_7$.

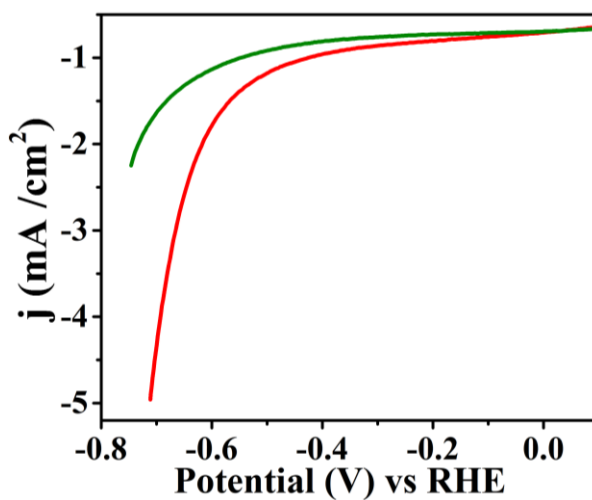


Figure 2.9: HER polarization curves in 0.1 M KOH for $\text{Ca}_2\text{LaMn}_2\text{O}_7$ (green) and $\text{Sr}_2\text{LaMn}_2\text{O}_7$ (red).

HER experiments were also done in alkaline conditions, as shown in **Figure 2.7** and **2.8**, indicating higher overpotentials. However, the catalysts have better stability in alkaline conditions. Even though the catalysts are able to catalyze the HER in acidic condition, we have found the catalytic material is partially decomposed under those conditions. However, at least some portion of the catalyst remains intact to give a stable current response for 10 hours in chronopotentiometry experiments. As demonstrated by X-ray diffraction experiments before and after 500 cycles, the main peaks corresponding to our catalyst are still present after 500 cycles, but there is evidence of gradual decomposition of the material in acidic conditions, indicated by the appearance of new peaks (**Figure 2.10**). On the other hand, in alkaline conditions, X-ray diffraction experiments before and after 500 cycles show that the material remains intact and retains its structural integrity, with no new peaks appearing in the diffraction data after 500 cycles (**Figure 2.11**).

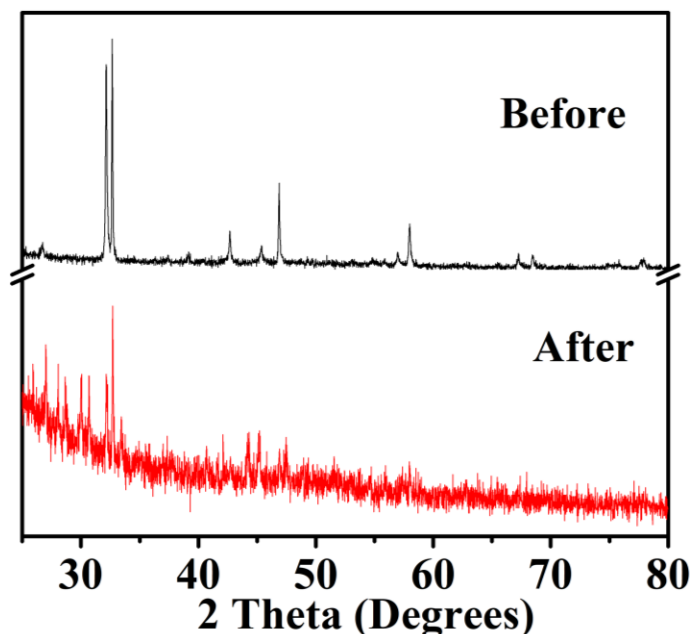


Figure 2.10: X-ray diffraction data of Sr₂LaMn₂O₇ before and after 500 cycles of HER in the 0.5 M H₂SO₄.

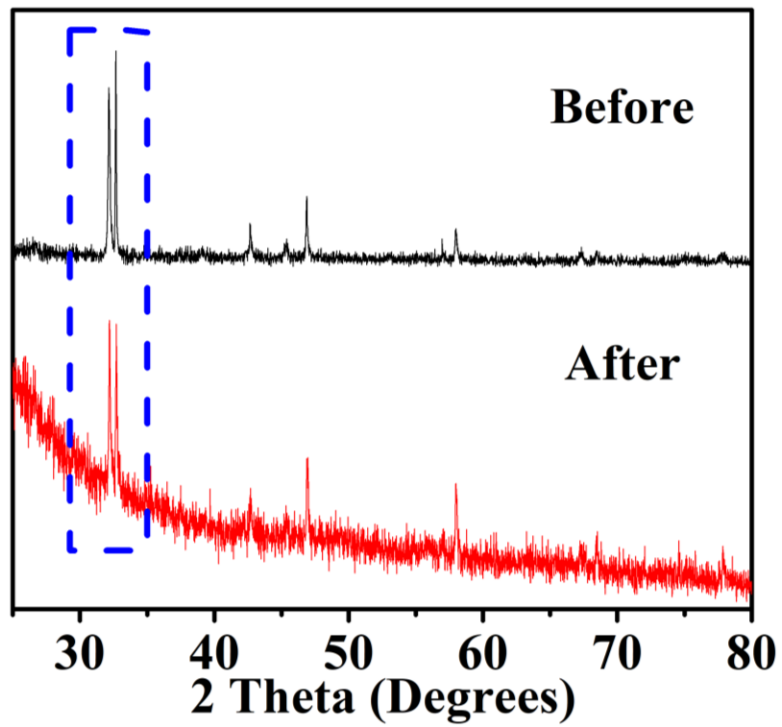


Figure 2.11: X-ray diffraction data of $\text{Sr}_2\text{LaMn}_2\text{O}_7$, before and after 500 cycles of HER in 1 M KOH.

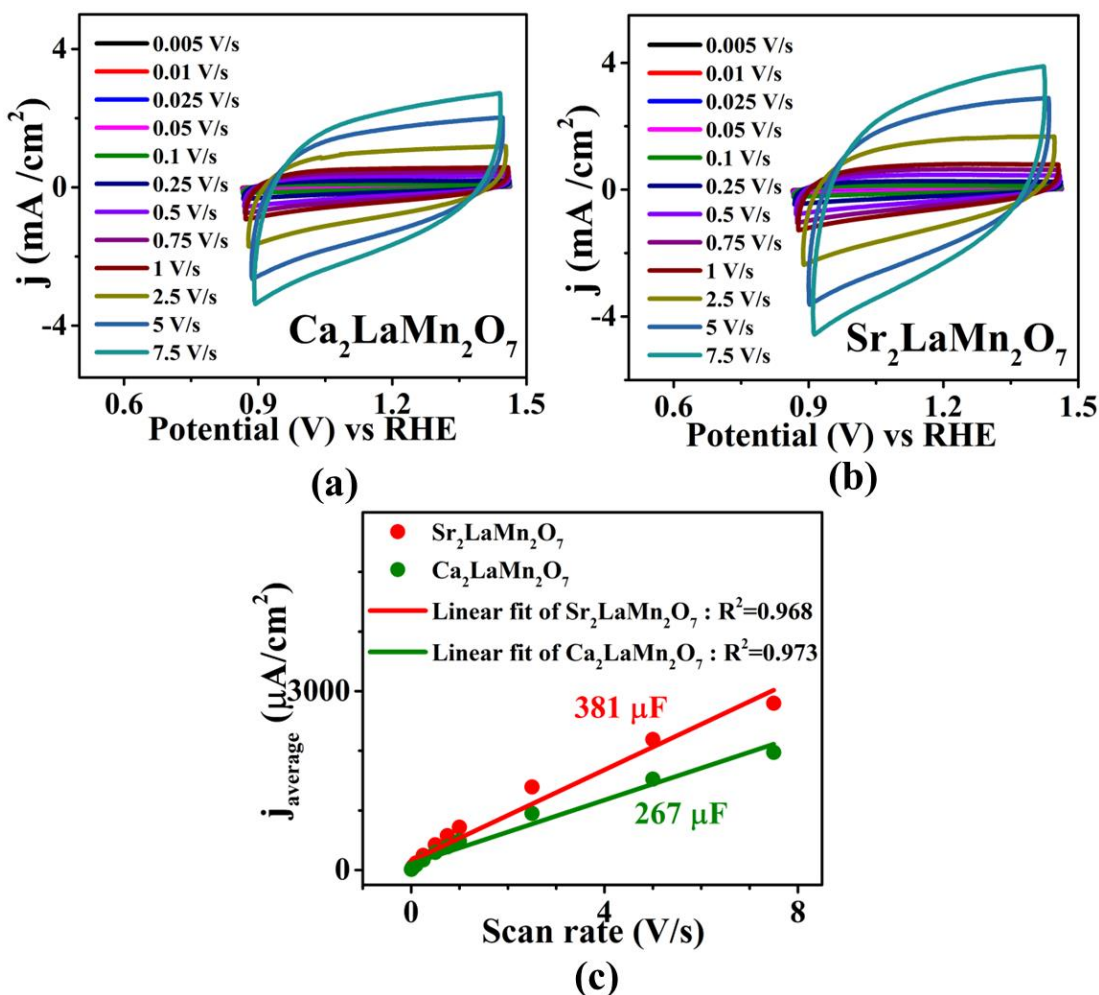


Figure 2.12: (a) and (b) show cyclic voltammetry (CV) data in non-Faradaic region in 0.1 M KOH. (c) shows the plot of j_{average} obtained from the middle potential of the above CVs as a function of scan rate. The slopes give the double layer capacitance values.

The double layer capacitance values, C_{dl} ,⁹⁸ were also obtained for both materials using cyclic voltammetry in the non-Faradaic region (**Figure 2.12a** and **b**), where the current stems from electrical double layer charge and discharge. The average of j_{anodic} and j_{cathodic} at the middle potential of the cyclic voltammetry data (j_{average}) is plotted against the scan rate ν based on the equation $C_{\text{dl}} = j_{\text{average}}/\nu$. Therefore, the C_{dl} value is obtained from the slope of the j_{average} vs ν plot.^{95, 99} As shown in **Figure 2.12**, the C_{dl} value for $\text{Sr}_2\text{LaMn}_2\text{O}_7$ is

greater than that of $\text{Ca}_2\text{LaMn}_2\text{O}_7$. The importance of C_{dl} is that it is proportional to the electrochemically active surface area.^{54, 100, 101}

The enhanced electrocatalytic activity of $\text{Sr}_2\text{LaMn}_2\text{O}_7$ may be understood in the context of its structural features. The HER process involves the adsorption of hydrogen atoms on the catalyst surface as intermediate species before forming hydrogen molecules.¹⁰² Various descriptors have been proposed to explain the HER activities of different catalysts. Among them, some are related to structural features, where the HER performance is correlated with the bond length between the transition metal and the non-metal anion.^{10, 103} Some researchers have proposed that longer distances between the metal and non-metal sites allow for greater electron localization on the non-metal site, favoring the adsorption of hydrogen and final transformation into hydrogen molecules.¹⁰³ As shown in **Table 2.3**, the average Mn-O bond length for $\text{Sr}_2\text{LaMn}_2\text{O}_7$ is greater than that of $\text{Ca}_2\text{LaMn}_2\text{O}_7$, which is consistent with the above descriptor, relating the HER activity to bond length. In addition, the average Mn-O-Mn bond angle for $\text{Sr}_2\text{LaMn}_2\text{O}_7$ is larger, leading to a better alignment of metal d and oxygen p orbitals and higher electrical conductivity. Given that HER is an electron transfer process, the enhanced electrical charge transport of $\text{Sr}_2\text{LaMn}_2\text{O}_7$ can also contribute to its greater electrocatalytic performance.

2.3 CONCLUSIONS

The structural symmetry has an important impact on electrical charge transport, magnetism and electrocatalytic activity, as demonstrated for isoelectronic oxides $\text{Ca}_2\text{LaMn}_2\text{O}_7$ and $\text{Sr}_2\text{LaMn}_2\text{O}_7$. The higher symmetry of the latter leads to enhanced electrical conductivity

and greater electrocatalytic performance for both half-reactions of water-splitting, i.e., HER and OER. $\text{Sr}_2\text{LaMn}_2\text{O}_7$ shows lower onset and overpotentials for these electrocatalytic processes, as well as better reaction kinetics. The improved activity of this material may be related to longer bond distances, which are proposed to correlate with electrocatalytic performance. In addition, greater bond angles lead to enhanced electrical conductivity, which in turn can have a positive impact on electrocatalytic properties, which involve the transfer of electrons.

CHAPTER 3

VARIATION OF ELECTROCATALYTIC ACTIVITY OF ISOSTRUCTURAL OXIDES $\text{Sr}_2\text{LaFeMnO}_7$ AND $\text{Sr}_2\text{LaCoMnO}_7$ FOR HYDROGEN AND OXYGEN- EVOLUTION ²

3.1 EXPERIMENTAL

3.1.1 SYNTHESIS

$\text{Sr}_2\text{LaCoMnO}_7$ and $\text{Sr}_2\text{LaFeMnO}_7$ were prepared by solid-state synthesis method. Stoichiometric amounts of SrCO_3 , La_2O_3 , MnO_2 , Fe_2O_3 or CoO were mixed thoroughly using agate mortar and pestle, then pressed into pellets and heated at 1300 °C for 24 hours in air. The samples were then ground, re-pelletized and heated at 1300 °C in air for 72 hours with two intermittent grindings and pelletizing. The heating and cooling rates of the furnace for all samples were 100 °C/hour.

3.1.2 CHARACTERIZATION

The synthesized materials were characterized by powder X-ray diffraction data using a high-resolution Cu $K\alpha_1$ X-ray diffractometer ($\lambda = 1.54056 \text{ \AA}$). Rietveld refinements were

² The work described in this chapter was published in Dalton Trans. **2021**, 50 (40), 14196-14206.

carried out using GSAS software⁷⁶ and the EXPGUI interface.⁷⁷ The electrical conductivity measurements in air were done using two-probe DC technique on small cylindrical pellets by applying the potential of 0.01 V and collecting the output current. Magnetic susceptibility data were obtained in the temperature range of 2 K to 400 K with an applied magnetic field of 1000 Oe on a vibrating sample magnetometer. Isothermal field-run measurements were also done in magnetic fields of 0 – 9 T. To examine the oxygen stoichiometry, iodometric titrations⁴² were performed by dissolving 50 mg of the sample and excess KI (2 g) in 100 ml of 1 M HCl, which were left overnight to ensure the completion of the reaction. All steps were done under argon atmosphere. Then 5 ml of the solution was pipetted out and the iodine generated during the process was titrated against 0.025 M Na₂S₂O₃. A volume of 0.6 ml (12 drops) of starch solution was used as an indicator near the endpoint of the titration.

3.1.3 ELECTROCATALYTIC MEASUREMENTS FOR OER AND HER

The catalyst ink was prepared by mixing 35 mg of the Ruddlesden-Popper sample, 7 mg of carbon black powder (Fuel Cell Store), 40 μ L Nafion® D-521 solution (Alfa Aesar, 5% w/w in water and 1-propanol) and 7 ml of THF (Alfa Aesar, 99%). After mixing, the solution mixture was sonicated for 30 minutes. This was followed by pipetting 20 μ l of the catalyst ink and drop-casting it on the surface of a glassy carbon electrode (GCE), which served as working electrode. The drop-casting was done by placing two coats of 10 μ l solution on GCE with a 2-minute interval. The GCE was then left overnight to air-dry before running the OER/HER measurements. Catalyst mass loading on GCE disk (diameter 5mm) was 0.1 mg. Prior to drop-casting, the GCE was furnished with aluminum oxide

polishing solution (Allied Hightech Products Inc.) on a polishing cloth and sonicated for 2-3 minutes in ethanol (Decon Labs, Inc.). It was then washed with deionized water before use. The electrochemical OER/HER experiments were carried out in a standard three-electrode cell using an electrode rotator (Pine Research Instrumentation, Inc.) at 1600 rpm. A commercial Ag/AgCl in 1 M KCl (CH instruments, Inc., TX, USA) and a commercial Ag/AgCl in 4 M KCl (Pine Research Instrumentation, Inc.) were utilized as reference electrodes for OER and HER experiments respectively. A platinum electrode was used as the counter electrode in basic condition and a carbon electrode in acidic condition. Chronopotentiometry experiments under HER conditions were done using this three-electrode setup and a constant current of -1.9 mA. Also, chronopotentiometry experiments under OER conditions, with an applied current of 10 mA, were done using a two-electrode cell. Each electrode consisted of 1 cm² nickel foam, on which 100 μ l of the catalyst ink had been dropcasted with 20 μ l increments, followed by overnight air-drying. Gold wires were attached to the two electrodes, which had been separated by two layers of glass fiber filter paper. The two electrodes were soaked in 0.1M KOH for least 12 hours before performing the chronopotentiometry experiment. The potential versus silver/silver chloride ($E_{\text{Ag}/\text{AgCl}}$) was converted to be expressed against RHE using the equation $E_{\text{RHE}} = E_{\text{Ag}/\text{AgCl}} + 0.059 \text{ pH} + E^0_{\text{Ag}/\text{AgCl}}$, where $E^0_{\text{Ag}/\text{AgCl}} = 0.21 \text{ V}$ for 3M KCl⁸⁴ and 0.197 V for 4 M KCl.^{85, 86}

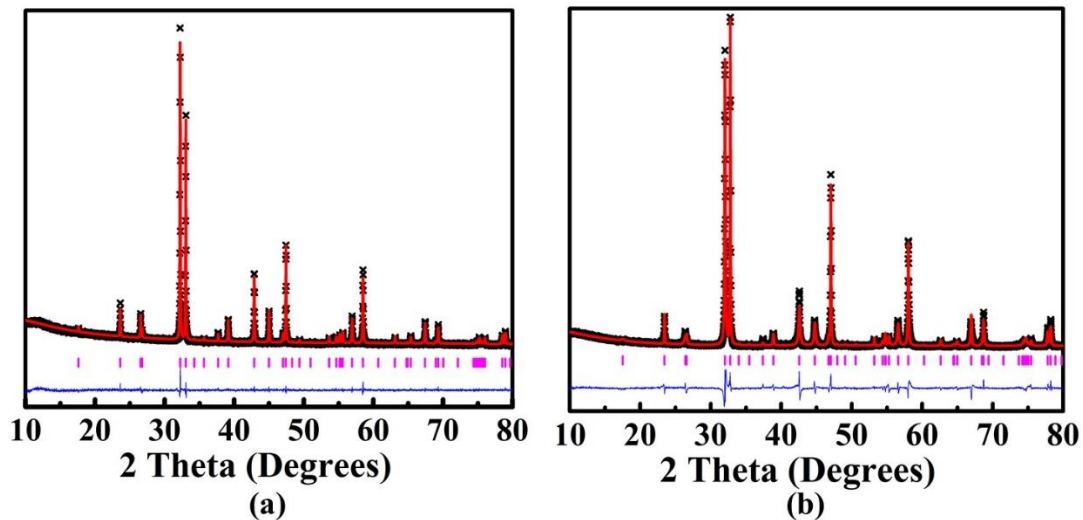


Figure 3.1: Rietveld refinement profiles for powder X-ray diffraction data for (a) $\text{Sr}_2\text{LaCoMnO}_7$ and (b) $\text{Sr}_2\text{LaFeMnO}_7$. The experimental data are represented by black crosses. The red line shows the fit. The vertical magenta tick marks, and the lower blue line correspond to the Bragg peak positions and difference plot, respectively.

3.2 RESULTS AND DISCUSSION

3.2.1 CRYSTAL STRUCTURE

The crystal structures of $\text{Sr}_2\text{LaCoMnO}_7$ and $\text{Sr}_2\text{LaFeMnO}_7$ were confirmed by Rietveld refinements using powder X-ray diffraction data. The Rietveld refinement profiles for the two compounds are shown in **Figure 3.1**. Both materials crystallize in tetragonal $I4/mmm$ space group, consistent with previous structural reports.^{104,105} The refined structural parameters are listed in **Tables 3.1 and 3.2**.

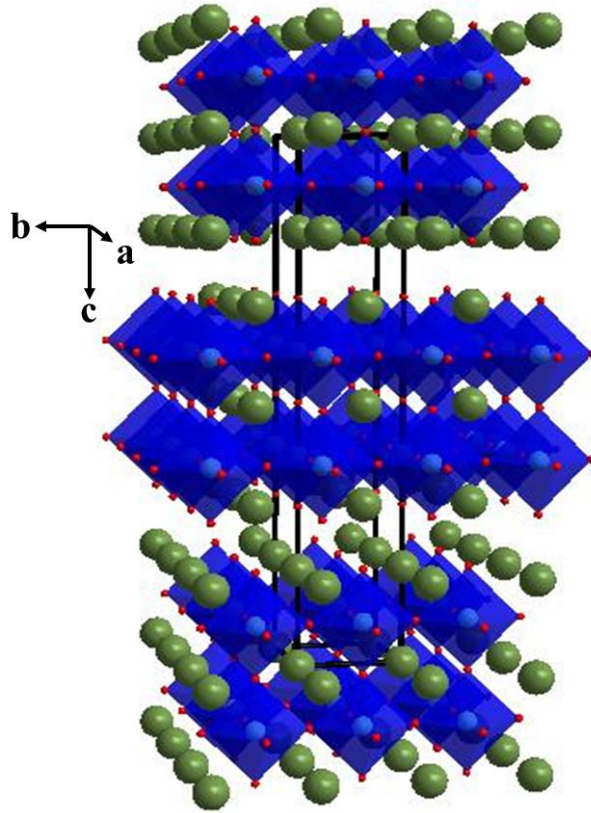


Figure 3.2: Crystal structure of $\text{Sr}_2\text{LaBMnO}_7$ ($B = \text{Fe}, \text{Co}$). Green spheres represent Sr/La, and red spheres show oxygens. The BO_6 octahedra are shown in dark blue.

The crystal structure of these Ruddlesden-Popper oxides, $\text{A}_{n+1}\text{B}_n\text{O}_{3n+1}$ ($n = 2$), consists of bilayer stacks of BO_6 octahedra. As shown in **Figure 3.2**, the BO_6 units ($B = \text{Mn}, \text{Fe}$ or Co) form a two-dimensional network by sharing the corner oxygens. Each octahedron shares one of its apical oxygens and all four of its equatorial oxygens with other octahedra.¹⁰⁶ The spaces between the BO_6 octahedra are occupied by the A-site cations.

Therefore, there are two crystallo

graphically distinct positions for A-site cations, one within and another between the octahedral stacks. Thus, the formula can be represented as $\text{AA}'_2\text{B}_2\text{O}_7$,¹⁰⁶ where A and A' indicate the metals located in intra and inter-stack spaces, respectively.

Table 3.1: Refined structural parameters of Sr₂LaCoMnO₇ from powder X-ray diffraction data.

Atom	x	y	z	Occupancy	U _{iso} (Å ²)	Multiplicity
Sr1	0	0	0.18233(9)	0.6667	0.034(1)	4
La1	0	0	0.18233(9)	0.3333	0.034(1)	4
Sr2	0	0	0	0.6667	0.010(1)	2
La2	0	0	0	0.3333	0.010(1)	2
Mn	0	0	0.4020(2)	0.5	0.024(1)	4
Co	0	0	0.4020(2)	0.5	0.024(1)	4
O1	0	0	0.5	1	0.036(9)	2
O2	0	0	0.3039(7)	1	0.040(6)	4
O3	0	0.5	0.0945(6)	1	0.028(3)	8

Space group: *I4/mmm*, $a = b = 3.83116(5)$ Å, $c = 20.1327(3)$ Å, $R_p = 0.0359$, $wR_p = 0.0446$

Table 3.2: Refined structural parameters of Sr₂LaFeMnO₇ from powder X-ray diffraction data.

Atom	x	y	z	Occupancy	U _{iso} (Å ²)	Multiplicity
Sr1	0	0	0.5	0.6667	0.027(2)	2
La1	0	0	0.5	0.3333	0.027(2)	2
Sr2	0	0	0.3166(1)	0.6667	0.047(2)	4
La2	0	0	0.3166(1)	0.3333	0.047(2)	4
Mn	0	0	0.1004(3)	0.5	0.016(1)	4
Fe	0	0	0.1004(3)	0.5	0.016(1)	4

O1	0	0	0	1	0.043(2)	2
O2	0	0	0.1899(8)	1	0.043(2)	4
O3	0	0.5	0.0928(9)	1	0.043(2)	8

Space group: $I4/mmm$, $a = b = 3.8617(1) \text{ \AA}$, $c = 20.2300(6) \text{ \AA}$, $R_p = 0.0360$, $wR_p = 0.0558$

While the structures of $\text{Sr}_2\text{LaFeMnO}_7$ and $\text{Sr}_2\text{LaCoMnO}_7$ are similar, the two compounds show slightly different unit volumes, i.e., $301.68(2) \text{ \AA}^3$ and $295.50(1) \text{ \AA}^3$, respectively. This is consistent with the difference in the ionic radii of Fe^{3+} and Co^{3+} , which are 0.645 \AA and 0.61 \AA , respectively.⁸⁷ To examine the oxygen contents of these materials, iodometric titrations were done, which indicated 7 oxygens per formula unit for both compounds. Scanning electron microscopy was used to evaluate the microstructure of the compounds. As shown in **Figure 3.3**, these data indicate larger grain size for $\text{Sr}_2\text{LaCoMnO}_7$ compared to $\text{Sr}_2\text{LaFeMnO}_7$.

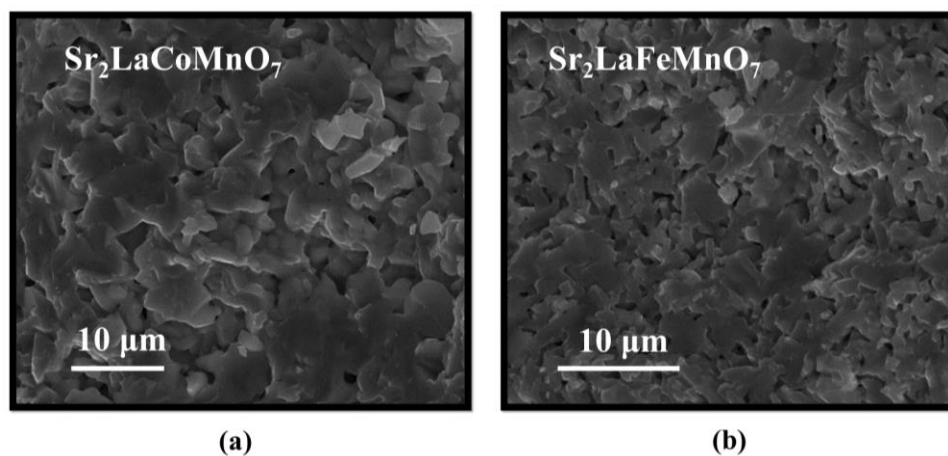


Figure 3.3: Scanning electron microscopy images for $\text{Sr}_2\text{LaCoMnO}_7$ compared to $\text{Sr}_2\text{LaFeMnO}_7$.

3.2.2 ELECTRICAL CONDUCTIVITY

The electrical properties of these materials were investigated in the temperature range 25 – 800 °C, indicating the effect of the change in the B-site cation. Electrical conductivity was obtained from the measured resistance (R) using the following equation:

$$\sigma = L/RA \quad (1)$$

Here, σ is the conductivity, L is the thickness of the measured pellet, and A is the cross-sectional area of the pellet. The variation of electrical conductivity as a function of temperature is illustrated in **Figure 3.4a**. As observed in this Figure, $\text{Sr}_2\text{LaCoMnO}_7$ shows significantly greater conductivity than $\text{Sr}_2\text{LaFeMnO}_7$ in the entire temperature range.

Both compounds show an increase in electrical conductivity as temperature increases beyond room temperature, but the conductivity of $\text{Sr}_2\text{LaCoMnO}_7$ plateaus and then decreases when the temperature is raised above 500 °C. The activation energy¹⁰⁷ can be found using the Arrhenius equation for thermally activated increase in conductivity:³³

91

$$\sigma T = A e^{-\frac{E_a}{k_B T}} \quad (2)$$

Here, σ , A, T, E_a , and k_B represent conductivity, pre-exponential factor, temperature, activation energy, and the Boltzmann constant, respectively. The Arrhenius plots for $\text{Sr}_2\text{LaFeMnO}_7$ and $\text{Sr}_2\text{LaCoMnO}_7$ are shown in **Figure 3.4b**. It is noted that the activation energy here represents the energy barrier for the temperature-dependent increase in conductivity.

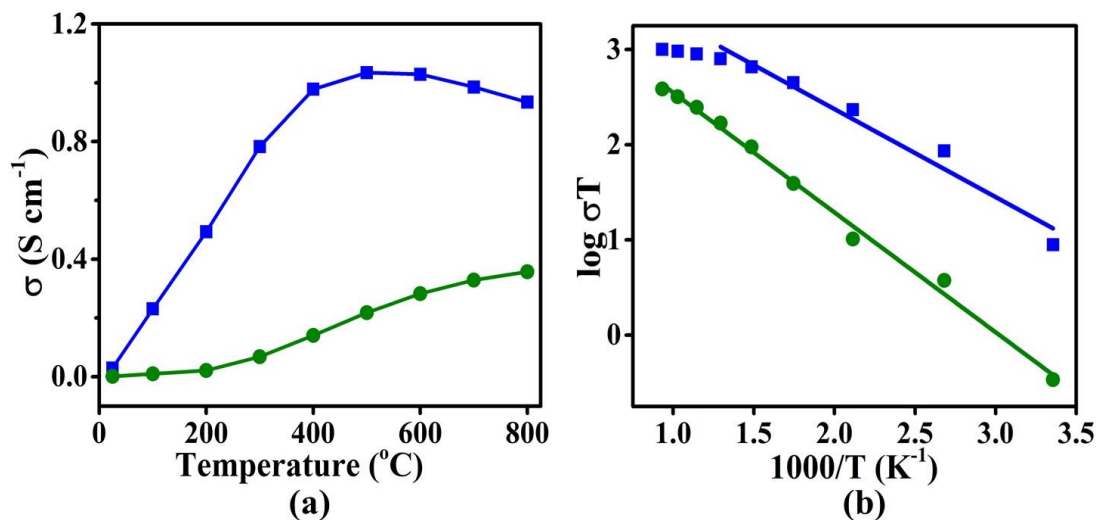


Figure 3.4: (a) Electrical conductivity variation as a function of temperature for $Sr_2LaFeMnO_7$ (green) and $Sr_2LaCoMnO_7$ (blue). (b) Arrhenius plots for determination of the activation energies (E_a) for the temperature-activated increase in conductivity, giving $E_a = 0.2499$ (25-800 $^{\circ}C$) for $Sr_2LaMnCoO_7$ and $E_a = 0.194$ (25-500 $^{\circ}C$) for $Sr_2LaMnCoO_7$.

The electrical conduction in oxide materials often occurs through the B–O–B pathways, where B is usually a transition metal with hetero-valency. The overlap of the 3d orbitals of the transition metal with the 2p orbitals of oxygen allows the electron conduction. This overlap can be enhanced by shorter B–O bonds and larger B–O–B angles, i.e., angles closer to 180° .⁹¹ While the average B–O bond distance is similar for both compounds, the average B–O–B bond angle for $Sr_2LaCoMnO_7$, $177.9(5)^{\circ}$, is greater than that of $Sr_2LaFeMnO_7$, $175.5(8)^{\circ}$.

3.2.3 MAGNETIC PROPERTIES

The change in the B-site cation results in significant changes in magnetic properties.

Figures 3.5a and **b** illustrate the magnetic susceptibility (χ) of $Sr_2LaCoMnO_7$ and

$\text{Sr}_2\text{LaFeMnO}_7$ in the temperature range 2 K – 400 K. The magnetic susceptibility data for $\text{Sr}_2\text{LaCoMnO}_7$ indicate a transition at ~85 K and splitting of the zero-field-cooled (ZFC) and field-cooled (FC) data below ~70 K. This is similar to the behavior that was previously reported for this material and was attributed to a spin-glass transition.^{105, 108} The spin-glass state was explained in terms of competing ferromagnetic ($\text{Mn}^{4+}\text{-Co}^{3+}$) and antiferromagnetic ($\text{Mn}^{4+}\text{-Mn}^{4+}$ and $\text{Co}^{3+}\text{-Co}^{3+}$) superexchange interactions.¹⁰⁵

To determine the effect of the change in B-site cation, we also obtained magnetic susceptibility data for $\text{Sr}_2\text{LaFeMnO}_7$, which showed a similar behavior to the Co-analogue, but with a less pronounced transition occurring at ~150 K. Similar to the Co-analogue discussed above, competing ferromagnetic ($\text{Mn}^{4+}\text{-Fe}^{3+}$) and antiferromagnetic ($\text{Mn}^{4+}\text{-Mn}^{4+}$ and $\text{Fe}^{3+}\text{-Fe}^{3+}$) superexchange couplings are expected. The greater magnetic moment of Fe^{3+} compared with Co^{3+} is likely the reason for the observation of the magnetic transition at a higher temperature for $\text{Sr}_2\text{LaFeMnO}_7$ than $\text{Sr}_2\text{LaCoMnO}_7$.

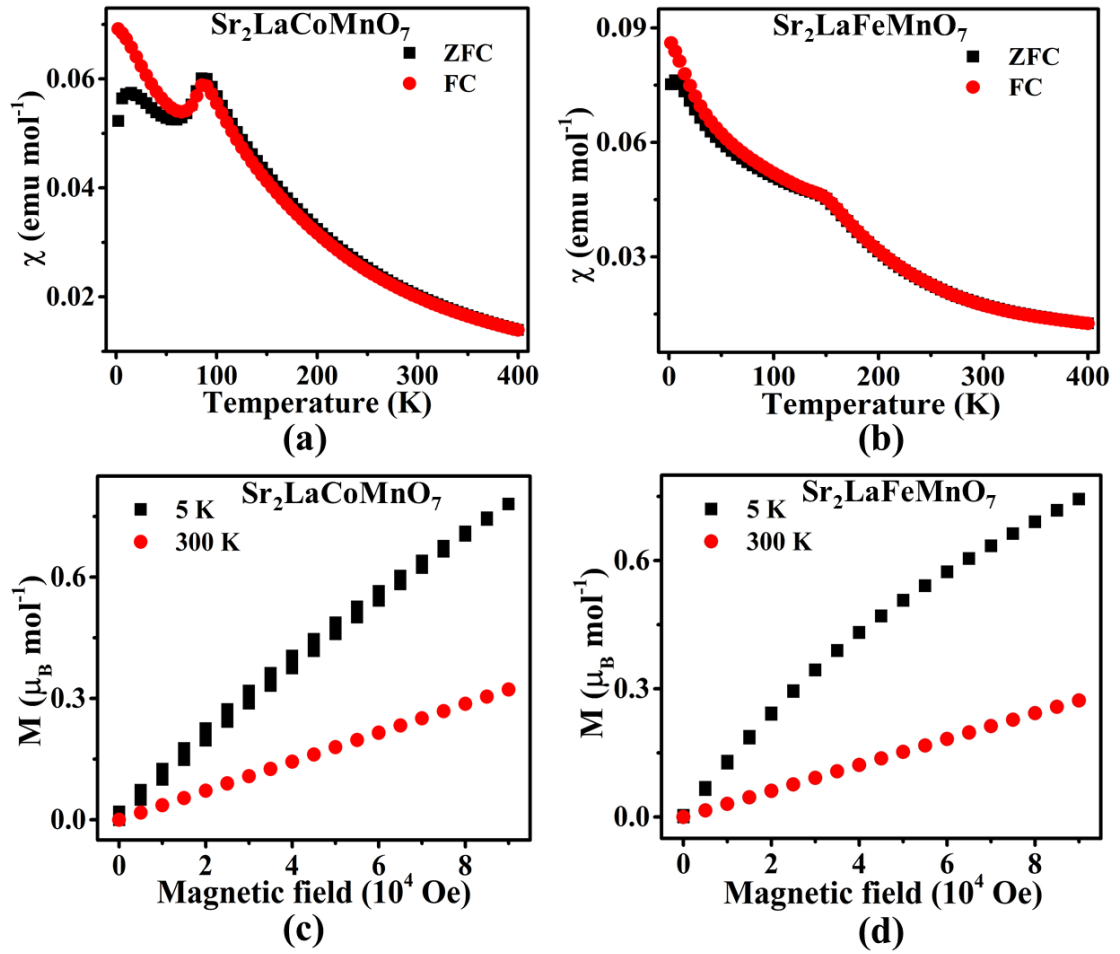


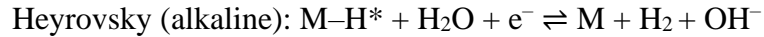
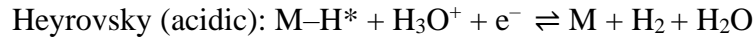
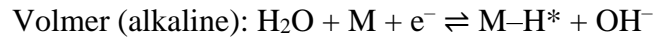
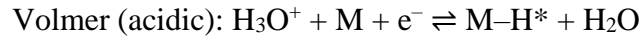
Figure 3.5: (a) and (b) show zero-field-cooled (ZFC) and field-cooled (FC) magnetic susceptibility data. (c) and (d) show the isothermal magnetization data as a function of magnetic field.

The isothermal field sweep data were obtained for both compounds at 5 K and 300 K, as shown in **Figure 3.5c** and **d**. The data at 300 K are linear for both materials, as expected for a paramagnetic state. However, at 5 K, deviations from linear behavior are observed for both compounds, with Sr₂LaMnCoO₇ showing small hysteresis, indicating the presence of uncompensated moments at low temperature.

Overall, the main effect of the change in the B-site cation is the shift in the magnetic transition temperature from ~85 K for Sr₂LaCoMnO₇ to ~150 K in Sr₂LaFeMnO₇.

3.2.4 ELECTROCATALYTIC ACTIVITY FOR HER

The change in the B-site cation has a major impact on the electrocatalytic activity toward both hydrogen-evolution reaction (HER) and oxygen-evolution reaction (OER). The broadly accepted mechanism for HER starts with Volmer reaction, followed by either Heyrovsky or Tafel reaction.^{58, 102}



In this work, the HER experiments were initially performed in typical alkaline conditions (1 M KOH),^{27, 109} showing little electrocatalytic activity. Therefore, the acidic conditions, 0.1 M HClO₄ and 0.5 M H₂SO₄, which are common in HER experiments,^{53, 110} were evaluated. While 0.1 M HClO₄ led to low HER activity, better performance was observed in 0.5 M H₂SO₄. As shown in **Figure 3.6a**, under this condition, Sr₂LaCoMnO₇ shows considerably better electrocatalytic properties for HER than Sr₂LaFeMnO₇. The HER overpotential at 10 mA/cm², η_{10} , is -693 mV for the latter and -612 mV for the former, which also shows a greater current response. In addition, HER data using Pt/C catalyst was also obtained as a reference, giving overpotential of $\eta_{10} \approx 20$ mV consistent with previous reports.^{93, 94} The HER activities of Sr₂LaFeMnO₇ and Sr₂LaCoMnO₇ are not as high as those observed for Pt/C^{93, 94} or some oxide catalysts such as SrCa₂GaMn₂O₈ ($\eta_{10} = -315$ mV).²⁷ However, the activity of Sr₂LaCoMnO₇ is better than that of some other oxide

electrocatalysts such as TiO_{2-x} ($\eta_{10} = -630 \text{ mV}$)⁹⁷ and WO_3 ($\eta_{10} = -637 \text{ mV}$).⁹⁶ The reaction kinetics was evaluated using Tafel equation,¹¹¹ $\eta = a + b \log j$, where η is the overpotential and j is the current density. The slope of the Tafel plot, η vs $\log j$, is affected by electron and mass transport. Smaller Tafel slopes indicate faster reaction kinetics. As shown in **Figure 3.6b**, the Tafel slopes are 239 mV/dec and 141 mV/dec for $\text{Sr}_2\text{LaFeMnO}_7$ and $\text{Sr}_2\text{LaCoMnO}_7$, respectively. This is consistent with greater electrocatalytic activity of $\text{Sr}_2\text{LaCoMnO}_7$, which also shows a stable response in chronopotentiometry data for 12 hours, as shown in **Figure 3.6c**.

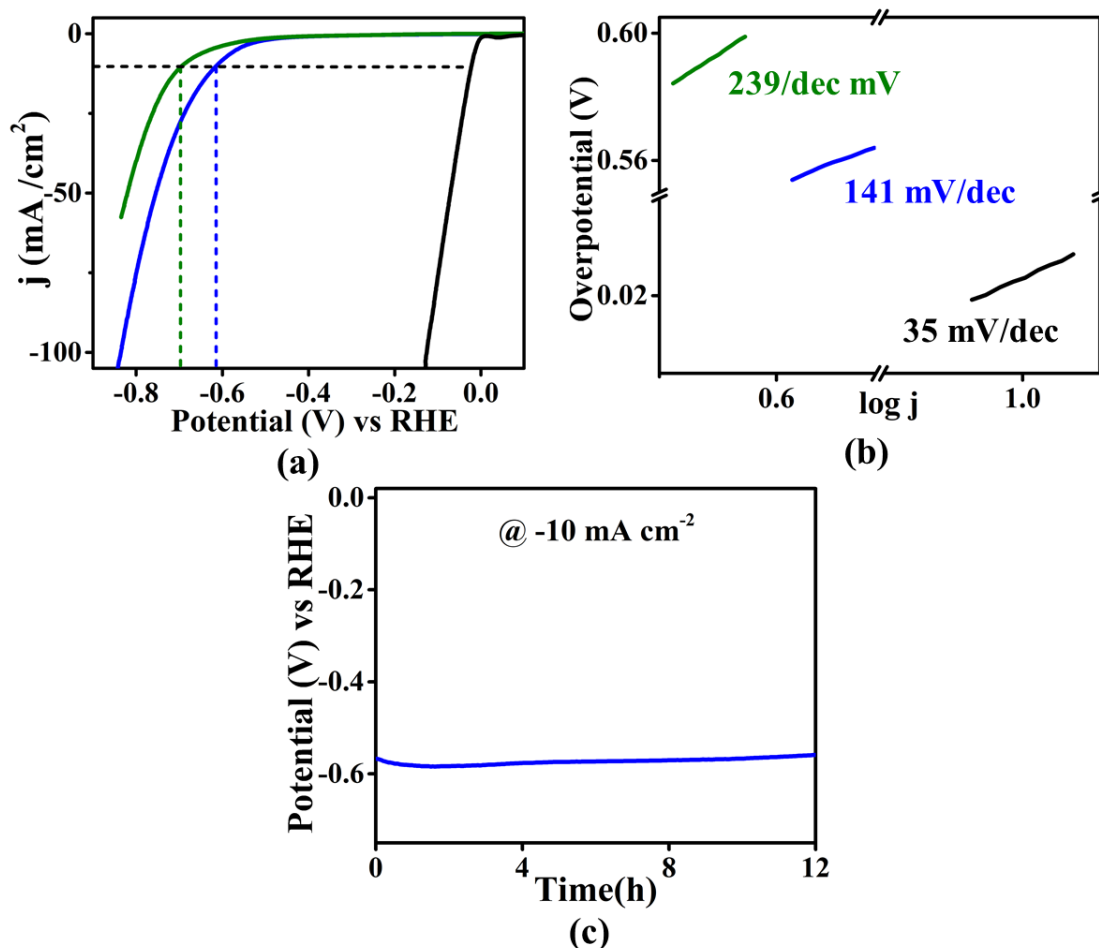
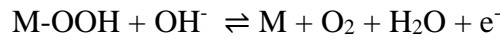
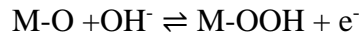
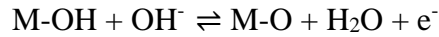
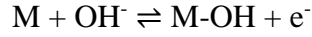


Figure 3.6: HER activity in 0.5 M H_2SO_4 for $\text{Sr}_2\text{LaFeMnO}_7$ (green), $\text{Sr}_2\text{LaCoMnO}_7$ (blue), and Pt/C (black): (a) Polarization curves. (b) Tafel plots. (c) Chronopotentiometry for $\text{Sr}_2\text{LaCoMnO}_7$.

3.2.5 ELECTROCATALYTIC ACTIVITY FOR OER

The OER in alkaline environment has been described as a multi-step process, as shown below:^{58, 59}



Similarly the OER mechanism in acidic condition has been described as follows:^{58, 59}

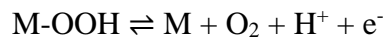


Figure 3.7a shows polarization curves for the OER activity of both $\text{Sr}_2\text{LaFeMnO}_7$ and $\text{Sr}_2\text{LaCoMnO}_7$ in a typical OER electrolyte, 0.1 M KOH. As evident from these data, the change in B-site metal results in a significant improvement in the OER activity. The OER overpotential, η_{10} , beyond the ideal potential of 1.23 V, is evaluated at 10 mA/cm². The polarization curve for $\text{Sr}_2\text{LaFeMnO}_7$ does not even reach 10 mA/cm², indicating the low OER activity of this compound. On the other hand, $\text{Sr}_2\text{LaCoMnO}_7$ shows overpotential of $\eta_{10} = 538$ mV. In addition, OER data using IrO_2 catalyst was also obtained as a reference, giving overpotential of $\eta_{10} \approx 400$ mV, consistent with previous reports.^{112, 113} The OER activities of $\text{Sr}_2\text{LaFeMnO}_7$ and $\text{Sr}_2\text{LaCoMnO}_7$ are not as high as those observed for some oxides such as IrO_2 ,^{112, 113} RuO_2 ($\eta_{10} \approx 420$ mV)¹¹⁴ and $\text{CaSrFeMnO}_{6-\delta}$ ($\eta_{10} = 370$ mV).⁵³

However, the activity of $\text{Sr}_2\text{LaCoMnO}_7$ is close to that of the well-known oxide catalyst BSCF ($\eta_{10} \approx 500$ mV).¹¹³ In addition, its activity is superior to some other reported OER electrocatalysts, such as $\text{La}_{0.5}\text{Sr}_{0.5}\text{Co}_{0.8}\text{Fe}_{0.2}\text{O}_3$ ($\eta_{10} = 600$ mV)¹¹⁵, $\text{La}_{0.6}\text{Sr}_{0.4}\text{CoO}_{3-\delta}$ ($\eta_{10} = 590$ mV)¹¹⁶, and $\text{La}_{0.5}\text{Sr}_{0.5}\text{CoO}_{3-\delta}$ ($\eta_{10} = 600$ mV).¹¹⁷

The significant difference in the catalytic activity is also evident from the OER kinetics, evaluated using the Tafel plot in **Figure 3.7b**. The Tafel slope for $\text{Sr}_2\text{LaCoMnO}_7$ is 123 mV/dec as compared to 151 mV/dec for $\text{Sr}_2\text{LaFeMnO}_7$. In addition, chronopotentiometry data for $\text{Sr}_2\text{LaCoMnO}_7$ show a stable response for 12 hours, as shown in **Figure 3.7c**.

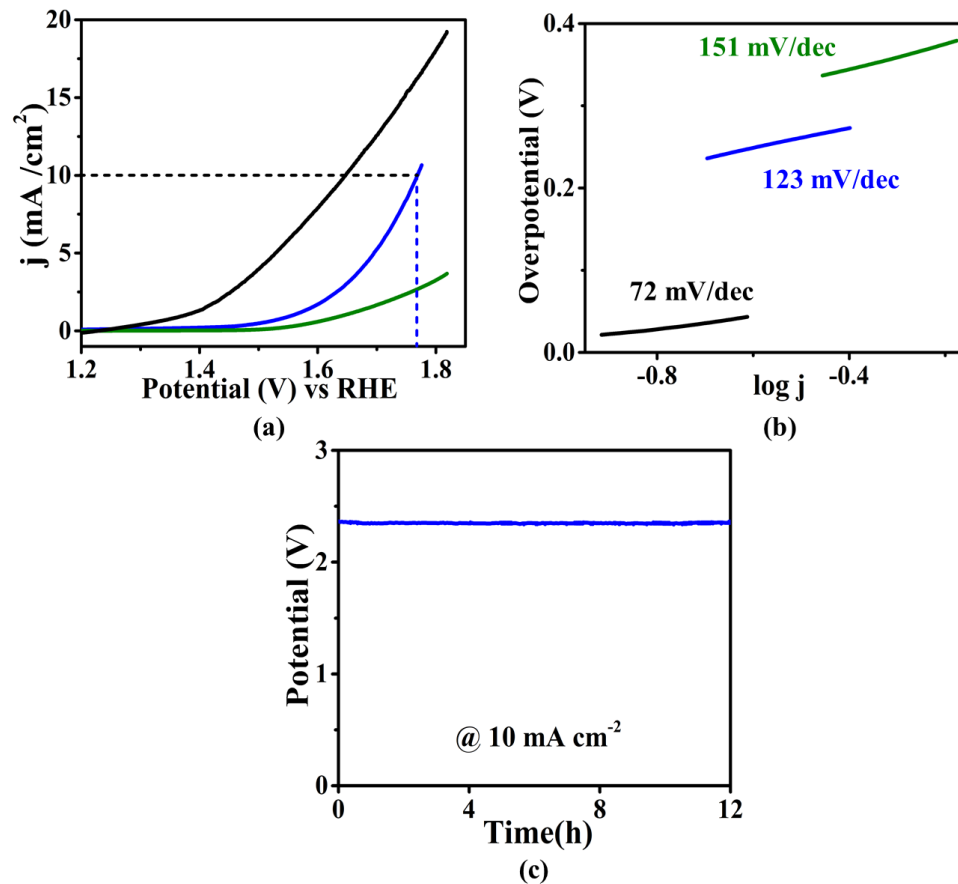


Figure 3.7: OER activity in 0.1 M KOH for $\text{Sr}_2\text{LaFeMnO}_7$ (green), $\text{Sr}_2\text{LaCoMnO}_7$ (blue), and IrO_2 (black): (a) Polarization curves. (b) Tafel plots. (c) Chronopotentiometry response of $\text{Sr}_2\text{LaCoMnO}_7$.

Furthermore, the electrochemically active surface areas (ECSA) were evaluated for the two materials. The ECSA is related to double-layer capacitance (C_{dl}) through the equation $ECSA=C_{dl}/C_s$, where C_s is specific capacitance. Given the direct relationship between ECSA and C_{dl} , it is common to use the value of C_{dl} as an indication of the magnitude of ECSA.^{54, 100} The double layer capacitance is obtained using cyclic voltammetry data in the non-Faradaic region (**Figure 3.8a** and **b**), where the electrode reactions are insignificant and the current originates from electrical double layer charge and discharge. The C_{dl} is evaluated using the relationship $C_{dl} = j_{average}/v$, where v is the scan rate and $j_{average}$ is the average of the absolute values of j_{anodic} and $j_{cathodic}$ from cyclic voltammetry.¹⁰⁰ Therefore, the value of C_{dl} is obtained using the slope of the plot of $j_{average}$ versus v . As shown in **Figure 3.8c**, $Sr_2LaCoMnO_7$ has a significantly greater C_{dl} , which is consistent with the higher electrocatalytic activity of this material compared with $Sr_2LaFeMnO_7$. X-ray diffraction data before and after 1000 cycles of OER showed a small shift of diffraction peaks to the right, but indicated the retention of the structural integrity of $Sr_2LaCoMnO_7$ upon its application as an electrocatalyst, as shown in **Figure 3.9**.

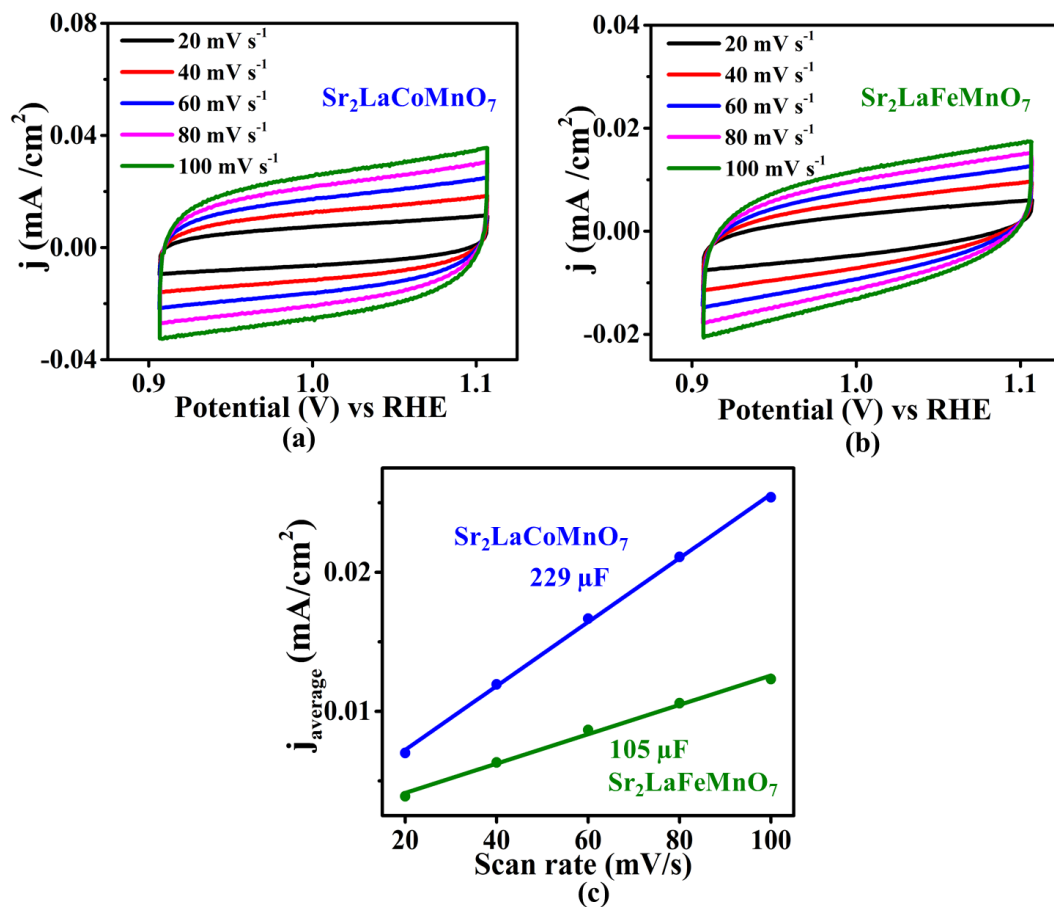


Figure 3.8: (a) and (b) cyclic voltammetry in non-Faradaic region in 0.1 M KOH. (c) j_{average} obtained from these CV plotted as a function of scan rate. The slope gives double layer capacitance.

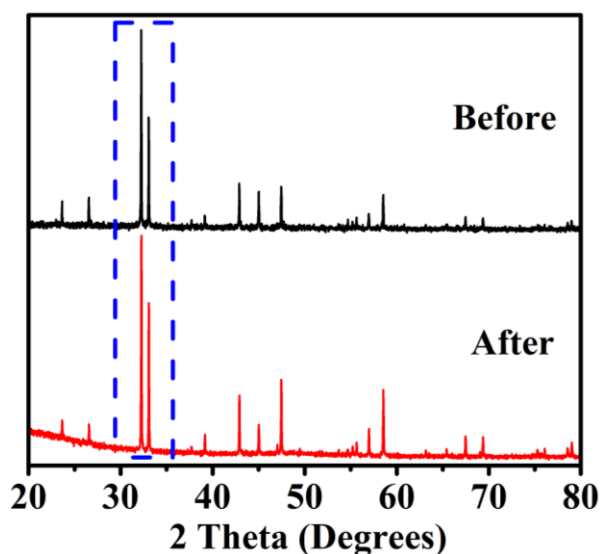


Figure 3.9: X-ray diffraction data for $\text{Sr}_2\text{LaCoMnO}_7$ before and after 1000 cycles of OER.

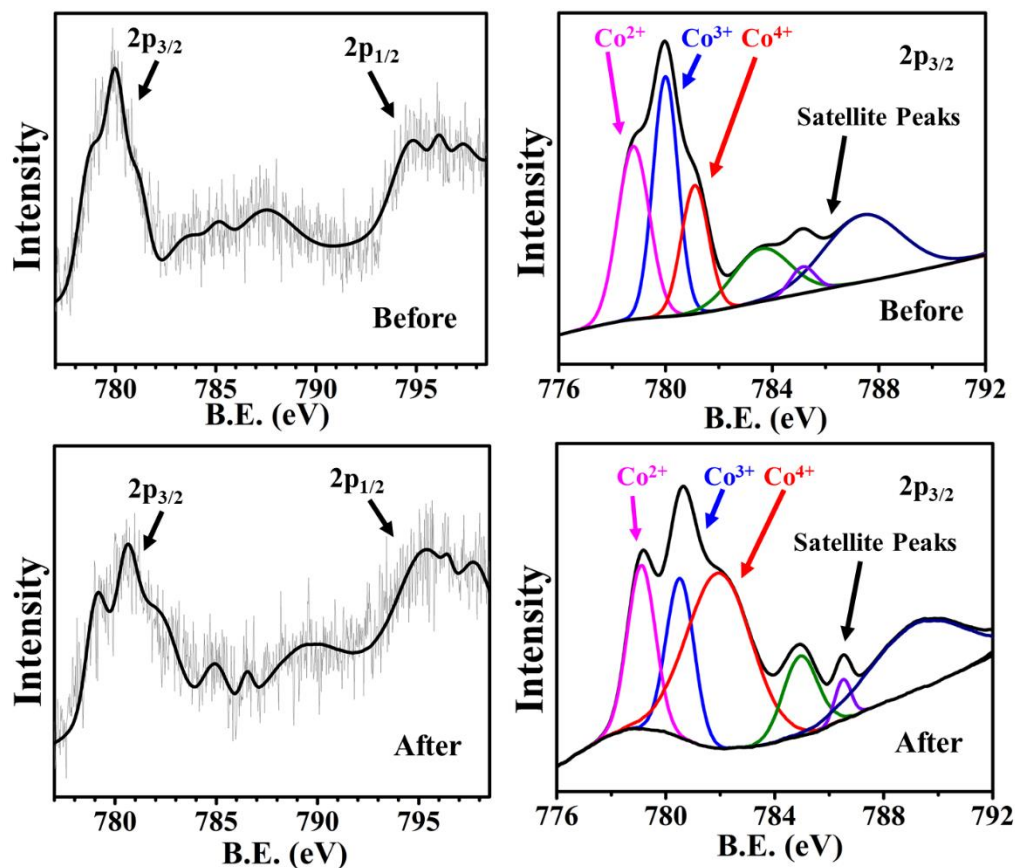


Figure 3.10: X-ray photoelectron spectroscopy data, showing cobalt binding energies, for $\text{Sr}_2\text{LaCoMnO}_7$ before (top) and after (bottom) 1000 cycles of OER.

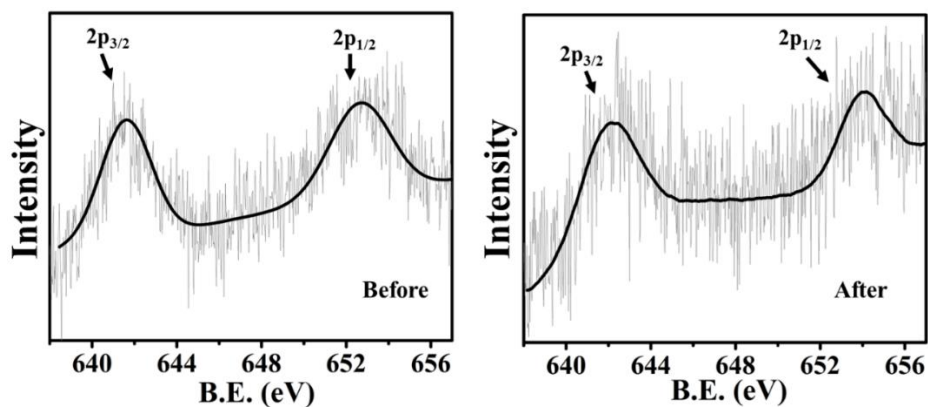


Figure 3.11: X-ray photoelectron spectroscopy data, showing manganese binding energies, for $\text{Sr}_2\text{LaCoMnO}_7$ before and after 1000 cycles of OER.

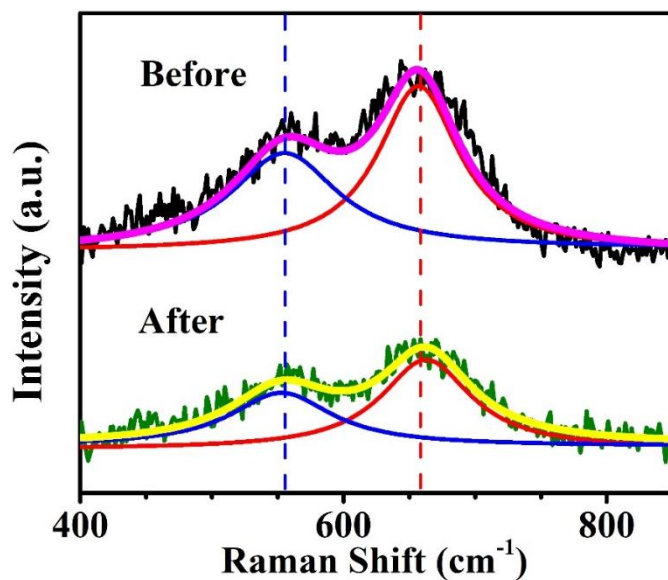


Figure 3.12: Raman spectroscopy data for $\text{Sr}_2\text{LaCoMnO}_7$ before and after 1000 cycles of OER.

In addition, X-ray photoelectron spectroscopy data for $\text{Sr}_2\text{LaCoMnO}_7$ before and after 1000 cycles of OER (**Figures 3.10** and **3.11**), indicated a small shift of the binding energies to the right, which could indicate a small increase in the average oxidation states of metal, but the material retains the same types of metal oxidation states, as shown in **Figures 3.10** and **3.11**. Moreover, as shown in **Figure 3.12**, the Raman shifts for the main bands remain almost the same, indicating the retention of the structural integrity of the catalyst.

The enhanced electrocatalytic properties of $\text{Sr}_2\text{LaCoMnO}_7$ over $\text{Sr}_2\text{LaFeMnO}_7$ can be explained in terms of greater electronegativity of Co compared to Fe, which leads to a decrease in metal-to-ligand charge-transfer energy^{118, 119} as well as a higher degree of covalency for the bonds between the transition metal and oxygen.¹²⁰ The improved covalency has been shown to positively impact the electrocatalytic activity, particularly for OER, where better overlap between metal d and oxygen p orbital is achieved.¹²⁰

Another parameter that has been shown to correlate with the electrocatalytic activity of some oxide materials is the electron occupancy of the e_g orbitals, which affects the strength of sigma bonding between the catalyst and reaction intermediates.¹²¹ It has been suggested that e_g orbital occupancy of ~ 1 is optimum for achieving enhanced electrocatalytic properties.¹²² The two compounds $\text{Sr}_2\text{LaFeMnO}_7$ and $\text{Sr}_2\text{LaCoMnO}_7$ contain Fe^{3+} and Co^{3+} , respectively. Trivalent Fe is often in high spin state in perovskite-related oxides, giving $t_{2g}^3 e_g^2$. However, previous studies have shown intermediate spin for Co^{3+} in perovskite-related oxides,^{122, 123} which gives $t_{2g}^5 e_g^1$, where the e_g orbital occupancy is 1. This could be another parameter that explains the higher electrocatalytic activity of $\text{Sr}_2\text{LaCoMnO}_7$.

3.3 CONCLUSIONS

Functional properties of Ruddlesden-Popper oxides can be changed by varying the B-site cation. We have shown that magnetic transition temperature can be shifted significantly by changing the B-site cation from Fe^{3+} to Co^{3+} . In addition, charge transport properties can be enhanced. $\text{Sr}_2\text{LaCoMnO}_7$ shows considerably greater electrical conductivity than $\text{Sr}_2\text{LaFeMnO}_7$. Furthermore, the change in the B-site cation helps to improve the electrocatalytic activity toward hydrogen-evolution reaction (HER) and oxygen-evolution reactions (OER). $\text{Sr}_2\text{LaCoMnO}_7$ shows significantly enhanced catalytic activity for both HER and OER, as well as better reaction kinetics and electrochemically active surface area. These changes are assigned to the higher electronegativity of Co compared to Fe, resulting in greater bond covalency and better overlap of metal-oxygen orbitals. In addition, the

electronic configuration and the eg orbital occupancy may play a role in the improvement of electrocatalytic properties in $\text{Sr}_2\text{LaCoMnO}_7$ as compared to $\text{Sr}_2\text{LaFeMnO}_7$.

CHAPTER 4

SYSTEMATIC VARIATION OF ELECTROCATALYTIC ACTIVITY FOR WATER SPLITTING IN ISOSTRUCTURAL OXIDES $\text{Sr}_3\text{Ti}_{2-x}\text{M}_x\text{O}_{7-\delta}$ ($\text{M} = \text{Mn}, \text{Fe}, \text{Co}; x = 0,$

1)³

4.1 EXPERIMENTAL

4.1.1 SYNTHESIS

Syntheses were performed using the solid-state method. Powders of SrCO_3 , TiO_2 , Mn_2O_3 , Fe_2O_3 , Co_3O_4 were used to synthesize $\text{Sr}_3\text{Ti}_2\text{O}_7$, $\text{Sr}_3\text{TiMnO}_7$, $\text{Sr}_3\text{TiFeO}_{7-\delta}$ and $\text{Sr}_3\text{TiCoO}_{7-\delta}$. Stoichiometric amounts of oxides/carbonates were weighed and mixed thoroughly using agate mortar and pestle. The powder mixtures for $\text{Sr}_3\text{Ti}_2\text{O}_7$, $\text{Sr}_3\text{TiMnO}_7$, and $\text{Sr}_3\text{TiCoO}_{7-\delta}$ were initially pelletized and calcinated in air at 1250 °C for 24 hours. Pure products of $\text{Sr}_3\text{Ti}_2\text{O}_7$ and $\text{Sr}_3\text{TiCoO}_{7-\delta}$ could be obtained after one additional grinding, palletization and heating at the same temperature, 1250 °C, for 24 hours. On the other hand, for $\text{Sr}_3\text{TiMnO}_7$, after the initial heating at 1250 °C, three additional re-palletization and re-heating were required, at 1250 °C for 24 hours each, to obtain a pure product. For $\text{Sr}_3\text{TiFeO}_{7-\delta}$, a lower temperature (1180 °C) was needed to obtain a pure product. Synthesis efforts at 1250 °C led to an impure product. However, heating at 1180 °C for 10 hours in air, followed by

³ The work described in this chapter was published in *Inorganics*. **2023**, 11, 172.

grinding, re-palletization and re-heating under the same conditions, 1180 °C for 10 hours in air, resulted in a pure product of $\text{Sr}_3\text{TiFeO}_{7-\delta}$. The heating and cooling rates of furnaces for all samples were 100 °C/hour.

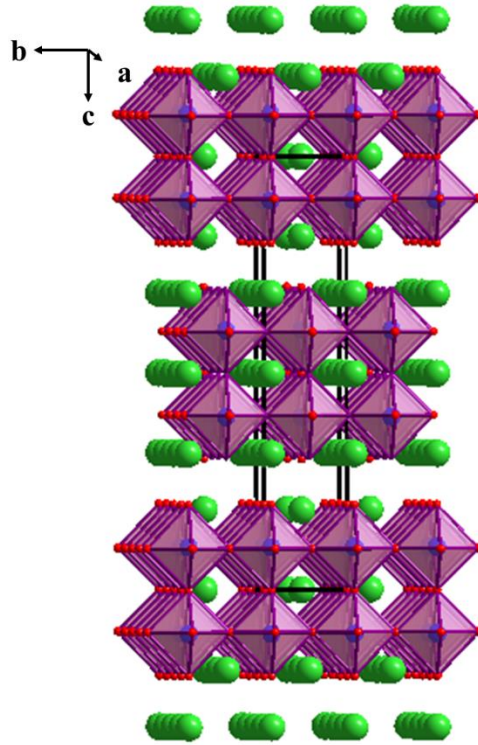


Figure 4.1: Crystal structure of Sr_3TiMO_7 ($M = \text{Ti}, \text{Mn}, \text{Fe}, \text{Co}$). Green spheres represent La, and red spheres show oxygens. The BO_6 octahedra are shown purple in color.

4.1.2 CHARACTERIZATION

The synthesized polycrystalline oxides were studied using a high-resolution Cu $K\alpha 1$ X-ray diffractometer ($\lambda = 1.54056 \text{ \AA}$). Rietveld refinements for the X-ray diffraction data were carried out using GSAS software⁷⁶ and EXPGUI interface.⁷⁷ A representative quasi-two-dimensional Ruddlesden Popper (RP) structure with formula Sr_3TiMO_7 ($M = \text{Ti}, \text{Mn}, \text{Fe}, \text{Co}$) is shown in **Figure 4.1**. The electrical conductivity measurements were done using

the two-probe technique on circular pellets, with an applied potential of 0.01 V in the temperature range of 25 to 800 °C. Iodometric titrations were performed to examine the oxygen contents of the materials.⁹⁹

4.1.3 ELECTROCHEMICAL OER/HER MEASUREMENTS

The catalyst ink of each material was prepared by mixing 35 mg of the powder sample, 7 mg of carbon black powder, 40 µL Nafion® D-521 solution (5% w/w in water and 1-propanol) with 7 ml of THF (99%). The mixture was then sonicated for 30 minutes. Glassy carbon electrode (GCE, 5 mm diameter, 0.196 cm² area) was used as the working electrode and was thoroughly cleaned prior to use. In the cleaning process, the GCE was refurbished using aluminum oxide polishing suspension on a polishing cloth and sonicated for 2-3 minutes in ethanol. At the end of the cleaning steps, GCE was washed with deionized water before use. After sonication, the prepared catalyst ink was drop-casted on the glassy carbon electrode by placing two 10 µl coats (total of 20 µl) with a 2-minute interval between the coats. Total catalyst mass loading on the GCE was 0.1 mg. Subsequently, the loaded GCEs were air-dried overnight before the OER/HER electrochemical measurements. Both acidic and basic electrolytes were tested. The electrochemical OER/HER measurements were performed in a standard three-electrode cell using a rotating disk electrode at 1600 rpm. A platinum electrode and a carbon electrode were used as counter electrodes in the OER and HER measurements, respectively. A commercial Hg/HgO electrode (1 M NaOH) was used for the OER/HER measurements in the basic medium as the reference electrode. The potential versus mercury/mercury oxide ($E_{\text{Hg}/\text{HgO}}$) was converted to be expressed against RHE using the equation $E_{\text{RHE}} = E_{\text{Hg}/\text{HgO}} + 0.059 \text{ pH} + E^0_{\text{Hg}/\text{HgO}}$, where $E^0_{\text{Hg}/\text{HgO}} = 0.097$ for 1 M NaOH.²⁶ A commercial Ag/AgCl electrode (4 M KCl) was used as the reference

electrode for OER/HER experiments in the acidic medium. The equation $E_{\text{RHE}} = E_{\text{Ag/AgCl}} + 0.059 \text{ pH} + E^0_{\text{Ag/AgCl}}$ was used to convert the potential vs silver/silver chloride ($E_{\text{Ag/AgCl}}$) to be represented against RHE where $E^0_{\text{Ag/AgCl}} = 0.197 \text{ V}$ for 4 M KCl.^{85, 86} Chronopotentiometry tests were conducted using two-electrode cells, with applied current of 10 mA. Each electrode was comprised 1 cm² of nickel foam, on which 100 μl of the catalyst ink had been drop-casted in 20 μl increments, followed by overnight air-drying. The two electrodes, which had been separated by two layers of glass fiber filter paper, were connected to gold leads and gold wires. The two electrodes were soaked in the electrolyte solution for least 12 hours before performing the chronopotentiometry experiments.

4.2 RESULTS AND DISCUSSION

4.2.1 CRYSTAL STRUCTURE AND OXYGEN CONTENT

The crystal structures of the materials were verified by Rietveld refinements using powder X-ray diffraction data. The refinement profiles are shown in **Figure 4.2** and the refined structural parameters are listed in **Table 4.1-4.4**. The quasi-two-dimensional network of these RP materials, $A_{n-1}A'_2B_nO_{3n+1}$ ($n=2$), consists of bilayer stacks of BO_6 octahedra, where B-site is occupied by transition metals. The spaces between the octahedra are occupied by A and A' metals, which reside on intra-stack and inter-stack sites, with coordination numbers 12 and 9, respectively. In the materials studied here, both A and A' sites are occupied by Sr. On the other hand, the B-site is occupied by Ti in $\text{Sr}_3\text{Ti}_2\text{O}_7$,²¹ and a mix of Ti/Mn, Ti/Fe or Ti/Co for $\text{Sr}_3\text{TiMnO}_7$,¹²⁴ $\text{Sr}_3\text{TiFeO}_{7-\delta}$,¹²⁵ and $\text{Sr}_3\text{TiCoO}_{7-\delta}$,¹²⁶ respectively.

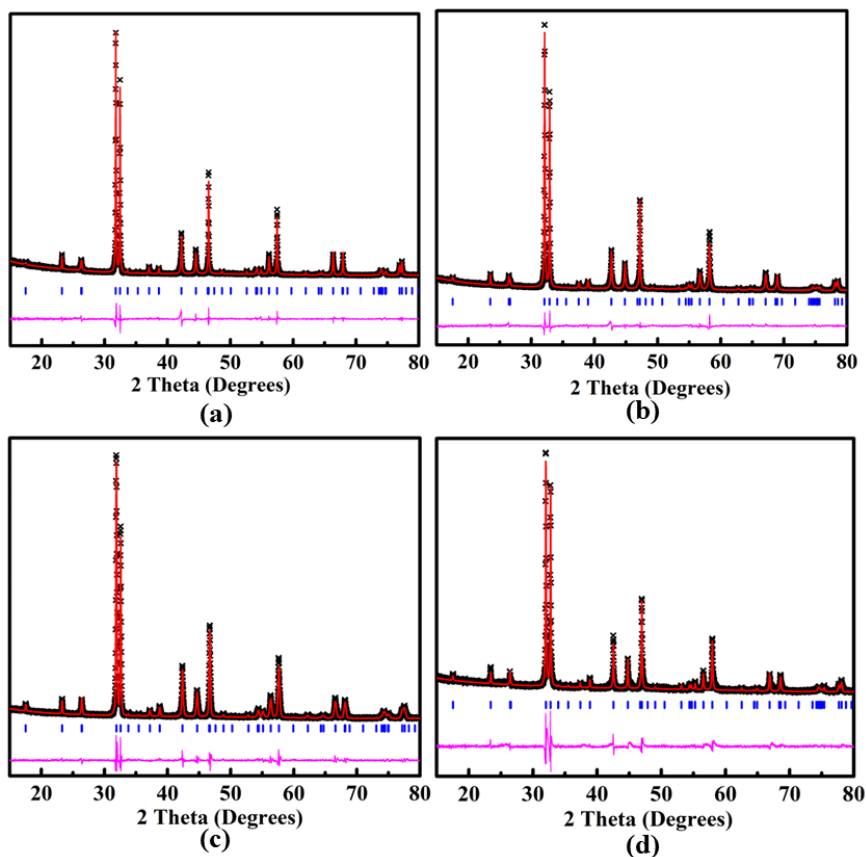


Figure 4.2: Rietveld refinement profiles with powder X-ray diffraction data for (a) $\text{Sr}_3\text{Ti}_2\text{O}_7$, (b) $\text{Sr}_3\text{TiMnO}_7$, (c) $\text{Sr}_3\text{TiFeO}_{7.8}$, and (d) $\text{Sr}_3\text{TiCoO}_{7.8}$. The experimental data are represented by black crosses. The red line shows the fit. The vertical blue tick marks and the lower pink line correspond to the Bragg peak positions and difference plot, respectively.

Table 4.1: Refined structural parameters of $\text{Sr}_3\text{Ti}_2\text{O}_7$ from powder X-ray diffraction data. Space group: $I4/mmm$, $a = b = 3.9009(1)$ Å, $c = 20.3386(5)$ Å, $R_p = 0.0702$, $wR_p = 0.0949$

Atom	x	y	z	Occupancy	$U_{\text{iso}} (\text{Å}^2)$	Multiplicity
Sr1	0	0	0.5	1	0.0327(18)	2
Sr2	0	0	0.31421(16)	1	0.0390(18)	4
Ti	0	0	0.09932(27)	1	0.0158(28)	4
O1	0	0	0	1	0.090(8)	2
O2	0	0	0.1882(12)	1	0.090(8)	4
O3	0	0.5	0.0979(6)	1	0.090(8)	8

Table 4.2: Refined structural parameters of Sr₃TiMnO₇ from powder X-ray diffraction data. Space group: *I4/mmm*, $a = b = 3.8481(1)$ Å, $c = 20.2024(6)$ Å, $R_p = 0.0446$, $wR_p = 0.0585$

Atom	x	y	z	Occupancy	U _{iso} (Å ²)	Multiplicity
Sr1	0	0	0.5	1	0.021(4)	2
Sr2	0	0	0.30097(12)	1	0.040(4)	4
Ti	0	0	0.11764(17)	0.5	0.034(4)	4
Mn	0	0	0.11764(17)	0.5	0.034(4)	4
O1	0	0	0	1	0.039(5)	2
O2	0	0	0.1897(7)	1	0.039(5)	4
O3	0	0.5	0.0759(4)	1	0.039(5)	8

Table 4.3: Refined structural parameters of Sr₃TiFeO_{7-δ} from powder X-ray diffraction data. Space group: *I4/mmm*, $a = b = 3.8904(1)$ Å, $c = 20.2788(7)$ Å, $R_p = 0.0326$, $wR_p = 0.0459$

Atom	x	y	z	Occupancy	U _{iso} (Å ²)	Multiplicity
Sr1	0	0	0.5	1	0.0083(13)	2
Sr2	0	0	0.31585(9)	1	0.0148(10)	4
Ti	0	0	0.10014(20)	0.5	0.0010(9)	4
Fe	0	0	0.10014(20)	0.5	0.0010(9)	4
O1	0	0	0	1	0.0542(17)	2
O2	0	0	0.1980(6)	1	0.0542(17)	4
O3	0	0.5	0.0963(4)	1	0.0542(17)	8

Table 4.4: Refined structural parameters of Sr₃TiCoO_{7-δ} from powder X-ray diffraction data. Space group: *I4/mmm*, $a = b = 3.8682(1)$ Å, $c = 20.2349(8)$ Å, Rp = 0.0361, wRp = 0.0545

Atom	x	y	z	Occupancy	U _{iso} (Å ²)	Multiplicity
Sr1	0	0	0	1	0.031(6)	2
Sr2	0	0	0.18493(21)	1	0.052(6)	4
Ti	0	0	0.4010(5)	0.5	0.050(6)	4
Co	0	0	0.4010(5)	0.5	0.050(6)	4
O1	0	0	0.5	1	0.080(8)	2
O2	0	0	0.3126(13)	1	0.080(8)	4
O3	0	0.5	0.0940(11)	1	0.080(8)	8

Iodometric titrations were carried out to examine the oxygen stoichiometries, which indicated 7 oxygens per formula unit for Sr₃Ti₂O₇ and Sr₃TiMnO₇, but 6.76 and 6.62 oxygens per formula unit for Sr₃TiFeO_{7-δ} and Sr₃TiCoO_{7-δ}, respectively. We note that all materials were synthesized under similar conditions in air, and no reduction experiment was done on any of these materials. It appears that the latter two materials have a tendency to accommodate cations with a lower oxidation state, possibly due to the relative stability of trivalent iron and cobalt. These findings are consistent with the observation of larger unit cell volumes for Sr₃TiFeO_{7-δ}¹²⁵ and Sr₃TiCoO_{7-δ},¹²⁶ indicating more reduced transition metals due to the lower oxygen stoichiometry. We note that ionic radii⁸⁷ of Fe³⁺ (0.645 Å) and Co³⁺ (0.61 Å) are considerably larger than those of Fe⁴⁺ (0.585 Å) and Co⁴⁺ (0.53 Å), respectively.

As shown in **Table 4.5**, the BO_6 octahedra in these materials are distorted, where the axial bond lengths are dissimilar. The distortions are also evident from the B-O-B bond angles, which deviate from the ideal 180° . $\text{Sr}_3\text{TiMnO}_7$ exhibits the highest distortion of angles, while $\text{Sr}_3\text{Ti}_2\text{O}_7$ exhibits the lowest, as indicated by the bond angles reported in **Table 4.5**.

Table 4.5: B-O bond distances and B-O-B angles for the synthesized structures.

$\text{Sr}_3\text{Ti}_2\text{O}_7$		$\text{Sr}_3\text{TiMnO}_7$	
Ti-O1	2.020(6)	Ti/Mn-O1	2.3766(35)
Ti-O2	1.808(23)	Ti/Mn-O2	1.456(12)
Ti-O3 x 4	1.95065(20)	Ti/Mn-O3 x 4	2.1006(31)
Average Ti-O	1.9384(19)	Average Ti/Mn -O	2.0391(29)
Ti-O1-Ti	180.0(0)	Ti/Mn-O1- Ti/Mn	180.0(0)
Ti-O3-Ti	178.3 (8)	Ti/Mn-O3- Ti/Mn	132.7(4)
Average Ti-O-Ti	179.2(6)	Average Ti/Mn-O- Ti/Mn	156.35(3)
$\text{Sr}_3\text{TiFeO}_{7-\delta}$		$\text{Sr}_3\text{TiCoO}_{7-\delta}$	
Ti/Fe-O1	2.031(4)	Ti/Co-O1	2.003(11)
Ti/Fe -O2	1.984(13)	Ti/Co -O2	1.788(25)
Ti/Fe -O3 x 4	1.9468(4)	Ti/Co -O3 x 4	1.9367(13)
Average Ti/Fe -O	1.9670(6)	Average Ti/Co-O	1.9229(15)
Ti/Fe -O1- Ti/Fe	180.0(0)	Ti/Co -O1- Ti/Co	180.0(0)

Ti/Fe –O3– Ti/Fe	175.4(6)	Ti/Co –O3– Ti/Co	174.0(15)
Average Ti/Fe-O-Ti/Fe	177.7(4)	Average Ti/Co-O-Ti/Co	177.0(11)

4.2.2 ELECTRICAL CONDUCTIVITY

The variable-temperature electrical conductivity of the synthesized materials was studied from the measured resistance (R) using the following equation at a constant applied potential.

$$\sigma = L/RA \quad (1)$$

In the above equation, σ is the conductivity, L is the average thickness, and A ($A = \pi r^2$) is the average cross-sectional area of the pellet. The conductivity values obtained for the materials from 25 °C to 800 °C are given in **Figure 4.3a**. The insets in **Figure 4.3a** show a magnified view of the conductivity variations for $\text{Sr}_3\text{Ti}_2\text{O}_7$ and $\text{Sr}_3\text{TiMnO}_7$. The conductivity of all materials increases as a function of temperature, a behavior typical of semiconducting materials. For $\text{Sr}_3\text{TiCoO}_{7-\delta}$ and $\text{Sr}_3\text{TiFeO}_{7-\delta}$, this increase is observed from 25 °C to 500 °C, followed by a decrease in conductivity as the temperature is raised to 800 °C.

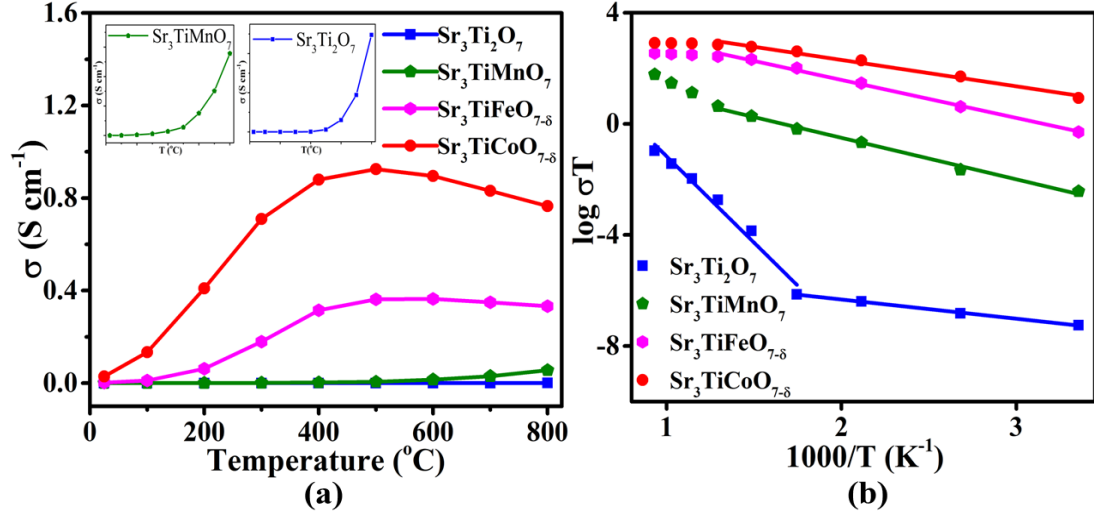


Figure 4.3: (a) Electrical conductivity variation as a function of temperature. The dotted box has been magnified in the inset to show the conductivity variations for Sr₃Ti₂O₇ and Sr₃TiMnO₇. (b) Arrhenius plots for determination of the activation energies (E_a) for the temperature-activated increase in conductivity.

The behavior of these materials can be described by equation 2, where σ , n , e , μ are conductivity, concentration of electrons/holes, charge of the electron, and mobility of the charge-carriers, respectively.²⁷

$$\sigma = ne\mu \quad (2)$$

The characteristic feature of a semiconductor is an increase in the number of charge-carriers as a function of temperature, leading to an increased electrical conductivity. The metallic behavior, i.e., decrease in electrical conductivity as a function of temperature, is explained by an increase in collisions between phonons and charge carriers with increasing temperature, which will decrease the relaxation time, hence lowering the charge-carrier mobility and the electrical conductivity.

The electron/hole hopping in oxides requires the B-site metal to have a variable oxidation state.⁶² Considering that Mn, Fe and Co have multiple stable oxidation states, it is expected

that their presence in Sr_3TiMO_7 ($M = \text{Mn, Fe, Co}$) leads to a higher electrical conductivity compared to $\text{Sr}_3\text{Ti}_2\text{O}_7$. As shown in **Table 4.6**, $\text{Sr}_3\text{Ti}_2\text{O}_7$ has a room temperature conductivity that is at least five orders of magnitude lower than those of the other three materials.

The electrical conduction in perovskite oxides occur through the B-O-B pathways,⁶² facilitated by the overlap of the transition metal 3d orbitals with oxygen 2p orbitals. Shorter B-O bonds and greater B-O-B angles facilitate the conductivity by increasing the orbital overlap.^{53, 91} Therefore, the degree of structural distortion in the structure has an impact on the conductivity.³² As shown in **Table 4.5**, $\text{Sr}_3\text{TiMnO}_7$ exhibits the largest distortion of B-O-B angles. Distortions can hinder the overlap of B-site metal 3d orbitals with oxygen 2p orbitals, leading to lower conductivity. Greater distortions and longer B-O bonds in $\text{Sr}_3\text{TiMnO}_7$ may cause the material to be less conductive. As shown in **Figure 4.3a**, $\text{Sr}_3\text{TiCoO}_{7-\delta}$ shows the highest conductivity in the entire temperature range, followed by $\text{Sr}_3\text{TiFeO}_{7-\delta}$. Oxygen vacancies were found for both materials by iodometric titrations, which indicated that $\text{Sr}_3\text{TiCoO}_{7-\delta}$ has more oxygen vacancies than $\text{Sr}_3\text{TiFeO}_{7-\delta}$. Although B-O-B bond angles in the two materials are similar, $\text{Sr}_3\text{TiCoO}_{7-\delta}$, has a greater conductivity than $\text{Sr}_3\text{TiFeO}_{7-\delta}$, which may be, in part, related to its shorter average B-O bond length (**Table 4.5**), facilitate the orbital overlap.^{53, 91}

The activation energy for the rise in thermally activated conductivity was examined using the Arrhenius equation below:

$$\sigma T = A e^{-\frac{E_a}{2.303 K_B T}} \quad (3)$$

In this equation, σ , A , T , E_a , and K_B represent conductivity, pre-exponential factor, temperature, activation energy, and the Boltzmann constant, respectively. **Figure 4.3b**

shows the Arrhenius plots for the four materials. The calculated activation energies using slopes of the best line of fits in the Arrhenius plots are listed in **Table 4.6**. It is noted that here, the activation energy indicates the energy barrier for the temperature-dependent rise in conductivity.

Table 4.6: Room temperature electrical conductivities and activation energies.

Material	Conductivity at 25 °C (S/cm)	Activation energy (eV)
Sr ₃ Ti ₂ O ₇	1.88719×10^{-10}	0.1372 (298 – 573 K)
		1.2327 (573-1073 K)
Sr ₃ TiMnO ₇	1.2445×10^{-5}	0.2966 (298-773 K)
Sr ₃ TiFeO _{7-δ}	1.72×10^{-3}	0.2714 (298-773 K)
Sr ₃ TiCoO _{7-δ}	2.843×10^{-2}	0.1883 (298-773 K)

4.2.3 ELECTROCATALYTIC PROPERTIES FOR HER AND OER

The HER electrocatalytic activities of the synthesized materials were investigated, showing a systematic change. The overpotential, η_{10} , which is the difference between the experimentally observed potential and the thermodynamic potential at 10 mA cm⁻², is one of the important parameters used to assess the electrocatalytic activity of a catalyst. While the overpotentials of these catalysts are not as low as that those of state-of-the-art HER catalysts, they show a systematic trend in their performance. As illustrated in **Figure 4.4a**, Sr₃TiCoO_{7-δ} shows the lowest overpotential, $\eta_{10} = -424$ mV, indicating better activity compared to the other materials. It is followed by Sr₃TiFeO_{7-δ}, which shows $\eta_{10} = -452$ mV.

The polarization curves for $\text{Sr}_3\text{TiMnO}_7$ and $\text{Sr}_3\text{Ti}_2\text{O}_7$ do not even reach 10 mA cm^{-2} , indicating the low HER activities of these two compounds. The overpotential of the state-of-the-art Pt/C,^{23, 63} as well as those of some oxides, such as $\text{CaSrFeMnO}_{6-\delta}$ ($\eta_{10} = 390 \text{ mV}$)⁵³ and $\text{LaCa}_2\text{Fe}_3\text{O}_8$ ($\eta_{10} = 400 \text{ mV}$),¹⁰¹ are lower than those found in this work. However, the HER overpotentials for the two best materials in this work are smaller than the values reported for some oxides such as TiO_{2-x} ($\eta_{10} = 630 \text{ mV}$).⁹⁷ X-ray diffraction data before and after the HER experiment (**Figure 4.4c**) show that, while some deterioration of the material might be happening, the bulk of the catalyst retains its crystalline structure. As shown in **Figure 4.4d**, chronopotentiometry measurements show a stable current response, indicating that the catalyst remains active for at least 12 hours.

The kinetics of the reaction was evaluated using the Tafel equation $\eta = a + b \log j$, where η is the overpotential and j is the current density. The kinetics of electrocatalytic reactions is dependent on the electron and mass transfers, which are indicated by the Tafel slope. Smaller slopes indicate faster reactions. Among the materials studied here, $\text{Sr}_3\text{TiCoO}_{7-\delta}$ shows the smallest Tafel slope (**Figure 4.4b**), consistent with its higher HER electrocatalytic activity. The trend in kinetics is similar to that of the HER overpotential, where $\text{Sr}_3\text{TiFeO}_{7-\delta}$ and $\text{Sr}_3\text{TiMnO}_7$ have the next lowest Tafel slopes, followed by $\text{Sr}_3\text{Ti}_2\text{O}_7$.

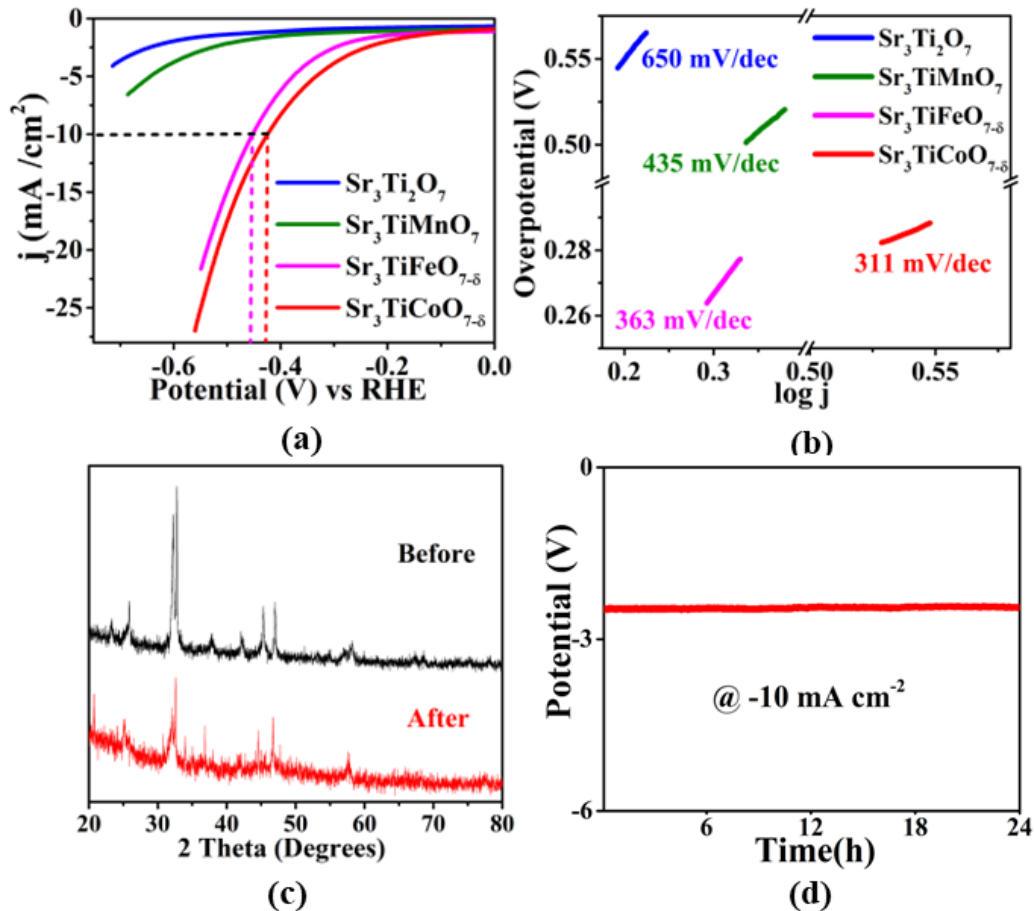


Figure 4.4: HER activity in 0.1 M KOH (a) Polarization curves. (b) Tafel plots. (c) X-ray diffraction data of Sr₃TiCoO_{7-δ}, before and after 100 cycles of OER (d) Chronopotentiometry response of Sr₃TiCoO_{7-δ}.

The electrocatalytic OER activities of the materials were also assessed. As evident from the polarization curves in **Figure 4.5a**, the electrocatalytic activities for OER show the same trend as HER, where Sr₃TiCoO_{7-δ} shows the lowest overpotential, $\eta_{10} = 456$ mV at 10 mA cm⁻², followed by Sr₃TiFeO_{7-δ}, Sr₃TiMnO₇, and Sr₃Ti₂O₇. The difference in activity between the four materials is significant, where the OER responses obtained from latter three materials do not even reach 10 mA cm⁻². However, the systematic change in current density is evident from **Figure 4.5a**. The overpotential (η_{10}) value obtained for Sr₃TiCoO_{7-δ} is lower than those of several oxides that have been reported before, such as

La_{0.5}Sr_{0.5}Co_{0.8}Fe_{0.2}O₃ ($\eta_{10} = 600$ mV)¹¹⁵ and La_{0.6}Sr_{0.4}CoO_{3- δ} ($\eta_{10} = 590$ mV),¹¹⁶ but higher than those of some other oxides, such as CaSrFeMnO_{6- δ} ($\eta_{10} \approx 370$ mV)⁵³ and LaCa₂Fe₃O₈ ($\eta_{10} = 360$ mV)¹⁰¹. The OER kinetics was also studied, where the smallest Tafel slope (Figure 4.5b) was obtained for Sr₃TiCoO_{7- δ} , indicating the fastest kinetics among the series, and consistent with its better OER activity. Chronopotentiometry experiments (Figure 4.5c) for Sr₃TiCoO_{7- δ} indicate a consistent response for at least 12 hours. This is consistent with X-ray diffraction results after the OER, which show the retention of the structural integrity of the material (Figure 4.5d).

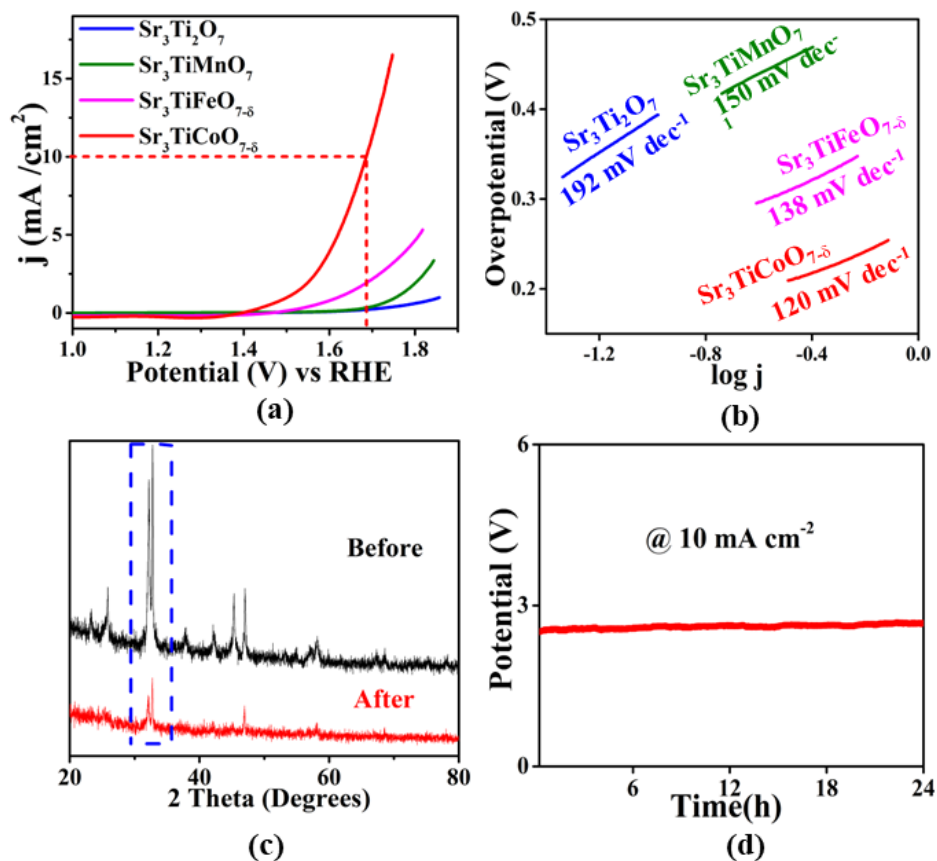


Figure 4.5: OER activity in 0.1 M KOH (a) Polarization curves. (b) Tafel plots. (c) X-ray diffraction data of Sr₃TiCoO_{7- δ} , before and after 100 cycles of OER (d) Chronopotentiometry response of Sr₃TiCoO_{7- δ} .

We also obtained the double-layer capacitance (C_{dl}) based on the equation $C_{dl} = j_{avg}/v$, using cyclic voltammograms acquired in the non-Faradaic region. Here, j_{avg} is the average of the absolute values of j_{anodic} and $j_{cathodic}$ at middle potential of the CV, and v is the scan rate.^{95, 99} In the non-faradaic region, the current is primarily from electrical double-layer charge and discharge where the electrode reactions are insignificant. The importance of C_{dl} is that it is proportional to the electrochemically active surface area.^{34, 54} The cyclic voltammograms obtained for the four compounds in the non-Faradaic region are shown in **Figure 4.6a-4.6d**. Also, the plot of j_{avg} versus v is depicted in **Figure 4.6e**, where the slope indicates the C_{dl} value. Among the four materials, $Sr_3TiCoO_{7-\delta}$ shows the largest C_{dl} , followed by $Sr_3TiFeO_{7-\delta}$, Sr_3TiMnO_7 and $Sr_3Ti_2O_7$. This is the same trend observed for the electrocatalytic activity for HER and OER, as well as the reaction kinetics.

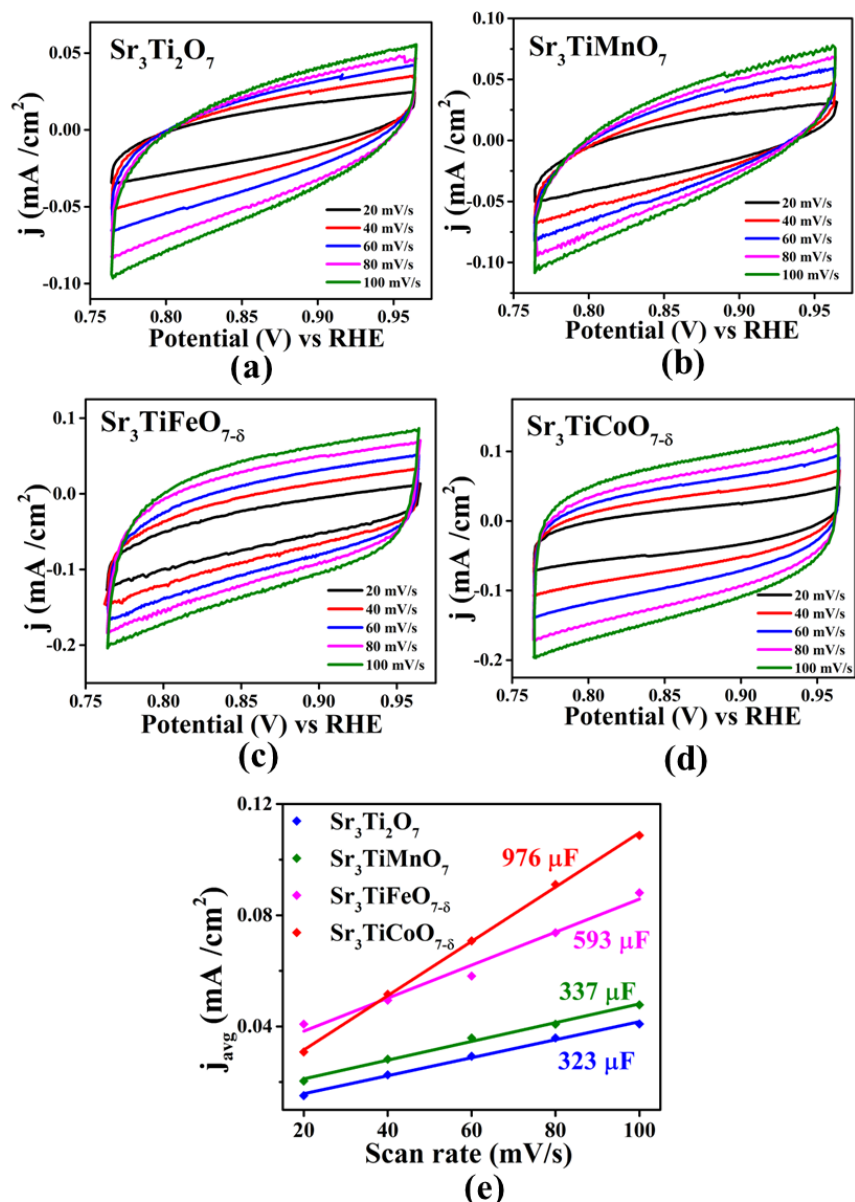


Figure 4.6: (a), (b), (c), and (d) cyclic voltammetry in non-Faradaic region in 0.1 M KOH. (e) j_{average} obtained from these CV plotted as a function of scan rate.

The active sites for oxide catalysts are often the metal sites.^{23, 34, 127} Given that OER and HER mechanisms both involve electron transfer processes, the ability of the metal to change oxidation state during the electrochemical process will affect the catalytic activity.^{127, 128} This may be one of the reasons for better catalytic activities of $\text{Sr}_3\text{TiMnO}_7$,

$\text{Sr}_3\text{TiFeO}_{7-\delta}$, and $\text{Sr}_3\text{TiCoO}_{7-\delta}$ compared to $\text{Sr}_3\text{Ti}_2\text{O}_7$. The two compounds, $\text{Sr}_3\text{TiCoO}_{7-\delta}$ and $\text{Sr}_3\text{TiFeO}_{7-\delta}$, which have better catalytic activities than the rest of the series, were found to contain oxygen-vacancies by iodometric titrations, with $\text{Sr}_3\text{TiCoO}_{7-\delta}$ showing the highest concentration of oxygen-vacancies ($\delta = 0.38$). Some previous studies on perovskite oxide electrocatalysts have indicated that oxygen vacancies can enhance the OER by increasing the adsorption energy of the reaction intermediates.¹²⁹ In some cases, oxygen vacancies may also lead to structural changes, which can enhance the electrocatalytic properties.⁹⁹ However, a number of other parameters may also have an impact on the electrocatalytic activity.^{120-122, 128, 130} The electronegativity of the B-site is one of the descriptors studied before.^{118, 119} The higher electronegativity of Co relative to Fe, Mn and Ti, results in a decrease in the energy of the metal-to-ligand charge-transfer,^{118, 119} and an increase in bond covalency between the metal and oxygen,¹²⁰ which can contribute to the improved electrocatalytic properties of $\text{Sr}_3\text{TiCoO}_{7-\delta}$ compared to the other materials in this series. Some other descriptors studied before are the number of 3d electrons¹³⁰ and the e_g orbital occupancy.¹²¹ Some studies have suggested that the e_g orbital occupancy of 1 is optimum for enhancing the electrocatalytic properties.^{23, 34, 122} The presence of oxygen-vacancies in $\text{Sr}_3\text{TiCoO}_{7-\delta}$ and $\text{Sr}_3\text{TiFeO}_{7-\delta}$ indicates partial reduction of the transition metals into the trivalent state. While Fe^{3+} in oxides is often in high-spin state ($t_{2g}^3 e_g^2$),¹³¹ an intermediate spin state has been suggested for Co^{3+} ($t_{2g}^5 e_g^1$),^{122, 123} which contains one electron in e_g orbitals. Finally, a correlation between the electrical conductivity and electrocatalytic activity has been suggested before.^{51, 62} For the materials studied in this work, the trend in electrical conductivity matches that of the electrocatalytic performance, where $\text{Sr}_3\text{TiCoO}_{7-\delta}$ has the highest electrical charge transport and best catalytic activity.

4.3 CONCLUSIONS

The trends in electrocatalytic activities of the Ruddlesden-Popper oxides studied in this work indicate the impact of several parameters on catalytic properties. The most active material in the series, $\text{Sr}_3\text{TiCoO}_{7-\delta}$, which shows the best catalytic performance for both HER and OER, also exhibits the highest electrical conductivity. In addition, it has the largest concentration of oxygen-vacancies in the series. The oxygen-vacancies lead to the reduction of metal ions, creating cations that have an optimum e_g electron occupancy for electrocatalytic activity. Furthermore, the higher electronegativity of cobalt, compared to Fe, Mn and Ti, leads to enhanced bond covalency between the metal and oxygen, which can enhance the electrocatalytic properties.

CHAPTER 5

STRUCTURE EFFECT ON PSEUDOCAPACITIVE PROPERTIES OF $A_2\text{LaMn}_2\text{O}_7$ ($A = \text{Ca, Sr}$)⁴

5.1 EXPERIMENTAL

5.1.1 SYNTHESIS

$\text{Ca}_2\text{LaMn}_2\text{O}_7$ and $\text{Sr}_2\text{LaMn}_2\text{O}_7$ were synthesized by solid-state synthesis method. Powders of CaCO_3 , SrCO_3 , La_2O_3 , and MnO_2 were used as precursors. Using an agate mortar and pestle, stoichiometric amounts of oxides and carbonates were thoroughly mixed before being pelletized. The samples were first calcined in air at 1300°C for 24 hours. This process was repeated three more times, by grinding, pelletization and heating for a total of 96 hours, until pure products were obtained. The intermediate products before refiring contained impurities, indicated by small peaks in the X-ray diffraction data. The re-pelletization and refiring helped to obtain pure products. The rate of heating and cooling of the furnace for all samples was $100^\circ\text{C}/\text{hour}$.

5.1.2 CHARACTERIZATION

The synthesized materials were characterized using a high-resolution X-ray diffractometer (Cu $K\alpha_1$, $\lambda = 1.54056 \text{ \AA}$). Rietveld refinements for the X-ray diffraction data were carried

⁴ The work described in this chapter was published in Energy Technol. 2023, 2201249.

out using GSAS software⁷⁶ and the EXPGUI interface.⁷⁷ The oxygen stoichiometry of the materials were determined by iodometric titration.

5.1.3 PSEUDOCAPACITANCE MEASUREMENTS

The catalyst ink for each sample was prepared by mixing 35 mg of the powdered sample, 7 mg of carbon black powder, 40 μL Nafion® D-521 solution (Alfa Aesar, 5% w/w in water and 1-propanol) with 7 ml of tetrahydrofuran. The mixture was then sonicated for 30 minutes. In three-electrode tests, the working electrode was the catalyst ink loaded on a glassy carbon electrode (GCE). Prior to use, the glassy carbon electrode (5 mm diameter, 0.196 cm^2 area) was furnished with aluminum oxide polishing slurry on a polishing cloth and sonicated for 2-3 minutes in ethanol. At the end of the polishing steps, GCE was washed with deionized water before being used. From the catalyst ink, two coatings of 10 μl were placed on the GCE, with a 2-minute interval, followed by overnight drying in air. The three-electrode pseudocapacitance measurements were performed in a standard three-electrode cell using a rotating disk electrode at 1600 rpm. The reference and counter electrodes were Ag/AgCl (in 3 M NaCl) and platinum, respectively.

The two-electrode cell for galvanostatic charge-discharge (GCD) measurements were done using two 1 cm^2 nickel foam pieces. From the above catalyst ink, 100 μl were dropcasted with 20 μl increments onto each of the two pieces of nickel foam, followed by overnight air-drying. The total mass of the active material for both electrodes was 1 mg. To separate the two electrodes, two layers of glass fiber filter paper were placed in between. The nickel foam electrodes were connected to the potentiostat using gold wires. Before performing

the GCD measurements and stability tests, the cell was placed in 1 M KOH to soak for at least 12 hours.

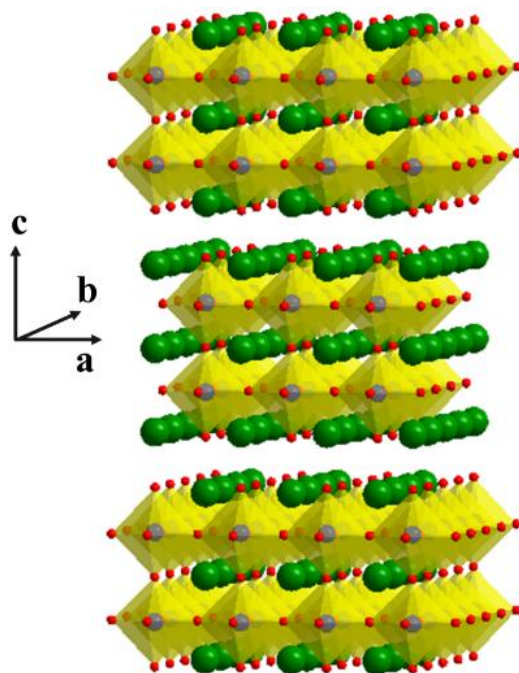


Figure 5.1: Typical crystal structure of a bilayered Ruddlesden-Popper oxide. In the case of $\text{Ca}_2\text{LaMn}_2\text{O}_7$ and $\text{Sr}_2\text{LaMn}_2\text{O}_7$, the yellow octahedra are MnO_6 units, green spheres represent the sites where La/Ca/Sr reside, and red spheres indicate oxygen.

5.2 RESULTS AND DISCUSSION

The crystal structures of both materials comprise bilayer stacks of MnO_6 octahedra, as shown in **Figure 5.1**. The La^{3+} , Ca^{2+} , and Sr^{2+} ions are located in vacant spaces among the above octahedra, both within the between the stacks. However, the difference in the ionic radii of Ca^{2+} and Sr^{2+} leads to a change in symmetry. While $\text{Ca}_2\text{LaMn}_2\text{O}_7$ ⁸⁸ has an orthorhombic *Cmcm* space group, $\text{Sr}_2\text{LaMn}_2\text{O}_7$ ⁸⁹ crystalizes in a tetragonal *I4/mmm* space group, as also reported previously.^{88, 89} **Figure 5.2** and **Tables 5.1-5.2** show the Rietveld refined profiles and refined structural parameters for both materials.

Cyclic voltammetry (CV) data for both materials are shown in **Figure 5.3**. The CVs were obtained in the potential window of -1.0 V to +0.6 V at scan rates of 5, 10, 25, 50 and 100 mV/s in 1 M KOH. The quasi-rectangular shape and redox peaks in the CVs indicate the pseudocapacitive characteristics and faradaic processes, respectively.⁷⁰ These redox peaks are more apparent at higher scan rates. These peaks can be attributed to $\text{Mn}^{2+} \leftrightarrow \text{Mn}^{3+}$ and $\text{Mn}^{3+} \leftrightarrow \text{Mn}^{4+}$ surface redox reactions.

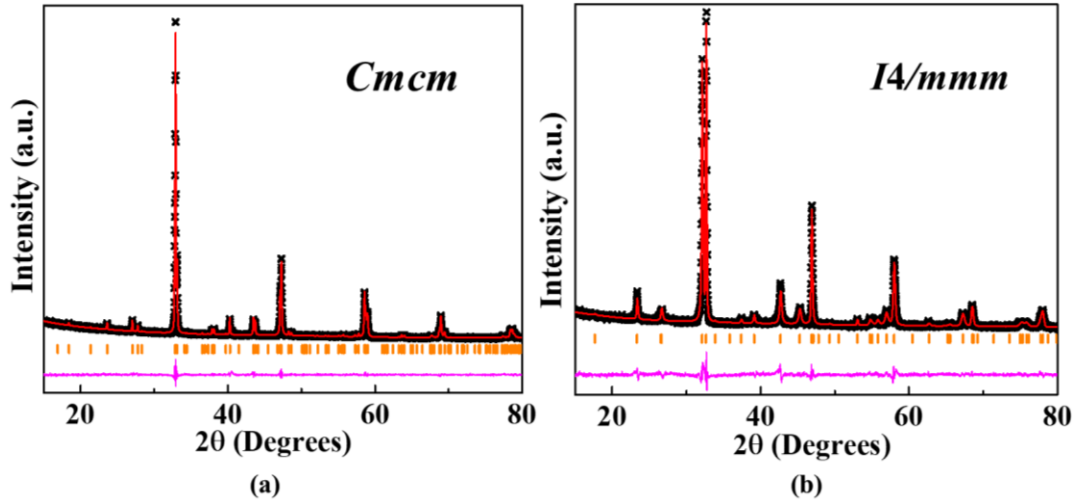


Figure 5.2: Powder X-ray diffraction data for (a) $\text{Ca}_2\text{LaMn}_2\text{O}_7$ and (b) $\text{Sr}_2\text{LaMn}_2\text{O}_7$. Black crosses, orange vertical tick marks, solid red line, and lower pink line correspond to experimental data, Bragg peak positions, the model, and difference plot, respectively.

Table 5.1: Refined structural parameters $\text{Ca}_2\text{LaMn}_2\text{O}_7$ from powder X-ray diffraction data. Space group: *Cmcm*, $a = 19.2820(5)$ Å, $b = 5.4614(1)$ Å, $c = 5.4116(2)$ Å, $R_p = 0.0259$, $wR_p = 0.0335$

Atom	x	y	z	Occupancy	$U_{\text{iso}} (\text{Å}^2)$	Multiplicity
Ca1	0	0.2504(25)	0.25	0.385(11)	0.0196(28)	4
La1	0	0.2504(25)	0.25	0.615(11)	0.0196(28)	4
Ca2	0.18869(30)	0.2425(22)	0.25	0.773(8)	0.0506(28)	8
La2	0.18869(30)	0.2425(22)	0.25	0.227(8)	0.0506(28)	8

Mn	0.3995(4)	0.2429(32)	0.25	1	0.015(4)	8
O1	0	0.690(9)	0.25	1	0.017(5)	4
O2	0.3023(13)	0.294(6)	0.25	1	0.017(5)	8
O3	0.0947(15)	0	0	1	0.017(5)	8
O4	0.3937(14)	0	0	1	0.017(5)	8

Table 5.2: Refined structural parameters of Sr₂LaMn₂O₇ from powder X-ray diffraction data. Space group: *I4/mmm*, $a = b = 3.8668(1)$ Å, $c = 19.9801(10)$ Å, $R_p = 0.0419$, $wR_p = 0.0556$

Atom	x	y	z	Occupancy	U _{iso} (Å ²)	Multiplicity
Sr1	0	0	0.5	0.577(27)	0.0379(26)	2
La1	0	0	0.5	0.423(27)	0.0379(26)	2
Sr2	0	0	0.31553(15)	0.727(28)	0.0424(21)	4
La2	0	0	0.31553(15)	0.273(28)	0.0424(21)	4
Mn	0	0	0.1008(4)	1	0.0210(18)	4
O1	0	0	0	1	0.097(4)	2
O2	0	0	0.1950(13)	1	0.097(4)	4
O3	0	0.5	0.0974(12)	1	0.097(4)	8

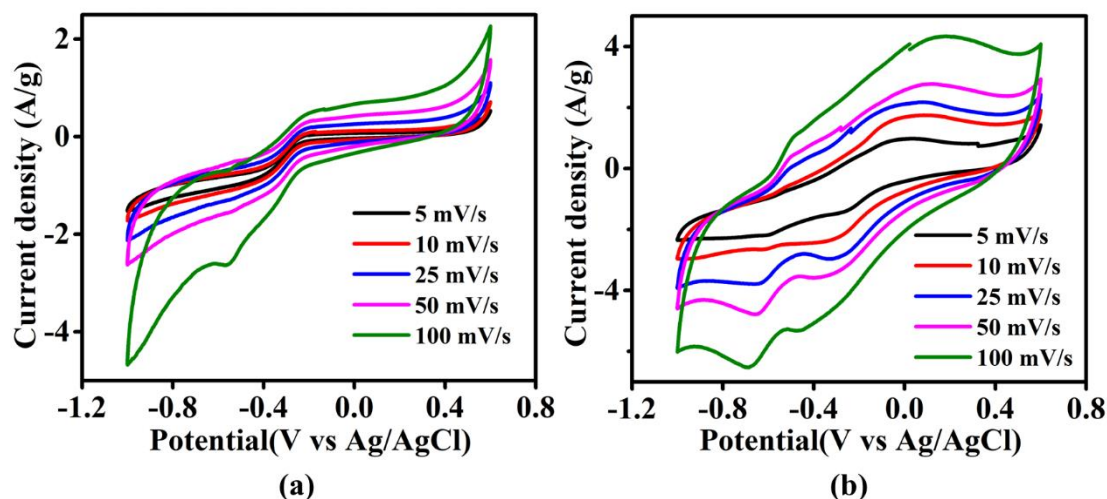


Figure 5.3: Cyclic voltammetry curves from three-electrode measurements for (a) $\text{Ca}_2\text{LaMn}_2\text{O}_7$ and (b) $\text{Sr}_2\text{LaMn}_2\text{O}_7$.

The data at 100 mV/s for $\text{Ca}_2\text{LaMn}_2\text{O}_7$ show a pair of redox peaks at about -0.55 V/-0.51 V, which can be ascribed to the $\text{Mn}^{2+} \leftrightarrow \text{Mn}^{3+}$ redox process. Another pair of peaks are present at ~ -0.35 V/-0.21 V, indicating the $\text{Mn}^{3+} \leftrightarrow \text{Mn}^{4+}$ surface redox reaction. For $\text{Sr}_2\text{LaMn}_2\text{O}_7$, there is a pair of redox peaks at ~ -0.67 V/-0.50 V, indicating $\text{Mn}^{2+} \leftrightarrow \text{Mn}^{3+}$, as well as a less perceptible peak couple at ~ -0.45 V/0.10 V for $\text{Mn}^{3+} \leftrightarrow \text{Mn}^{4+}$.^{27, 70, 73}

The appearance of both anodic and cathodic peaks indicates the reversible redox process. As the scan rate increases, slight shifts of anodic and cathodic CV peaks are observable to the higher and lower potentials, respectively. These shifts are due to the internal resistance of the electrode and, further indicate that the limiting step in the process is charge transfer kinetics.^{132, 133} The peak current increase at higher scan rates indicates the rapid electronic and ionic transport rates.^{133, 134} Moreover, the enhanced mass transport and electron conduction are indicated by the increase in the area of the CV as a function of scan rate, while the shape of the cyclic voltammogram is retained.¹³²⁻¹³⁴

The electrochemical redox process is associated with oxygen ion intercalation into the perovskite system in alkaline medium, as was first observed for $\text{Nd}_{1-x}\text{Sr}_x\text{CoO}_3$,¹³⁵ followed by later studies on other perovskite-type oxides.^{22, 27, 73} This leads to pseudocapacitive properties, where oxygen ions that are intercalated into the oxygen vacancies originate from OH^- in the electrolyte. The OH^- ions lose a proton to another OH^- ion to form an H_2O molecule, leaving behind the O^{2-} ion to intercalate into the material, as described for other perovskite oxides.^{71, 134} The OH^- ion intercalation was confirmed by conducting cyclic voltammetry experiments in both KOH and KNO_3 electrolytes in the same potential window, as shown in **Figure 5.4**. The lack of redox peaks in the CVs in KNO_3 indicates that the redox reactions are facilitated by the intercalation processes that rely on hydroxide ions of KOH.⁷⁰

Galvanostatic charge-discharge (GCD) curves were obtained at different current densities of 0.5, 1, 3, 5, and 10 A/g, using a symmetric two-electrode cell fabricated according to the procedure described in the experimental section. The GCD curves are illustrated in **Figure 5.5**.

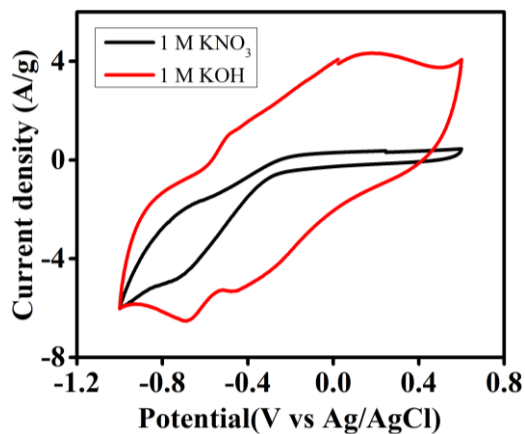


Figure 5.4: Cyclic voltammetry curves from three-electrode measurements in 1M KNO_3 and 1M KOH electrolytes at 100 mV/s for $\text{Sr}_2\text{LaMn}_2\text{O}_7$, which has greater pseudocapacitive properties.

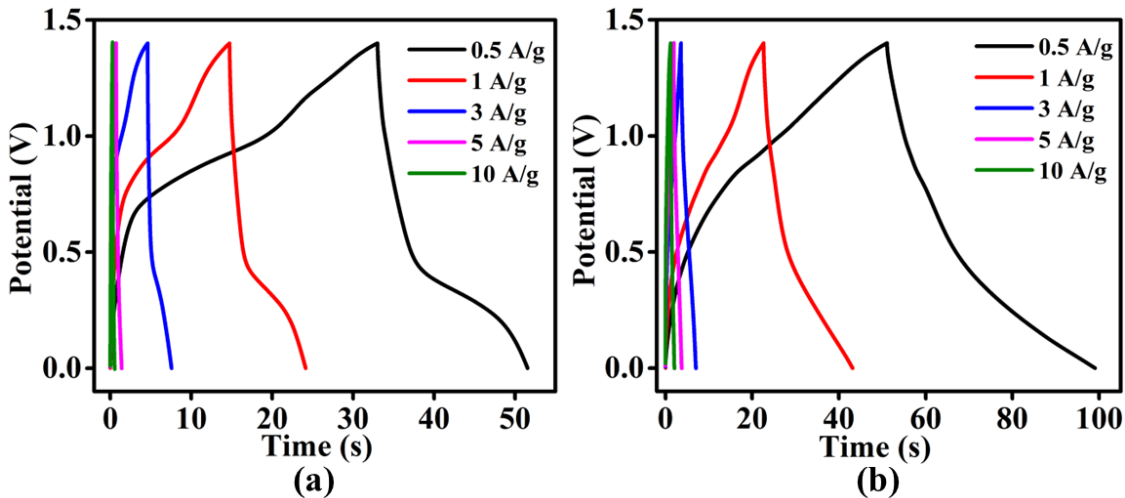


Figure 5.5: Galvanostatic charge-discharge (GCD) profiles using a two-electrode cell for (a) $\text{Ca}_2\text{LaMn}_2\text{O}_7$ and (b) $\text{Sr}_2\text{LaMn}_2\text{O}_7$.

The inverted V shape of the cycles are indicative of the pseudocapacitive behavior of the materials.⁶⁹ Equation (1) can be used to calculate the specific capacitance using the GCD data at different current densities where m is the total mass of the active material in both the electrodes, I is the constant current applied in the GCD measurement, ΔV is the potential window, and Δt is the discharge time.¹³⁶

$$C_s = \frac{4I\Delta t}{m\Delta V} \quad (1)$$

Internal resistance of the electrode limits the utilization of the pseudocapacitive material, thereby causing a decrease in the specific capacitance with increasing current density, as evident from **Figure 5.6**.⁶⁹

The specific capacitance values at 0.5 A/g in 1 M KOH are 13.2 F/g for $\text{Ca}_2\text{LaMn}_2\text{O}_7$ and 34.265 F/g for $\text{Sr}_2\text{LaMn}_2\text{O}_7$. We note that iodometric titrations show that both of these

materials have stoichiometric formulas, with 7 oxygens per formula unit. Therefore, the oxygen intercalation might occur into interstitial spaces within the material lattice. In such situation, the larger ionic radius of Sr^{2+} compared to that of Ca^{2+} , may lead to wider interstitial spaces, allowing better intercalation of oxygen. For example, the separation between Mn sites in adjacent stacks are 6.38 (2) Å for $\text{Ca}_2\text{LaMn}_2\text{O}_7$ and 6.56 (1) Å for $\text{Sr}_2\text{LaMn}_2\text{O}_7$. The enhanced intercalation results in the observation of a greater specific capacitance for $\text{Sr}_2\text{LaMn}_2\text{O}_7$. Furthermore, the orthorhombic structure of $\text{Ca}_2\text{LaMn}_2\text{O}_7$ features more distortions than the tetragonal structure of $\text{Sr}_2\text{LaMn}_2\text{O}_7$. The latter may be able to accommodate more oxygen intercalation through lattice distortion, whereas the former already has a substantial degree of distortion in the structure. The C_s for the latter is significantly larger than those of some of the reported perovskites, such as 13 F/g for $\text{La}_{1-x}\text{Ca}_x\text{MnO}_3$ ¹³⁷ and 7.75 F/g for $\text{La}_{1-x}\text{Sr}_x\text{MnO}_3$,⁶⁹ at 0.5 A/g current density.

The energy densities (E) of these pseudocapacitors can be calculated using equation (2), where C_s is the specific capacitance obtained from the two electrode cell and V is the potential window.¹³⁸

$$E = \frac{C_s V^2}{2 \times 3.6} \quad (2)$$

The multiplier 1/3.6 is used to calculate the energy density in Wh/kg, where the C_s has the unit F/g. It should mention that $1\text{F} = \frac{1\text{ s.A}}{\text{V}}$ and $1\text{ W} = 1\text{ V} \times 1\text{ A}$. In some previous studies, the multipliers were not shown in the energy density formula, $E = C_s \cdot V^2/2$.^{70, 129, 139, 140} It is assumed that those studies utilized multipliers separately to achieve the appropriate units. The energy density obtained from equation (2) can then be used to calculate the power

density using equation (3), shown below, where the multiplier 3600 is needed to express the power density in W/kg.

$$P = \frac{E \times 3600}{\Delta t} \quad (3)$$

Using these equations, the energy density of 3.59 Wh/kg and power density of 700 W/kg is obtained for $\text{Ca}_2\text{LaMn}_2\text{O}_7$ based on GCD experiments at the applied current density of 0.5 A/g. On the other hand, $\text{Sr}_2\text{LaMn}_2\text{O}_7$ shows an energy density of 9.33 Wh/kg and power density of 700 W/kg at 0.5 A/g. For comparison, an energy density of ~ 7.6 Wh/kg and a power density of 160 W/kg are reported for $\text{La}_{1-x}\text{Ca}_x\text{MnO}_3$ at 0.5 A/g current density.¹³⁷ Also, $\text{La}_{1-x}\text{Sr}_x\text{MnO}_3$ gives an energy density of ~ 3.6 Wh/kg and a power density of 120 W/kg at 0.5 A/g.⁶⁹

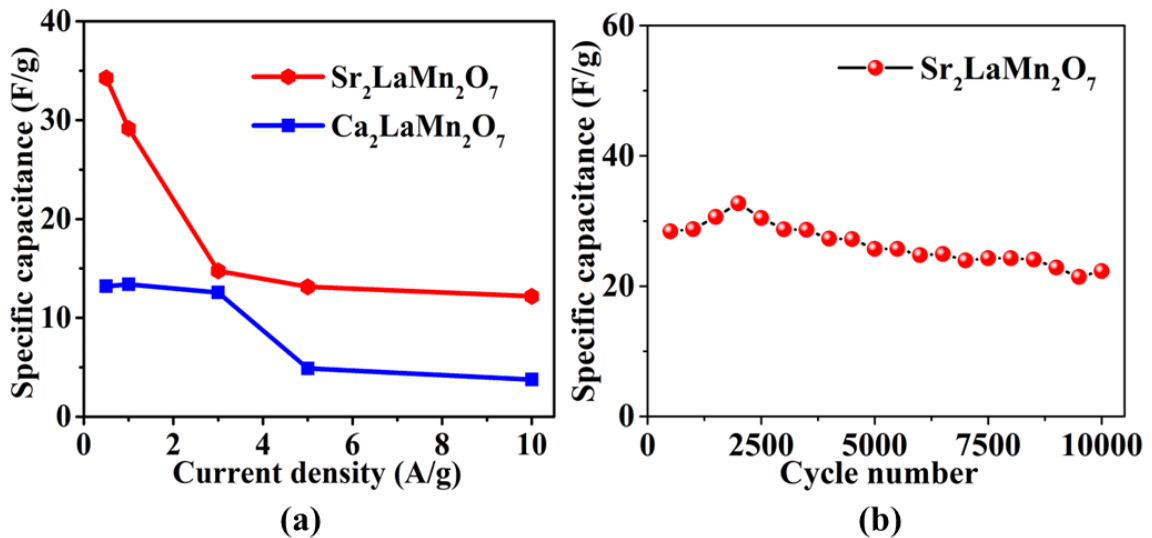


Figure 5.6: (a) Specific capacitance at different current densities. (b) Stability test at current density of 1 A/g for $\text{Sr}_2\text{LaMn}_2\text{O}_7$.

The stability of the best performing material $\text{Sr}_2\text{LaMn}_2\text{O}_7$, was also studied by performing 10,000 GCD cycles at a current density of 1 A/g. The specific capacitance at every 500

cycles is shown in Figure 6b. The specific capacitance of $\text{Sr}_2\text{LaMn}_2\text{O}_7$, shows only a small change after 10,000 cycles, indicating the high stability.

In summary, the effect of structure on pseudocapacitive properties is significant, given that the two materials studied here are isoelectronic, and only differ in their structural features due to the difference in the ionic radii of Ca^{2+} and Sr^{2+} . These ions do not make a direct contribution to the near-surface faradaic processes that promote a pseudocapacitive behavior. Instead, they modify the structure and symmetry of the lattice, which can affect the oxygen intercalation and the associated faradaic reactions.

CHAPTER 6

CONCLUSION

Oxide materials derived from perovskites have been studied for a wide range of applications, such as solar cells, batteries, superconductors, catalysts, and capacitors. Ruddlesden-Popper (RP) structure, with the general formula $A_3B_2O_7$, is a perovskite-derived oxide, comprising bilayer stacks of BO_6 octahedra, where A occupy the spaces within and between the stacks.

The impact of structural symmetry on electrical charge transport, magnetism and electrocatalytic activity has been investigated in isoelectronic bilayer RP materials $Ca_2LaMn_2O_7$ and $Sr_2LaMn_2O_7$ by changing the A-site cations. The change in ionic radius from Ca^{2+} (1.18 Å) to Sr^{2+} (1.31 Å) results in a change in structural symmetry in these systems. $Ca_2LaMn_2O_7$ has an orthorhombic structure with $Cmcm$ space group, whereas $Sr_2LaMn_2O_7$ features a tetragonal, $I4/mmm$, structure. The higher symmetry results in a significant variation of electrical, magnetic and electrocatalytic properties. $Sr_2LaMn_2O_7$ shows significantly greater charge transport in the entire temperature range of 25-800 °C, owing to a larger angle of Mn–O–Mn conduction pathway. In addition, the electrocatalytic properties of $Sr_2LaMn_2O_7$ for the two half-reactions of water-splitting, i.e., hydrogen-evolution reaction (HER) and oxygen-evolution reaction (OER) are enhanced as compared to $Ca_2LaMn_2O_7$. The improved OER/HER activity is also a function of structural features

that produce greater electrical conductivity, which in turn affects the electrocatalytic properties.

Our next strategy was to study the effect of the electronic configuration of transition metal on electrocatalytic activity, charge transport, and magnetic properties in $\text{Sr}_2\text{LaFeMnO}_7$ and $\text{Sr}_2\text{LaCoMnO}_7$ via changing the B-site cations. The two compounds are isostructural. Despite their structural similarity, the magnetic transition temperature of $\text{Sr}_2\text{LaCoMnO}_7$ is significantly lower than that of $\text{Sr}_2\text{LaFeMnO}_7$. The electrical charge-transport properties are also different, where $\text{Sr}_2\text{LaCoMnO}_7$ shows considerably improved electrical conductivity. Importantly, the electrocatalytic activities for the two half-reactions of water-splitting, are improved in $\text{Sr}_2\text{LaCoMnO}_7$ compared to $\text{Sr}_2\text{LaFeMnO}_7$. The trends in electrical charge transport, HER and OER activity, and kinetics for OER and HER are all similar, indicating the improved properties of $\text{Sr}_2\text{LaCoMnO}_7$. These changes are explained in the context of a greater bond covalency in this material due to the higher electronegativity of Co, which results in better overlap between the transition metal d orbital and oxygen p orbital. The relation between the electrocatalytic performance and the optimum eg orbital occupancy in $\text{Sr}_2\text{LaCoMnO}_7$ is also discussed.

In the next approach the correlation of the electrocatalytic activity with electrical conductivity, oxygen-vacancies, and electronegativity have been studied in a series of isostructural oxides, $\text{Sr}_3\text{Ti}_{2-x}\text{M}_x\text{O}_{7-\delta}$ ($M = \text{Mn, Fe, Co; } x = 0, 1$). They show a systematic increase in electrocatalytic activity in progression from $\text{Sr}_3\text{Ti}_2\text{O}_7$ to $\text{Sr}_3\text{TiMnO}_7$, $\text{Sr}_3\text{TiFeO}_{7-\delta}$, and $\text{Sr}_3\text{TiCoO}_{7-\delta}$. The kinetic studies using Tafel method indicate the same trend across the series, where the best catalyst also has the fastest kinetics for both HER and OER. Also, the same progression is observed in the concentration of oxygen-vacancies,

as well as the electrical conductivity in a wide range of temperatures, 25 °C – 800 °C. The material that shows the best electrocatalytic activity, i.e., $\text{Sr}_3\text{TiCoO}_{7-\delta}$, also has the highest electrical conductivity and the greatest concentration of oxygen-vacancies in the series. The correlations observed in this work indicate that trends in electrocatalytic performance may be related to the systematic increase in electrical conductivity, electronegativity, and oxygen-vacancies, as well as the electron occupancy of e_g orbitals, which can affect the strength of sigma interactions between the catalyst and reaction intermediates.

Bilayered RP materials were further explored to understand oxide intercalation-based pseudocapacitance. The effect of structure on pseudocapacitive properties in alkaline conditions is demonstrated through the investigation of isoelectronic oxides $\text{Ca}_2\text{LaMn}_2\text{O}_7$ and $\text{Sr}_2\text{LaMn}_2\text{O}_7$, where the difference in ionic radii of Ca^{2+} and Sr^{2+} leads to a change in structure and lattice symmetry as described in Chapter 2. While calcium and strontium do not make a direct contribution to the near-surface faradaic processes that are essential to the pseudocapacitive properties, their effect on the structure leads to a change in the oxygen intercalation process and the associated pseudocapacitive energy storage. We have shown that $\text{Sr}_2\text{LaMn}_2\text{O}_7$ has a significantly greater specific capacitance than $\text{Ca}_2\text{LaMn}_2\text{O}_7$. In addition, the former shows a considerably higher energy density compared to the latter. Furthermore, these materials show highly stable energy storage properties, and retain their specific capacitance over 10000 cycles of charge-discharge in a symmetric pseudocapacitive cell. Importantly, these findings show the structure-property relationships, where a change in the structure and lattice symmetry can result in a significant change in pseudocapacitive charge-discharge properties in isoelectronic systems.

Overall, this study has emphasized that bilayered RP oxides show versatile properties such as magnetism, electrical charge transport, pseudocapacitance, and electrocatalysis. The structure, symmetry, and oxygen vacancies in the bilayered RP oxides can be changed to modify the above-mentioned properties. There is much room in the structure of the bilayered RP oxides to tune the physical and chemical properties for various energy-related applications, including water splitting and energy storage.

REFERENCES

- (1) Fanah, S. J.; Ramezanipour, F. Lithium-ion mobility in layered oxides $\text{Li}_2\text{Ca}_{1.5}\text{Nb}_3\text{O}_{10}$, $\text{Li}_2\text{Ca}_{1.5}\text{TaNb}_2\text{O}_{10}$ and $\text{Li}_2\text{Ca}_{1.5}\text{Ta}_2\text{NbO}_{10}$, enhanced by supercell formation. *J. Energy Chem.* **2021**, *60*, 75-84.
- (2) Fanah, S. J.; Ramezanipour, F. Symmetry Effect on the Enhancement of Lithium-Ion Mobility in Layered Oxides $\text{Li}_2\text{A}_2\text{B}_2\text{TiO}_{10}$ (A = La, Sr, Ca; B = Ti, Ta). *J. Phys. Chem. C* **2021**, *125* (7), 3689-3697.
- (3) Fanah, S. J.; Yu, M.; Huq, A.; Ramezanipour, F. Insight into lithium-ion mobility in $\text{Li}_2\text{La}(\text{TaTi})\text{O}_7$. *J. Mater. Chem. A* . **2018**, *6* (44), 22152-22160.
- (4) Lun-hua, H.; Pan-lin, Z.; Qi-wei, Y. The structure and magnetic properties of $\text{La}_{2-2x}\text{Sr}_1\text{Ca}_{2x}\text{Mn}_2\text{O}_7$ ($x = 0.25-1.00$). *Chin. Phys* **2001**, *10* (9), 857-861.
- (5) Suryanarayanan, R.; Dhahenne, G.; Revcolevschi, A.; Prellier, W.; Renard, J. P.; Dupas, C.; Caliebe, W.; Chatterji, T. Colossal magnetoresistance and re-entrant charge ordering in single crystalline two layer Mn perovskite $\text{LaSr}_2\text{Mn}_2\text{O}_7$. *Solid State Commun.* **1999**, *113* (5), 267-271.
- (6) Gupta, A. K.; Bhalla, G. L.; Khare, N. Magnetic phase diagram of double-layered $\text{La}_{2-2x}\text{Ca}_{1+2x}\text{Mn}_2\text{O}_7$ manganite. *J Phys Chem Solids* **2006**, *67* (11), 2358-2364.
- (7) Fanah, S. J.; Ramezanipour, F. Lithium-Ion Mobility in Layered Oxide $\text{Li}_2(\text{La}_{0.75}\text{Li}_{0.25})(\text{Ta}_{1.5}\text{Ti}_{0.5})\text{O}_7$ Containing Lithium on both Intra and Inter-Stack Positions. *Eur. J. Inorg. Chem.* **2022**, *2022* (7), e202100950.
- (8) Fanah, S. J.; Ramezanipour, F. Strategies for Enhancing Lithium-Ion Conductivity of Triple-Layered Ruddlesden–Popper Oxides: Case Study of $\text{Li}_{2-x}\text{La}_{2-y}\text{Ti}_{3-z}\text{Nb}_z\text{O}_{10}$. *Inorg. Chem.* **2020**, *59* (14), 9718-9727.
- (9) Fanah, S. J.; Ramezanipour, F. Enhancing the lithium-ion conductivity in $\text{Li}_2\text{SrTa}_{2-x}\text{Nb}_x\text{O}_7$ ($x = 0-2$). *Solid State Sci.* **2019**, *97*, 106014.
- (10) Zhu, Y.; Tahini, H. A.; Hu, Z.; Dai, J.; Chen, Y.; Sun, H.; Zhou, W.; Liu, M.; Smith, S. C.; Wang, H.; et al. Unusual synergistic effect in layered Ruddlesden–Popper oxide enables ultrafast hydrogen evolution. *Nat. Commun.* **2019**, *10* (1), 149.
- (11) Yin, B.; Li, Y.; Sun, N.; Ji, X.; Huan, Y.; Dong, D.; Hu, X.; Wei, T. Activating ORR and OER in Ruddlesden-Popper based catalysts by enhancing interstitial oxygen and lattice oxygen redox reactions. *Electrochim. Acta* **2021**, *370*, 137747.
- (12) Yattoo, M. A.; Du, Z.; Yang, Z.; Zhao, H.; Skinner, S. J. $\text{La}_x\text{Pr}_{4-x}\text{Ni}_3\text{O}_{10-\delta}$: Mixed A-Site Cation Higher-Order Ruddlesden-Popper Phase Materials as Intermediate-Temperature Solid Oxide Fuel Cell Cathodes. *Crystals* **2020**, *10*, 428.
- (13) Wang, Q.; Hou, J.; Fan, Y.; Xi, X.-a.; Li, J.; Lu, Y.; Huo, G.; Shao, L.; Fu, X.-Z.; Luo, J.-L. $\text{Pr}_2\text{BaNiMnO}_{7-\delta}$ double-layered Ruddlesden–Popper perovskite oxides as efficient cathode electrocatalysts for low temperature proton conducting solid oxide fuel cells. *J. Mater. Chem. A* . **2020**, *8* (16), 7704-7712.
- (14) Fanah, S. J.; Yu, M.; Ramezanipour, F. Experimental and theoretical investigation of lithium-ion conductivity in $\text{Li}_2\text{LaNbTiO}_7$. *Dalton Trans.* **2019**, *48* (46), 17281-17290.

- (15) Huan, D.; Wang, Z.; Wang, Z.; Peng, R.; Xia, C.; Lu, Y. High-Performanced Cathode with a Two-Layered R–P Structure for Intermediate Temperature Solid Oxide Fuel Cells. *ACS Appl. Mater. Interfaces* **2016**, *8* (7), 4592-4599.
- (16) Assirey, E. A. R. Perovskite synthesis, properties and their related biochemical and industrial application. *SPJ* **2019**, *27* (6), 817-829.
- (17) Kostopoulou, A.; Brintakis, K.; Nasikas, N. K.; Stratakis, E. Perovskite nanocrystals for energy conversion and storage. *Nanophotonics* **2019**, *8* (10), 1607-1640.
- (18) Kananke-Gamage, C. C. W.; Ramezanipour, F. Structure Effect on Pseudocapacitive Properties of $A_2LaMn_2O_7$ (A = Ca, Sr). *Energy Technol.* **2023**, 2201249.
- (19) Navrotsky, A. Energetics and Crystal Chemical Systematics among Ilmenite, Lithium Niobate, and Perovskite Structures. *Chem. Mater.* **1998**, *10* (10), 2787-2793.
- (20) Sun, C.; Alonso, J. A.; Bian, J. Recent Advances in Perovskite-Type Oxides for Energy Conversion and Storage Applications. *Adv. Energy Mater.* **2021**, *11* (2), 2000459.
- (21) Ruddlesden, S. N.; Popper, P. The compound $Sr_3Ti_2O_7$ and its structure. *Acta Crystallographica* **1958**, *11* (1), 54-55.
- (22) Alom, M. S.; Ramezanipour, F. Pseudocapacitive charge storage in layered oxides $SrLaFe_{1-x}Co_xO_{4-\delta}$ (x = 0–1). *Mater. Lett.* **2021**, 295, 129859.
- (23) Alom, M. S.; Kananke-Gamage, C. C. W.; Ramezanipour, F. Perovskite Oxides as Electrocatalysts for Hydrogen Evolution Reaction. *ACS Omega* **2022**, *7* (9), 7444-7451.
- (24) Kubicek, M.; Bork, A. H.; Rupp, J. L. M. Perovskite oxides – a review on a versatile material class for solar-to-fuel conversion processes. *J. Mater. Chem. A* **2017**, *5* (24), 11983-12000.
- (25) Hona, R. K.; Ramezanipour, F. Effect of the Oxygen Vacancies and Structural Order on the Oxygen Evolution Activity: A Case Study of $SrMnO_{3-\delta}$ Featuring Four Different Structure Types. *Inorg. Chem.* **2020**, *59* (7), 4685-4692.
- (26) Karki, S. B.; Hona, R. K.; Yu, M.; Ramezanipour, F. Enhancement of Electrocatalytic Activity as a Function of Structural Order in Perovskite Oxides. *ACS Catal.* **2022**, 10333-10337.
- (27) Karki, S. B.; Ramezanipour, F. Pseudocapacitive Energy Storage and Electrocatalytic Hydrogen-Evolution Activity of Defect-Ordered Perovskites $Sr_xCa_{3-x}GaMn_2O_8$ (x = 0 and 1). *ACS Appl. Energy Mater.* **2020**, *3* (11), 10983-10992.
- (28) Karki, S. B.; Hona, R. K.; Ramezanipour, F. Effect of Structure on Sensor Properties of Oxygen-Deficient Perovskites, $A_2BB'O_5$ (A = Ca, Sr; B = Fe; B' = Fe, Mn) for Oxygen, Carbon Dioxide and Carbon Monoxide Sensing. *J. Electron. Mater.* **2020**, *49* (2), 1557-1567.
- (29) Chen, A.; Zhang, X.; Zhang, Z.; Yao, S.; Zhou, Z. Band engineering of two-dimensional Ruddlesden–Popper perovskites for solar utilization: the relationship between chemical components and electronic properties. *J. Mater. Chem. A* **2019**, *7* (18), 11530-11536.
- (30) Mulmi, S.; Hona, R. K.; Jasinski, J. B.; Ramezanipour, F. Electrical conductivity of $Sr_{2-x}Ca_xFeMnO_5$ (x = 0, 1, 2). *J Solid State Electrochem* **2018**, *22* (8), 2329-2338.
- (31) Anjum, M. A. R.; Okyay, M. S.; Kim, M.; Lee, M. H.; Park, N.; Lee, J. S. Bifunctional sulfur-doped cobalt phosphide electrocatalyst outperforms all-noble-metal electrocatalysts in alkaline electrolyzer for overall water splitting. *Nano Energy* **2018**, *53*, 286-295.
- (32) Hona, R. K.; Ramezanipour, F. Enhanced electrical properties in $BaSrFe_2O_{6-\delta}$ ($\delta = 0.5$): A disordered defect-perovskite. *Polyhedron* **2019**, *167*, 69-74.

- (33) Karki, S. B.; Ramezanipour, F. Magnetic and electrical properties of BaSrMMoO₆ (M = Mn, Fe, Co, and Ni). *Mater. Today Chem.* **2019**, *13*, 25-33.
- (34) Alom, M. S.; Ramezanipour, F. Layered Oxides SrLaFe_{1-x}Co_xO_{4-δ} (x=0–1) as Bifunctional Electrocatalysts for Water-Splitting. *ChemCatChem* **2021**, *13* (15), 3510-3516.
- (35) Avci, Ö. N.; Sementa, L.; Fortunelli, A. Mechanisms of the Oxygen Evolution Reaction on NiFe₂O₄ and CoFe₂O₄ Inverse-Spinel Oxides. *ACS Catal.* **2022**, *12* (15), 9058-9073.
- (36) Sowjanya, C.; Mandal, R.; Abhinay, S.; Mohanta, A.; Das, S.; Pratihari, S. K. Effect of B-site substitution on the crystal structure, electrical conductivity and oxygen transport properties of La_{0.5}Sr_{0.5}M_{0.2}Fe_{0.8}O_{3-δ} (M = Co, Al, and Zn) perovskite. *J. Solid State Chem.* **2020**, *285*, 121237.
- (37) Park, J.; Lee, E.; Lee, K. W.; Lee, C. E. Electrical transport and quasipersistent photocurrent in vanadium oxide nanowire networks. *Appl. Phys. Lett.* **2006**, *89* (18), 183114.
- (38) Han, N.; Shen, Z.; Zhao, X.; Chen, R.; Thakur, V. K. Perovskite oxides for oxygen transport: Chemistry and material horizons. *Sci. Total Environ.* **2022**, *806*, 151213.
- (39) Ding, P.; Li, W.; Zhao, H.; Wu, C.; Zhao, L.; Dong, B.; Wang, S. Review on Ruddlesden–Popper perovskites as cathode for solid oxide fuel cells. *J Phys Materials* **2021**, *4* (2), 022002.
- (40) Chronopoulos, A.; Parfitt, D.; Kilner, J. A.; Grimes, R. W. Anisotropic oxygen diffusion in tetragonal La₂NiO_{4+δ}: molecular dynamics calculations. *J. Mater. Chem. A* **2010**, *20* (2), 266-270.
- (41) Sun, R.; Qin, X.-y.; Li, L. L.; Li, D.-D.; Zhang, J.; Wang, Q. Transport and thermoelectric properties of n-type Ruddlesden–Popper phase (Sr_{1-x}Gd_x)₃(Ti_{1-y}Ta_y)₂O₇ oxides. *J. Phys. D: Appl. Phys* **2012**, *45*, 415401.
- (42) Hona, R. K.; Ramezanipour, F. Disparity in electrical and magnetic properties of isostructural oxygen-deficient perovskites BaSrCo₂O_{6-δ} and BaSrCoFeO_{6-δ}. *J. Mater. Sci.: Mater. Electron.* **2018**, *29* (16), 13464-13473.
- (43) Kanaiwa, Y.; Wakeshima, M.; Hinatsu, Y. Synthesis, crystal structure, and magnetic properties of ordered perovskites Sr₂LnTaO₆ (Ln = lanthanides). *Mater. Res. Bull.* **2002**, *37* (11), 1825-1836.
- (44) Xia, H.; Dai, J.; Xu, Y.; Yin, Y.; Wang, X.; Liu, Z.; Liu, M.; McGuire, M. A.; Li, X.; Li, Z.; et al. Magnetism and the spin state in cubic perovskite CaCoO₃ synthesized under high pressure. *Physical Review Materials* **2017**, *1* (2), 024406.
- (45) Salak, A.; Cardoso, J. P.; Vieira, J.; Shvartsman, V.; Khalyavin, D.; Fertman, E.; Fedorchenko, A.; Pushkarev, A.; Radyush, Y.; Olekhovich, N.; et al. Magnetic Behaviour of Perovskite Compositions Derived from BiFeO₃. *Magnetochemistry* **2021**, *7*, 151.
- (46) Vasala, S.; Karppinen, M. A₂B'B''O₆ perovskites: A review. *Prog. Solid. State Ch.* **2015**, *43* (1), 1-36.
- (47) Jin, L.; Ni, D.; Gui, X.; Straus, D. B.; Zhang, Q.; Cava, R. J. Ferromagnetic Double Perovskite Semiconductors with Tunable Properties. *Adv. Sci.* **2022**, *9* (8), 2104319.
- (48) Gurusinghe, N. N. M.; de la Figuera, J.; Marco, J. F.; Thomas, M. F.; Berry, F. J.; Greaves, C. Synthesis and characterisation of the n=2 Ruddlesden–Popper phases Ln₂Sr(Ba)Fe₂O₇ (Ln=La, Nd, Eu). *Mater. Res. Bull.* **2013**, *48* (9), 3537-3544.

- (49) Gillie, L. J.; Wright, A. J.; Hadermann, J.; Van Tendeloo, G.; Greaves, C. Synthesis and characterization of the reduced double-layer manganite $\text{Sr}_3\text{Mn}_2\text{O}_{6+x}$. *J. Solid State Chem.* **2003**, *175* (2), 188-196.
- (50) Song, M. S.; Kim, S.; Lee, J. Y. Synthesis and physical properties of Ruddlesden-Popper phase $\text{Sr}_{3-x}\text{Mn}_2\text{Fe}_x\text{O}_{7-\delta}$ ($x = 0.15 \sim 1.0$). *Ceram. - Silik.* **2004**, *48*, 175-179.
- (51) Fan, L.; Rautama, E. L.; Lindén, J.; Sainio, J.; Jiang, H.; Sorsa, O.; Han, N.; Flox, C.; Zhao, Y.; Li, Y.; et al. Two orders of magnitude enhancement in oxygen evolution reactivity of $\text{La}_{0.7}\text{Sr}_{0.3}\text{Fe}_{1-x}\text{Ni}_x\text{O}_{3-\delta}$ by improving the electrical conductivity. *Nano Energy* **2022**, *93*, 106794.
- (52) Hona, R. K.; Karki, S. B.; Cao, T.; Mishra, R.; Sterbinsky, G. E.; Ramezanipour, F. Sustainable Oxide Electrocatalyst for Hydrogen- and Oxygen-Evolution Reactions. *ACS Catal.* **2021**, 14605-14614.
- (53) Hona, R. K.; Karki, S. B.; Ramezanipour, F. Oxide Electrocatalysts Based on Earth-Abundant Metals for Both Hydrogen- and Oxygen-Evolution Reactions. *ACS Sustain. Chem. Eng.* **2020**, *8* (31), 11549-11557.
- (54) Hona, R. K.; Ramezanipour, F. Remarkable Oxygen-Evolution Activity of a Perovskite Oxide from the $\text{Ca}_{2-x}\text{Sr}_x\text{Fe}_2\text{O}_{6-\delta}$ Series. *Angew. Chem.* **2019**, *131*, 2082-2085.
- (55) Retuerto, M.; Pascual, L.; Calle-Vallejo, F.; Ferrer, P.; Gianolio, D.; Pereira, A. G.; García, Á.; Torrero, J.; Fernández-Díaz, M. T.; Bencok, P.; et al. Na-doped ruthenium perovskite electrocatalysts with improved oxygen evolution activity and durability in acidic media. *Nat. Commun* **2019**, *10* (1), 2041.
- (56) Badreldin, A.; Abusrafa, A. E.; Abdel-Wahab, A. Oxygen-deficient perovskites for oxygen evolution reaction in alkaline media: a review. *emergent mater.* **2020**, *3* (5), 567-590.
- (57) Lu, M.; Zheng, Y.; Hu, Y.; Huang, B.; Ji, D.; Sun, M.; Li, J.; Peng, Y.; Si, R.; Xi, P.; et al. Artificially steering electrocatalytic oxygen evolution reaction mechanism by regulating oxygen defect contents in perovskites. *Sci Adv* **2022**, *8* (30), eabq3563.
- (58) Jin, H.; Guo, C.; Liu, X.; Liu, J.; Vasileff, A.; Jiao, Y.; Zheng, Y.; Qiao, S.-Z. Emerging Two-Dimensional Nanomaterials for Electrocatalysis. *Chem. Rev.* **2018**, *118* (13), 6337-6408.
- (59) Liang, Q.; Brocks, G.; Bieberle-Hütter, A. Oxygen evolution reaction (OER) mechanism under alkaline and acidic conditions. *J Phys: Energy* **2021**, *3* (2), 026001.
- (60) Wang, T.; Zhao, Q.; Fu, Y.; Lei, C.; Yang, B.; Li, Z.; Lei, L.; Wu, G.; Hou, Y. Carbon-Rich Nonprecious Metal Single Atom Electrocatalysts for CO_2 Reduction and Hydrogen Evolution. *Small Methods* **2019**, *3* (10), 1900210.
- (61) Dubouis, N.; Grimaud, A. The hydrogen evolution reaction: from material to interfacial descriptors. *Chem. Sci.* **2019**, *10* (40), 9165-9181.
- (62) Hona, R. K.; Huq, A.; Ramezanipour, F. Charge transport properties of $\text{Ca}_2\text{FeGaO}_{6-\delta}$ and $\text{CaSrFeGaO}_{6-\delta}$: The effect of defect-order. *Mater. Chem. Phys.* **2019**, 238.
- (63) Kananke-Gamage, C. C. W.; Ramezanipour, F. Variation of the electrocatalytic activity of isostructural oxides $\text{Sr}_2\text{LaFeMnO}_7$ and $\text{Sr}_2\text{LaCoMnO}_7$ for hydrogen and oxygen-evolution reactions. *Dalton Trans.* **2021**, *50* (40), 14196-14206.
- (64) Shafir, O.; Shopin, A.; Grinberg, I. Band-Gap Engineering of Mo- and W-Containing Perovskite Oxides Derived from Barium Titanate. *Physical Review Applied* **2020**, *13* (3), 034066. DOI: 10.1103/PhysRevApplied.13.034066.

- (65) Wang, Z.; Tan, S.; Xiong, Y.; Wei, J. Effect of B sites on the catalytic activities for perovskite oxides $\text{La}_{0.6}\text{Sr}_{0.4}\text{Co}_x\text{Fe}_{1-x}\text{O}_{3-\delta}$ as metal-air batteries catalysts. *Prog. Nat. Sci.* **2018**, *28* (4), 399-407.
- (66) Forslund, R.; Hardin, W.; Rong, X.; Abakumov, A.; Filimonov, D.; Alexander, C.; Mefford, J.; Iyer, H.; Kolpak, A.; Johnston, K.; et al. Exceptional electrocatalytic oxygen evolution via tunable charge transfer interactions in $\text{La}_{0.5}\text{Sr}_{1.5}\text{Ni}_{1-x}\text{Fe}_x\text{O}_{4\pm\delta}$ Ruddlesden-Popper oxides. *Nat. Commun.* **2018**, *9*.
- (67) Hona, R. K.; Ramezanipour, F. Structure-dependence of electrical conductivity and electrocatalytic properties of $\text{Sr}_2\text{Mn}_2\text{O}_6$ and $\text{CaSrMn}_2\text{O}_6$. *J Chem Sci* **2019**, *131* (11), 109.
- (68) Mitali, J.; Dhinakaran, S.; Mohamad, A. A. Energy storage systems: a review. *ENSS* **2022**, *1* (3), 166-216.
- (69) Lang, X.; Mo, H.; Hu, X.; Tian, H. Supercapacitor performance of perovskite $\text{La}_{1-x}\text{Sr}_x\text{MnO}_3$. *Dalton Trans.* **2017**, *46*, 13720-13730.
- (70) Mefford, J. T.; Hardin, W. G.; Dai, S.; Johnston, K. P.; Stevenson, K. J. Anion charge storage through oxygen intercalation in LaMnO_3 perovskite pseudocapacitor electrodes. *Nat. Mater* **2014**, *13* (7), 726-732.
- (71) Sang, Z.; Che, W.; Yang, S.; Liu, Y. Ruddlesden-Popper type $\text{La}_2\text{NiO}_{4+\delta}$ oxide as a pseudocapacitor electrode. *Mater. Lett.* **2018**, *217*. DOI: 10.1016/j.matlet.2018.01.030.
- (72) Jiang, Y.; Liu, J. Definitions of Pseudocapacitive Materials: A Brief Review. *Energy Environ. Sci.* **2019**, *2* (1), 30-37.
- (73) Alexander, C. T.; Mefford, J. T.; Saunders, J.; Forslund, R. P.; Johnston, K. P.; Stevenson, K. J. Anion-Based Pseudocapacitance of the Perovskite Library $\text{La}_{1-x}\text{Sr}_x\text{BO}_{3-\delta}$ (B = Fe, Mn, Co). *ACS Appl. Mater. Interfaces* **2019**, *11* (5), 5084-5094.
- (74) Liang, T.; Zhang, X.; Su, L.; Hou, R.; Yang, B.; Lang, J.; Yang, S.; Yan, X. Superiority of Cubic Perovskites Oxides with Strong B-O Hybridization for Oxygen-Anion Intercalation Pseudocapacitance. *Adv. Funct. Mater.* **2022**, *32* (30), 2202245.
- (75) Abdullah, N. A.; Osman, N.; Hasan, S.; Nordin, R. M. The Effect of Various Chelating Agents on the Thermal Decomposition of Cerate-Zirconate Ceramics Powder. *APCBEE Procedia* **2012**, *3*, 28-32.
- (76) Dreele, A. C. L. a. R. B. V. General Structure Analysis System (GSAS). *Los Alamos National Laboratory Report LAUR* **2004**, 86-748.
- (77) Toby, B. H. EXPGUI, a graphical user interface for GSAS. *J. Appl. Crystallogr.* **2001**, *34*, 210-213.
- (78) Long, Y.; Duvail, J.; Li, M.; Gu, C.; Liu, Z.; Ringer, S. P. Electrical Conductivity Studies on Individual Conjugated Polymer Nanowires: Two-Probe and Four-Probe Results. *Nanoscale Res. Lett.* **2009**, *5* (1), 237.
- (79) Singh, Y. ELECTRICAL RESISTIVITY MEASUREMENTS: A REVIEW. *Int. j. mod.phys.conf.ser.* **2013**, *22*, 745-756.
- (80) Li, Q.; Thangadurai, V. A comparative 2 and 4-probe DC and 2-probe AC electrical conductivity of novel co-doped $\text{Ce}_{0.9-x}\text{RE}_x\text{Mo}_{0.1}\text{O}_{2.1-0.5x}$ (RE = Y, Sm, Gd; x = 0.2, 0.3). *J. Mater. Chem. A* **2010**, *20* (37), 7970-7983.
- (81) Klicpera, M.; Javorský, P.; Diviš, M. Magnetization and electrical resistivity measurements on CeCuAl_3 single crystal. *JPCS* **2015**, *592* (1), 012014.
- (82) Ding, X.; Gao, B.; Krenkel, E.; Dawson, C.; Eckert, J. C.; Cheong, S.-W.; Zapf, V. Magnetic properties of double perovskite $\text{Ln}_2\text{CoIrO}_6$ (Ln=Eu, Tb, Ho): Hetero-tri-spin 3d-5d-4f systems. *Phys. Rev. B* **2019**, *99* (1), 014438.

- (83) Yang, T.; Mattick, V. F.; Chen, Y.; An, K.; Ma, D.; Huang, K. Crystal Structure and Transport Properties of Oxygen-Deficient Perovskite $\text{Sr}_{0.9}\text{Y}_{0.1}\text{CoO}_{3-\delta}$. *ACS Appl. Energy Mater.* **2018**, *1* (2), 822-832.
- (84) Jeerage, K. M.; Candelaria, S. L.; Stavis, S. M. Rapid Synthesis and Correlative Measurements of Electrocatalytic Nickel/Iron Oxide Nanoparticles. *Sci. Rep.* **2018**, *8* (1), 4584.
- (85) Du, X.; Ma, G.; Zhang, X. Experimental and Theoretical Understanding on Electrochemical Activation Processes of Nickel Selenide for Excellent Water-Splitting Performance: Comparing the Electrochemical Performances with M–NiSe (M = Co, Cu, and V). *ACS Sustain. Chem. Eng.* **2019**, *7* (23), 19257-19267.
- (86) Du, X.; Su, H.; Zhang, X. Metal–Organic Framework-Derived Cu-Doped Co_9S_8 Nanorod Array with Less Low-Valence Co Sites as Highly Efficient Bifunctional Electrodes for Overall Water Splitting. *ACS Sustain. Chem. Eng.* **2019**, *7* (19), 16917-16926.
- (87) Shannon, R. D. Revised effective ionic radii and systematic studies of interatomic distances in halides and chalcogenides. *Acta Crystallogr., Sect. A* **1976**, *32* (5), 751-767.
- (88) Green, M. A.; Neumann, D. A. Synthesis, Structure, and Electronic Properties of $\text{LaCa}_2\text{Mn}_2\text{O}_7$. *Chem. Mater.* **2000**, *12*, 90-97.
- (89) Ehsani, M. H.; Mehrabad, M. J.; Kameli, P.; Ghazi, M. E.; Razavi, F. S. Low-Temperature Electrical Resistivity of Bilayered $\text{LaSr}_2\text{Mn}_2\text{O}_7$ Manganite. *J. Low Temp. Phys* **2016**, *183*, 359-370.
- (90) Wudl, F.; Bryce, M. R. Apparatus for two-probe conductivity measurements on compressed powders. *J. Chem. Educ.* **1990**, *67* (8), 717.
- (91) Hona, R. K.; Huq, A.; Mulmi, S.; Ramezanipour, F. Transformation of Structure, Electrical Conductivity, and Magnetism in $\text{AA}'\text{Fe}_2\text{O}_{6-\delta}$, A = Sr, Ca and A' = Sr. *Inorg. Chem.* **2017**, *56* (16), 9716-9724.
- (92) Ehsani, M. H.; Ghazi, M. E.; Kameli, P.; Razavi, F. S. DC magnetization studies of nano- and micro-particles of bilayered manganite $\text{LaSr}_2\text{Mn}_2\text{O}_7$. *J. Alloys Compd.* **2014**, *586*, 261-266.
- (93) Wang, H.; Zhou, H.; Zhang, W.; Yao, S. Urea-assisted synthesis of amorphous molybdenum sulfide on P-doped carbon nanotubes for enhanced hydrogen evolution. *J. Mater. Sci.* **2018**, *53* (12), 8951-8962.
- (94) Gong, Q.; Wang, Y.; Hu, Q.; Zhou, J.; Feng, R.; Duchesne, P. N.; Zhang, P.; Chen, F.; Han, N.; Li, Y.; et al. Ultrasmall and phase-pure W_2C nanoparticles for efficient electrocatalytic and photoelectrochemical hydrogen evolution. *Nat. Commun* **2016**, *7* (1), 13216.
- (95) Hona, R. K.; Karki, S. B.; Cao, T.; Mishra, R.; Sterbinsky, G. E.; Ramezanipour, F. Sustainable Oxide Electrocatalyst for Hydrogen- and Oxygen-Evolution Reactions. *ACS Catal.* **2021**, *11* (23), 14605-14614.
- (96) Li, Y. H.; Liu, P. F.; Pan, L. F.; Wang, H. F.; Yang, Z. Z.; Zheng, L. R.; Hu, P.; Zhao, H. J.; Gu, L.; Yang, H. G. Local atomic structure modulations activate metal oxide as electrocatalyst for hydrogen evolution in acidic water. *Nat. Commun* **2015**, *6* (1), 8064.
- (97) Feng, H.; Xu, Z.; Ren, L.; Liu, C.; Zhuang, J.; Hu, Z.; Xu, X.; Chen, J.; Wang, J.; Hao, W.; et al. Activating Titania for Efficient Electrocatalysis by Vacancy Engineering. *ACS Catal.* **2018**, *8* (5), 4288-4293.

- (98) Morales, D. M.; Risch, M. Seven steps to reliable cyclic voltammetry measurements for the determination of double layer capacitance. *J Phys Energy* **2021**, *3* (3), 034013.
- (99) Hona, R. K.; Ramezanipour, F. Effect of the Oxygen Vacancies and Structural Order on the Oxygen Evolution Activity: A Case Study of $\text{SrMnO}_{3-\delta}$ Featuring Four Different Structure Types. *Inorg. Chem.* **2020**, *59*, 4685-4692.
- (100) Zhu, Y.; Zhou, W.; Sunarso, J.; Zhong, Y.; Shao, Z. Phosphorus-Doped Perovskite Oxide as Highly Efficient Water Oxidation Electrocatalyst in Alkaline Solution. *Adv. Funct. Mater.* **2016**, *26* (32), 5862-5872.
- (101) Karki, S. B.; Andriotis, A. N.; Menon, M.; Ramezanipour, F. Bifunctional Water-Splitting Electrocatalysis Achieved by Defect Order in $\text{LaA}_2\text{Fe}_3\text{O}_8$ (A = Ca, Sr). *ACS Appl. Energy Mater.* **2021**, *4* (11), 12063-12066.
- (102) Lasia, A. Mechanism and kinetics of the hydrogen evolution reaction. *Int. J. Hydrog. Energy* **2019**, *44* (36), 19484-19518.
- (103) Chen, G.-F.; Ma, T. Y.; Liu, Z.-Q.; Li, N.; Su, Y.-Z.; Davey, K.; Qiao, S.-Z. Efficient and Stable Bifunctional Electrocatalysts $\text{Ni/Ni}_x\text{M}_y$ (M = P, S) for Overall Water Splitting. *Adv. Funct. Mater.* **2016**, *26* (19), 3314-3323.
- (104) Sharma, I. B.; Magotra, S. K.; Singh, D.; Batra, S.; Mudher, K. D. S. Synthesis, structure, electric transport and magnetic properties of $\text{Sr}_2\text{LaMnFeO}_7$ and $\text{Sr}_2\text{LaMn}_{1.5}\text{Fe}_{0.5}\text{O}_7$. *J. Alloys Compd.* **1999**, *291*, 16-20.
- (105) El-Shinawi, H.; Bertha, A.; Hadermann, J.; Herranz, T.; Marco, J.; Berry, F.; Greaves, C. Synthesis and characterization of $\text{La}_{1+x}\text{Sr}_{2-x}\text{CoMnO}_{7-\delta}$ ($x=0,0.2$; $\delta=0,1$). *J. Solid State Chem.* **2010**, *183*, 1347-1353.
- (106) Beznosikov, B.; Aleksandrov, K. Perovskite-like crystals of the Ruddlesden-Popper series. *Crystallogr. Rep.* **2000**, *45*, 792-798.
- (107) Roy, S.; K, S.; Rao, U. Evaluation of Activation Energy (E_a) Profiles of Nanostructured Alumina Polycarbonate Composite Insulation Materials. *IJMMM* **2014**, *2*, 96-100.
- (108) Chupakhina, T. I.; Bazuev, G. V. Synthesis and magnetic properties of $\text{LaSr}_2\text{CoMnO}_7$. *Russ. J. Inorg* **2008**, *53* (5), 681-685.
- (109) Wang, H.; Lee, H.-W.; Deng, Y.; Lu, Z.; Hsu, P.-C.; Liu, Y.; Lin, D.; Cui, Y. Bifunctional non-noble metal oxide nanoparticle electrocatalysts through lithium-induced conversion for overall water splitting. *Nat. Commun.* **2015**, *6*, 7261.
- (110) Zheng, J.; Yan, Y.; Xu, B. Correcting the Hydrogen Diffusion Limitation in Rotating Disk Electrode Measurements of Hydrogen Evolution Reaction Kinetics. *J. Electrochem. Soc.* **2015**, *162* (14), F1470-F1481.
- (111) Xu, X.; Chen, Y.; Zhou, W.; Zhu, Z.; Su, C.; Liu, M.; Shao, Z. A Perovskite Electrocatalyst for Efficient Hydrogen Evolution Reaction. *Adv. Mater.* **2016**, *28* (30), 6442-6448.
- (112) Jiang, H.; Zhang, H.; Kang, Q.; Ma, H.; Tong, Y.; Gao, F.; Lu, Q. Rapid solvent-evaporation strategy for three-dimensional cobalt-based complex hierarchical architectures as catalysts for water oxidation. *Sci. Rep.* **2019**, *9* (1), 15681.
- (113) Zhu, Y.; Zhou, W.; Chen, Z.-G.; Chen, Y.; Su, C.; Tadó, M. O.; Shao, Z. $\text{SrNb}_{0.1}\text{Co}_{0.7}\text{Fe}_{0.2}\text{O}_{3-\delta}$ Perovskite as a Next-Generation Electrocatalyst for Oxygen Evolution in Alkaline Solution. *Angew. Chem. Int. Ed.* **2015**, *54* (13), 3897-3901.
- (114) Das, D.; Das, A.; Reghunath, M.; Nanda, K. K. Phosphine-free avenue to Co_2P nanoparticle encapsulated N,P co-doped CNTs: a novel non-enzymatic glucose sensor and

- an efficient electrocatalyst for oxygen evolution reaction. *Green Chem.* **2017**, *19* (5), 1327-1335.
- (115) Park, H. W.; Lee, D. U.; Park, M. G.; Ahmed, R.; Seo, M. H.; Nazar, L. F.; Chen, Z. Perovskite-nitrogen-doped carbon nanotube composite as bifunctional catalysts for rechargeable lithium-air batteries. *ChemSusChem* **2015**, *8* (6), 1058-1065.
- (116) Oh, M. Y.; Jeon, J. S.; Lee, J. J.; Kim, P.; Nahm, K. S. The bifunctional electrocatalytic activity of perovskite $\text{La}_{0.6}\text{Sr}_{0.4}\text{CoO}_{3-\delta}$ for oxygen reduction and evolution reactions. *RSC Adv.* **2015**, *5* (25), 19190-19198.
- (117) Zhao, Y.; Xu, L.; Mai, L.; Han, C.; An, Q.; Xu, X.; Liu, X.; Zhang, Q. Hierarchical mesoporous perovskite $\text{La}_{0.5}\text{Sr}_{0.5}\text{CoO}_{2.91}$ nanowires with ultrahigh capacity for Li-air batteries. *PNAS* **2012**, *109* (48), 19569-19574.
- (118) Saitoh, T.; Bocquet, A. E.; Mizokawa, T.; Fujimori, A. Systematic variation of the electronic structure of 3d transition-metal compounds. *Phys. Rev. B* **1995**, *52* (11), 7934-7938.
- (119) Bocquet, A. E.; Mizokawa, T.; Saitoh, T.; Namatame, H.; Fujimori, A. Electronic structure of 3d-transition-metal compounds by analysis of the 2p core-level photoemission spectra. *Phys. Rev. B* **1992**, *46* (7), 3771-3784.
- (120) Suntivich, J.; Hong, W. T.; Lee, Y.-L.; Rondinelli, J. M.; Yang, W.; Goodenough, J. B.; Dabrowski, B.; Freeland, J. W.; Shao-Horn, Y. Estimating Hybridization of Transition Metal and Oxygen States in Perovskites from O K-edge X-ray Absorption Spectroscopy. *J. Phys. Chem. C* **2014**, *118* (4), 1856-1863.
- (121) Hong, W. T.; Risch, M.; Stoerzinger, K. A.; Grimaud, A.; Suntivich, J.; Shao-Horn, Y. Toward the rational design of non-precious transition metal oxides for oxygen electrocatalysis. *Energy Environ. Sci.* **2015**, *8* (5), 1404-1427.
- (122) Suntivich, J.; May, K. J.; Gasteiger, H. A.; Goodenough, J. B.; Shao-Horn, Y. A Perovskite Oxide Optimized for Oxygen Evolution Catalysis from Molecular Orbital Principles. *Science* **2011**, *334* (6061), 1383-1385.
- (123) Moritomo, Y.; Higashi, K.; Matsuda, K.; Nakamura, A. Spin-state transition in layered perovskite cobalt oxides: $\text{La}_{2-x}\text{Sr}_x\text{CoO}_4$ ($0.4 \leq x \leq 1.0$). *Phys. Rev. B* **1997**, *55* (22), R14725-R14728.
- (124) Sharma, I. B.; Singh, C.; Singh, D. Synthesis, structure, electric transport and magnetic properties of $\text{Sr}_3\text{MnTiO}_{7-\delta}$. *J. Alloys Compd* **2004**, *375* (1), 11-14.
- (125) Zvereva, I.; Pavlova, T. a.; Pantchuk, V.; Semenov, V.; Breard, Y.; Choynet, J. THE SOLID SOLUTION $\text{Sr}_3\text{Ti}_{2-x}\text{Fe}_x\text{O}_{7-\delta}$ ($x \leq 0.5$): CHARACTERIZATION OF Fe (III) – Fe (IV) MIXED VALENCES. *Chim. Techno Acta* **2016**, *3*, 46-57.
- (126) Nuansaeng, S.; Yashima, M.; Matsuka, M.; Ishihara, T. Mixed Conductivity, Nonstoichiometric Oxygen, and Oxygen Permeation Properties in Co-Doped $\text{Sr}_3\text{Ti}_2\text{O}_{7-\delta}$. *Chem. Eur. J.* **2011**, *17* (40), 11324-11331.
- (127) Guan, D.; Zhou, J.; Huang, Y.-C.; Dong, C.-L.; Wang, J.-Q.; Zhou, W.; Shao, Z. Screening highly active perovskites for hydrogen-evolving reaction via unifying ionic electronegativity descriptor. *Nat. Commun* **2019**, *10* (1), 3755.
- (128) Bockris, J. O. M.; Otagawa, T. Mechanism of oxygen evolution on perovskites. *J. Phys. Chem* **1983**, *87* (15), 2960-2971.
- (129) Hou, L.; Shi, Y.; Zhu, S.; Rehan, M.; Pang, G.; Zhang, X.; Yuan, C. Hollow mesoporous hetero- $\text{NiCo}_2\text{S}_4/\text{Co}_9\text{S}_8$ submicro-spindles: unusual formation and excellent

- pseudocapacitance towards hybrid supercapacitors. *J. Mater. Chem. A* **2017**, *5* (1), 133-144.
- (130) Bockris, J. O. M.; Otagawa, T. The Electrocatalysis of Oxygen Evolution on Perovskites. *J. Electrochem. Soc.* **1984**, *131* (2), 290.
- (131) Kan, W. H.; Chen, M.; Bae, J.-S.; Kim, B.-H.; Thangadurai, V. Determination of Fe oxidation states in the B-site ordered perovskite-type $\text{Ba}_2\text{Ca}_{0.67}\text{Fe}_{0.33}\text{NbO}_{6-\delta}$ at the surface (nano-scale) and bulk by variable temperature XPS and TGA and their impact on electrochemical catalysis. *J. Mater. Chem. A* **2014**, *2* (23), 8736-8741.
- (132) Zhang, J.; Liu, H.; Shi, P.; Li, Y.; Huang, L.; Mai, W.; Tan, S.; Cai, X. Growth of nickel (111) plane: The key role in nickel for further improving the electrochemical property of hexagonal nickel hydroxide-nickel & reduced graphene oxide composite. *J. Power Sources* **2014**, *267*, 356-365.
- (133) Guo, D.; Zhang, H.; Yu, X.; Zhang, M.; Zhang, P.; Li, Q.; Wang, T. Facile synthesis and excellent electrochemical properties of CoMoO_4 nanoplate arrays as supercapacitors. *J. Mater. Chem. A* **2013**, *1* (24), 7247-7254.
- (134) Che, W.; Wei, M.; Sang, Z.; Ou, Y.; Liu, Y.; Liu, J. Perovskite $\text{LaNiO}_{3-\delta}$ oxide as an anion-intercalated pseudocapacitor electrode. *J. Alloys Compd.* **2018**, 731.
- (135) Kudo, T.; Obayashi, H.; Gejo, T. Electrochemical Behavior of the Perovskite-Type $\text{Nd}_{1-x}\text{Sr}_x\text{CoO}_3$ in an Aqueous Alkaline Solution. *J. Electrochem. Soc.* **1975**, *122* (2), 159.
- (136) Stoller, M. D.; Ruoff, R. S. Best practice methods for determining an electrode material's performance for ultracapacitors. *Energy & Environmental Science* **2010**, *3* (9).
- (137) Mo, H.; Nan, H.; Lang, X.; Liu, S.; Qiao, L.; Hu, X.; Tian, H. Influence of calcium doping on performance of LaMnO_3 supercapacitors. *Ceram. Int.* **2018**, *44* (8), 9733-9741.
- (138) Balamurugan, J.; Thanh, T. D.; Kim, N. H.; Lee, J. H. Facile synthesis of 3D hierarchical N-doped graphene nanosheet/cobalt encapsulated carbon nanotubes for high energy density asymmetric supercapacitors. *J. Mater. Chem. A* **2016**, *4* (24), 9555-9565.
- (139) Kim, B. K.; Sy, S.; Yu, A.; Zhang, J. Electrochemical Supercapacitors for Energy Storage and Conversion. In *Handbook of Clean Energy Systems*, 2015; pp 1-25.
- (140) Bag, S.; Raj, C. R. Facile shape-controlled growth of hierarchical mesoporous $\delta\text{-MnO}_2$ for the development of asymmetric supercapacitors. *J. Mater. Chem. A* **2016**, *4* (21), 8384-8394.

CURRICULUM VITAE

Chandana C W Kananke Gamage

SUMMARY

Innovative Researcher eager to discover novel materials for various applications and a self-motivated quick learner who appreciates both individual initiative and teamwork environments. Experiences include perovskite oxide-based material synthesis, property characterization and analysis. Quickly adaptable to new, demanding, and fast-paced working conditions with the passion to solve technical challenges and plan actionable insights for the execution towards the success, using critical thinking abilities.

EDUCATION

University of Louisville

Ph.D. in Chemistry, GPA – 3.87

Aug 2018 – May 2023 (Anticipated)

University of Colombo, Sri Lanka

B.Sc. (Special) in Computational Chemistry

Feb 2013 – Feb 2017

PROFESSIONAL EXPERIENCE

University of Louisville

Aug 2018 – Present

Graduate Researcher, Solid-State and Materials Chemistry

- Employ critical thinking skills to design and synthesize various metal oxide materials.
- Characterize and elucidate synthesized 2 and 3-Dimensional solid materials.
- Functional property studies such as electronic conductivities (both AC and DC) in perovskite oxide-based materials.
- Electrochemical measurements of electrocatalysts for OER/HER and pseudocapacitive energy storage.
- Maintenance of laboratory instruments such as high temperature furnaces, X-ray diffractometer, Potentiostats, and Rotating disk electrode (RDE).
- Provide leadership, mentorship, and training to junior graduate students in discipline.
- 4+ year experience on property studies of semiconducting and metallic materials based on perovskite oxides.

University of Louisville

Aug 2018 – Apr 2022

Graduate Teaching Assistant in General and Introductory Chemistry

- Instructor for Chem 201 and Chem 202 general chemistry recitation/tutoring classes.

Laboratory Analyst

- Performed analysis of Azo dye, extractable Perfluorinated compounds, Alkylphenol and Alkylphenol Ethoxylate and extractable Chlorophenols on fabric and leather.
- Responsible for the use of instruments for analysis. (Agilent GC-MS, Shimadzu UFLC-DAD)
- Validation of methods and quality control checks as per ISO+ requirements.
- Followed the quality assurance and quality control protocols with respect to the test methods.
- Faced SGS global audits and Sri Lanka Accreditation Board (SLAB) audits successfully.
- Trained for maintaining laboratory safety requirements as per SGS global safety requirements.

PROFESSIONAL SKILLS

- R & D in multi-step synthesis, characterization methods, data interpretation, data analysis, and relevant knowledge in electrochemical methods such as Cyclic Voltammetry (CV), Linear Sweep Voltammetry (LSV), Electrochemical Impedance Spectroscopy (EIS), Galvanostatic Cycling with Potential Limitation (GCPL), etc.
- **Instrumentation:** Powder X-ray Diffractometer (PXRD), Scanning Electron Microscope (SEM)/EDAX, X-ray Photo-electron Spectroscopy (XPS), RDE setup, Potentiostat, High temperature furnaces, Physical property measurement system (PPMS), Raman Spectroscopy, gas chromatography (GC-MS), liquid chromatography (LC-MS), NMR.
- **Software:** Proficient in High Score Plus, GSAS 1, Z view 2, Diamond 3, VESTA, Origin 9, EC-LAB, XPSPEAK41, EIS analyzer, Chemdraw, MS office, Fityk.
- **Training** - General laboratory safety practices.
- **Materials Synthesis** – Solid State, Solgel.
- Knowledge and experience in inorganic chemistry.
- Understanding challenges and use critical thinking, problem solving skills.
- Working in collaboration with other teams in related fields.

PUBLICATIONS

- Kananke-Gamage, C. C. W.; Ramezanipour, F. Isostructural Oxides $Sr_3Ti_{2-x}M_xO_{7-\delta}$ (M = Mn, Fe, Co; x = 0, 1) as Electrocatalysts for Water Splitting. In *Inorganics*, 2023; Vol. 11.
- Kananke-Gamage, C. C. W.; Ramezanipour, F. Structure Effect on Pseudocapacitive Properties of $A_2LaMn_2O_7$ (A = Ca, Sr). *Energy Technol.* **2023**, 2201249.
- Kananke-Gamage, C. C. W.; Ramezanipour, F. Effect of structural symmetry on magnetic, electrical and electrocatalytic properties of isoelectronic oxides $A_2LaMn_2O_7$ (A = Sr^{2+} , Ca^{2+}). *J Phys Chem Solids* **2022**, 171, 111013.
- Alom, M. S¹.; Kananke-Gamage, C. C. W.¹; Ramezanipour, F., Perovskite Oxides as electrocatalysts for hydrogen evolution reaction. *ACS Omega* **2022**, 7 (9), 7444-7451. (I co-first author)
- Kananke-Gamage, C. C. W.; Ramezanipour, F., Variation of the electrocatalytic activity of isostructural oxides $Sr_2LaFeMnO_7$ and $Sr_2LaCoMnO_7$ for hydrogen and oxygen-evolution reactions. *Dalton Trans.* **2021**, 50 (40), 14196-14206.

- Kananke-Gamage, C. C. W.; Ramezanipour, F., Effect of the B-site on Pseudocapacitance properties of two isostructural oxides $\text{Sr}_2\text{LaBMnO}_7$ (B = Co, Fe), manuscript under preparation.

CONFERENCE PRESENTATIONS

- American Chemical Society -National meeting (ACS Spring 2023), Oral March 2023
Impact of structural symmetry on electrocatalysis for water splitting using two isoelectronic oxides.
- Graduate Students Regional Research Conference (GSRRC), Louisville, Oral March 2023
Effect of structural symmetry on two isoelectronic oxides as electrocatalysts for water splitting.
- Graduate Students Regional Research Conference (GSRRC), Louisville, Oral March 2022
Study of the catalytic properties of bi-layered Ruddlesden Popper oxides for electrochemical water splitting.
- American Chemical Society -National meeting (ACS Spring 2022), Oral March 2022
Electrocatalysis for water splitting using two isostructural layered oxides.
- American Chemical Society -National meeting (ACS Fall 2021), (Atlanta), Oral August 2021
Study of electrical and electrocatalytic properties of layered oxides derived from perovskite structure.
- North American Solid State Research Conference (NASSRC Fall 2021), Oral July 2021
Investigation of electrical and electrochemical properties of layered Ruddlesden-Popper oxides.
- Graduate Students Regional Research Conference (GSRRC), Louisville, Oral March 2021
Structural, electrical and electrocatalytic properties of $\text{A}_3\text{B}_2\text{O}_7$ (A= $\text{Sr}^{2+}/\text{La}^{3+}$, B= $\text{Co}^{3+}/\text{Fe}^{3+}/\text{Mn}^{3+}/\text{Mn}^{4+}$).
- Graduate Students Regional Research Conference (GSRRC), Louisville, Oral February 2020
Electrical and electrocatalytic properties of a series of bilayered Ruddlesden-Popper oxides.

EXTRA-CURRICULAR

- Member of Chemistry Graduate Student Association, 2019-2022
- Member of Chemical Society, University of Colombo, Sri Lanka, 2015-2016
- Member of Astronomy Club, University of Colombo, Sri Lanka, 2014-2016

PROFESSIONAL MEMBERSHIP

- American Chemical Society (ACS), since 2021